# 学 位 論 文

# Quantum disordered phases in the frustrated honeycomb antiferromagnets

(ハニカム反強磁性体における量子無秩序相)

平成２９年 ３月博士（理学）申請

東京大学大学院理学系研究科

物理学専攻

張　昊

# Quantum disordered phases in the frustrated honeycomb antiferromagnets

A dissertation submitted to

DEPARTMENT OF PHYSICS
GRADUATE SCHOOL OF SCIENCE
THE UNIVERSITY OF TOKYO

in partial fulfillment of the requirements for the degree of

DOCTOR OF PHILOSOPHY

By

Hao Zhang

February 2017

# Abstract

The two-dimensional frustrated quantum spin systems have become a corner stone in the understanding of novel and exotic physical phenomena in quantum magnetism. The inclusion of frustration is expected to enhance the effect of quantum spin fluctuations which may induce novel disordered phases such as quantum spin liquids. One typical two-dimensional system is the quantum $J_1$-$J_2$ model on the honeycomb lattice, where the lowest possible coordination number in two-dimensional systems enhances the quantum fluctuations. Recently, the possible spin liquid phase found in the Hubbard model on the honeycomb lattice and the spin liquid behavior observed in the bismuth oxynitrate compound, $Bi_3Mn_4O_{12}(NO_3)$, also induce the interest for this system.

In this thesis, we study quantum disordered phases in the frustrated Heisenberg model on the single layer and bilayer honeycomb lattices. This thesis contains three main parts. In the first part, we study the ground-state phase diagram of the frustrated quantum Heisenberg antiferromagnet on the single-layer honeycomb lattice with the first ($J_1$) and second ($J_2$) nearest-neighbor couplings using a mean-field approach in terms of the Schwinger boson representation of the spin operators. We calculate the ground-state energy, local magnetization, energy gap and spin-spin correlations. The system shows magnetic long range order for $0 \leq J_2/J_1 \lesssim 0.2075$ (Néel) and $0.398 \lesssim J_2/J_1 \leq 0.5$ (spiral). In the intermediate region, we find two magnetically disordered phases: a gapped spin liquid phase which shows short-range Néel correlations ($0.2075 \lesssim J_2/J_1 \lesssim 0.3732$), and a lattice nematic phase ($0.3732 \lesssim J_2/J_1 \lesssim 0.398$), which is magnetically disordered but breaks lattice rotational symmetry.

In the second part, we use a combination of analytical and numerical techniques to study the quantum melting of Néel order in the frustrated Heisenberg model on the bilayer honeycomb lattice. Using a similar Schwinger boson mean-field theory, the ground-state phase diagram is studied as a

function of the frustration intralayer coupling $J_2$ and the interlayer coupling $J_\perp$. We also investigate the spin gap, local magnetization, spin-spin correlations and ground-state energy. We find a novel reentrant behavior in the melting curve of Néel order. We complement the study with exact diagonalization on small clusters performed by C. A. Lamas. Using a linear spin wave approach we also study the melting of Néel phase as a function of the spin $S$, the frustration coupling $J_2$ and the interlayer coupling $J_\perp$.

In the third part, we study the Heisenberg antiferromagnet on a bilayer honeycomb lattice including interlayer frustration due to the competing interactions, $J_1$, $J_\perp$, and $J_x$. We map out its quantum phase diagram based on Schwinger boson and bond operator approaches. This is also supplemented by dimer series expansion by M. Arlego and W. Brenig, and exact diagonalization by C. A. Lamas. Analyzing ground state energies and spin correlation functions, we find four distinct phases, corresponding to three collinear magnetic long range ordered states, and one quantum disordered interlayer dimer phase. The latter phase is adiabatically connected to an exact singlet product ground state of the the bilayer which exists along a line of maximum interlayer frustration in the phase diagram of $(J_x, J_1)$. The types of orders within the remaining three phases are clarified.

In summary, for the single layer case, we found that two types of magnetically disordered phases exist in the intermediate frustration region and the lattice rotational symmetry breaks in the part of large $J_2/J_1$ in the magnetically disordered region. For the bilayer case with intralayer frustration, we found a novel reentrant behavior in the melting curve of Néel order. To the best of our knowledge, it is the first time to provide a comprehensive study about the ground-state phase diagram for the bilayer case with interlayer frustration. Our studies of the frustrated systems on the honeycomb single layer and bilayer lattices provide a systematic investigation about the effects of frustration to the ground state and should play an important role in the understanding of the quantum phases and the competition between the frustration and unfrustration couplings in the large family of frustrated magnets.

# Acknowledgements

It is a pleasure to thank the people to whom I have owed a great deal in completing this thesis. First and foremost, I would like to express my thanks to my doctoral supervisor, Prof. Hirokazu Tsunetsugu for introducing me to the interesting field of frustrated magnetism, proposing the project for this thesis, his insightful guidance and advice over my entire period of doctoral studies at the University of Tokyo. As a foreign student, I would like to thank him for his genuine kindness and solicitude for my daily life during my stay in Japan.

I would like to thank my collaborator, Dr. Carlos A. Lamas for his kind support and fruitful discussions. I have learned technical points about numerical calculations from his code. He also performed exact diagonalization for the bilayer system and provided data which are used for comparison in Chapter 3 and Chapter 4. I have enjoyed collaborated with him and learned a lot from him. The exchanges have always been inspiring and stimulating. I also would like to thank Dr. Marcelo Arlego and Prof. Dr. Wolfram Brenig for our fruitful collaboration. They also performed dimer series expansion for the bilayer system including interlayer frustration and provided results which are used for comparison in Chapter 4.

I would like to thank Prof. Masaki Oshikawa for his course and the theoretical seminar organized by him.

I would like to thank Prof. Peng Li for fruitful discussions about the Schwinger boson method.

I would like to thank everyone in Prof. Tsunetsugu's group, especially for Dr. Kazumasa Hattori, who was the research associate of Prof. Tsunetsugu's group during my doctor course. He gave me a lot of help both in my research and daily life, especially for the use of the workstation. It was pleasure to have countless valuable discussions with Dr. Kazumasa Hattori and Dr. Toshihiro Sato on a wide range of topics in physics. Special thanks go to Mr. Junji Takano, my tutor when I studied at the University of Tokyo during the

first year of my doctorate.

I would like to also thank Ms. Mayumi Matsushita and Ms. Atsuko Tsuji for their administrative assistance and numerous help in my daily life. I would also like to thank Ms. Emiko Gosho of the International Liaison Office, Graduate School of Science, who helped me greatly in my life and study in Japan. I would like to thank the Japanese Government Scholarship for their financial support during my stay in Japan.

I would like to thank Prof. Lu Yu at the Institute of Physics, Chinese Academy of Sciences and Prof. Guang-Ming Zhang at the Department of Physics, Tsinghua University for continuous encouragement and solicitude.

Finally I would like to express my thanks to my parents for continuous support and encouragement.

Hao Zhang
*The University of Tokyo*
*February 2017*

# List of Publications

These are published works related to this thesis.

- Hao Zhang and C. A. Lamas,
  *Exotic disordered phases in the quantum $J_1$-$J_2$ model on the honeycomb lattice*
  Physical Review B **87**, 024415 (2013)

- Hao Zhang, M. Arlego, and C. A. Lamas,
  *Quantum phases in the frustrated Heisenberg model on the bilayer honeycomb lattice*
  Physical Review B **89**, 024403 (2014)

- Hao Zhang, Carlos A. Lamas, Marcelo Arlego, and Wolfram Brenig,
  *Quantum phase diagram of a frustrated antiferromagnet on the bilayer honeycomb lattice*
  Physical Review B **93**, 235150 (2016)

# List of Publications Added for Reference

- Hao Zhang, Guang-Ming Zhang and Lu Yu,
  *Spin transport properties of a quantum dot coupled to ferromagnetic leads with noncollinear magnetizations*
  J. Phys.: Condens. Matter **21**, 155501 (2009)

- M. Arlego, C. A. Lamas, and Hao Zhang,
  *Self consistent study of the quantum phases in a frustrated antiferromagnet on the bilayer honeycomb lattice*
  J. Phys.: Conf. Series **568**, 042019 (2014)

# Contents

# Chapter 1

# Introduction

This chapter reviews the basic background of our studies. In Sec. 1.1, we briefly review frustration effects and exotic magnetically disordered phases which are induced by frustration and quantum fluctuations. Then in Sec. 1.2, we review the experimental results that motivated our studies. Sec. 1.3 is a review of the previous theoretical studies about the phase diagram of the frustrated Heisenberg antiferromagnets on the honeycomb lattice. In Sec. 1.4, we introduce the main method we have used, an improved version of Schwinger boson mean-field theory which includes both ferromagnetic and antiferromagnetic correlations, and show some available comparisons with quantum Monte Carlo method and exact diagonalizations. Finally, in the end of this chapter, Sec. 1.5, we summarize the purpose and present the overview of this thesis.

## 1.1 Frustrated magnets and exotic magnetically disordered phases

Frustrated quantum spin systems have attracted a great deal of interest both theoretically and experimentally in recent years [1, 2]. When a spin system is frustrated, no spin configuration can fully minimize all the interactions of spins at the same time. There are two types of frustration. One is so-called geometrical frustration, in which there exists only one type of interactions

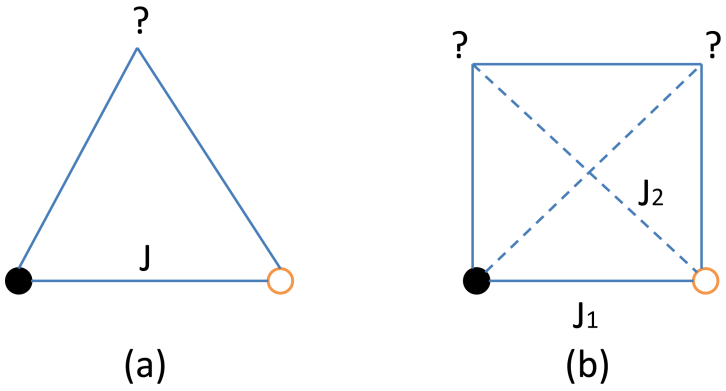


Figure 1.1: Examples of frustrated systems: (a) The triangular Heisenberg antiferromagnetic cluster. (b) The $J_1$-$J_2$ square Heisenberg antiferromagnetic cluster. The black and void circles represent antiparallel configurations of spins. Choosing any orientation for the spin marked by the question mark will leave at least one of its bonds unsatisfied (frustrated bonds).

but frustration comes from special geometry of the lattice. A triangular or Kagome lattice in two dimensions and a pyrochlore lattice in three dimensions are typical examples. In Fig. 1.1 (a), we show the triangular Heisenberg antiferromagnetic cluster as one example of this type. The other type is the case when there are several competing exchange interactions, for example, the competition between the first and second neighboring antiferromagnetic exchange interactions on a square or honeycomb lattice. In Fig. 1.1 (b), we show the $J_1$-$J_2$ square Heisenberg antiferromagnetic cluster as one example of this type. Frustration as well as quantum fluctuations suppresses or may even destroy a long-range magnetic order in spin systems, and this may result in exotic magnetically disordered phases [3–5, 9]. If any symmetry is spontaneously broken, this phase can be classified according to the broken symmetry, but if no symmetry is broken, the phase belongs to the so-called quantum spin liquid [3, 4], which is one of the most exciting and interesting topics in modern condensed matter physics.

Among these magnetically disordered phases, the valence-bond crystals (VBC) is the simplest scenario to overcome frustration. In this phase, the spins construct themselves into small clusters which are arranged in a spa-

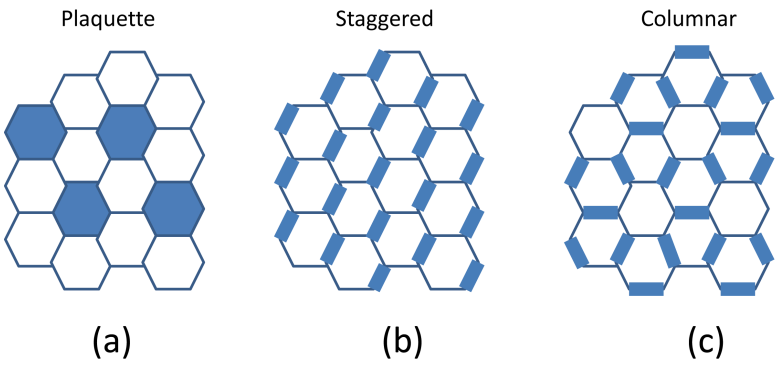


Figure 1.2: Three possible valence bond crystal states on a honeycomb lattice: (a) The plaquette VBC. (b) The staggered VBC which is also called the lattice nematic [36]. (c) The columnar VBC which is also called the Read-Sachdev state [7].

tially regular pattern of singlets: dimers, quadrumers (four-site plaquettes) or 2n-mers $S = 0$ plaquettes [1]. In a VBC phase, there is no magnetic long-range order (no spin $SU(2)$ symmetry breaking), but long-range order in the dimer-dimer correlation function. From this definition, the VBC phase may spontaneously break some lattice symmetry or may break no lattice symmetry [1]. In the other point of view, the VBCs are absence of long-range order in spin-spin correlations, but spontaneously break some lattice symmetry [1, 6]. In the following, we will use the second definition. In Fig. 1.2, we show three possible VBC states on a honeycomb lattice. All of the three VBC states break the lattice rotational symmetry. While both of the plaquette VBC and the columnar VBC break the lattice translational symmetry. However, the staggered VBC maintains the lattice translational symmetry.

Finally we briefly explain some phases discussed in this thesis. Three of them are magnetically disordered phases. The gapped spin liquid (GSL) [8,9] preserves both the lattice translational symmetry and the lattice rotational symmetry. The staggered VBC preserves the lattice translational symmetry, but breaks the lattice rotational symmetry (see Fig. 1.2(b)). In the plaquette VBC state, the lattice translational symmetry is broken, and the unit cell is tripled and contains 6 sites. The $C_3$ lattice rotational symmetry, corresponding to $2\pi/3$ rotations around an axis perpendicular to the plane and passing

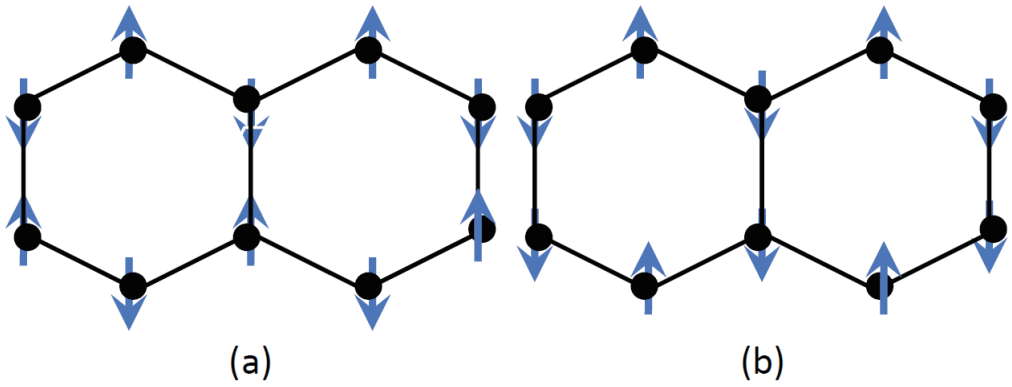


Figure 1.3: Schematic representation of (a) the Néel phase and (b) the Néel-II phase on the honeycomb lattice. Arrows represent spins.

through a site, is broken. However, the global $C_6$ lattice rotational symmetry is preserved (see Fig. 1.2(a)). Other phases are magnetically ordered. As shown in Fig. 1.3(a), in the Néel phase [10], the spins align in a pattern with neighboring spins pointing in opposite directions. As shown in Fig. 1.3(b), the Néel-II phase [53, 59] is a kind of collinear magnetically ordered phase. Here collinear means that the spin configuration is parallel or antiparallel to each other, while non-collinear means that not all spin configurations in the system are parallel or antiparallel to each other. The Néel-II phase has antiferromagnetic sawtooth chains along one of the three equivalent honeycomb directions, and the nearest neighbor spins on adjacent chains are parallel to one another.

## 1.2 Experimental background

One of the motivations of the present study is provided by experimental studies on frustrated honeycomb antiferromagnets. One example of these materials is the bismuth oxynitrate, $Bi_3Mn_4O_{12}(NO_3)$, which was synthesized by Smirnova *et al.* [11]. The crystal structure of $Bi_3Mn_4O_{12}(NO_3)$ is shown in Fig. 1.4 [12]. It consists of $Bi^{3+}$, $Mn^{4+}$, $O^{2-}$ ions and $NO_3^-$ layers. As

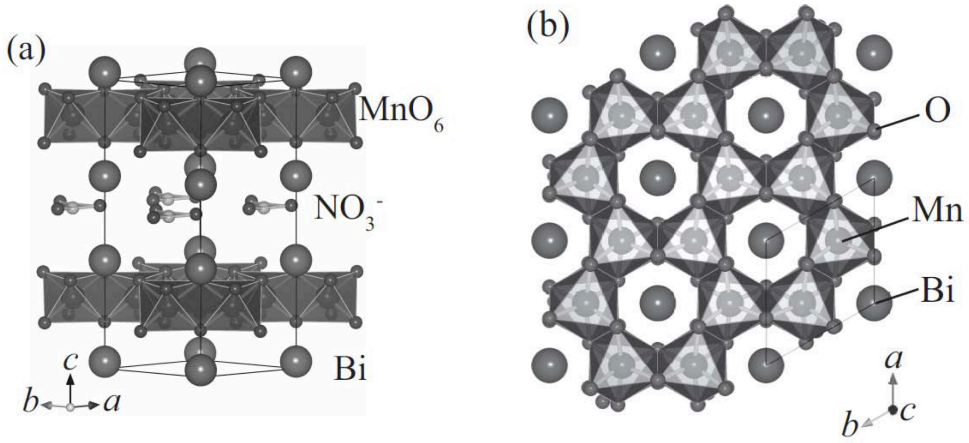


Figure 1.4: (a) Polyhedral representation of $Bi_3Mn_4O_{12}(NO_3)$ structure. (b) Honeycomb structure of $MnO_6$ in the *ab* plane. (from Ref. [12])

shown in this figure, this compound has a trigonal structure ($P3$) with the lattice constants $a = 0.49692$ nm and $c = 1.31627$ nm. The $MnO_6$ layers are separated by Bi and $NO_3$ layers, and this leads to short (0.478nm) and long (0.838nm) honeycomb interlayer distances, forming a stacked bilayer structure. The $Mn^{4+}$ ions have a spin $S = 3/2$ and form a honeycomb lattice in the *ab* plane, as shown in Fig. 1.4(b). This honeycomb lattice is uniform, without any distortion. The substitutions of $Mn^{4+}(S = 3/2)$ in $Bi_3Mn_4O_{12}(NO_3)$ by $Cr^{4+}(S = 1)$ or $V^{4+}(S = 1/2)$ may lead, if possible, to the realization of the Heisenberg model on the honeycomb lattice with other spin quantum numbers [11].

The magnetic susceptibility $\chi(T)$ shows a broad maximum at about 70K in its temperature dependence as shown in Fig. 1.5(a). This is a typical feature of low-dimensional antiferromagnets and is consistent with the two-dimensional crystal structure [11]. Fitting the data between 300 and 400K to the Curie-Weiss law $\chi = C/(T - \theta) + \chi_0$ obtains Curie constant $C = 2.21$ emu·K/mol, Weiss temperature $\theta = -257$ K, and the temperature-independent term $\chi_0 = -1.16 \times 10^{-4}$ emu/mol. Despite a relatively large Weiss temperature of $-257$K, no long-range magnetic order was observed down to 0.4K [11]. The upturn in magnetic susceptibility below 20K is not

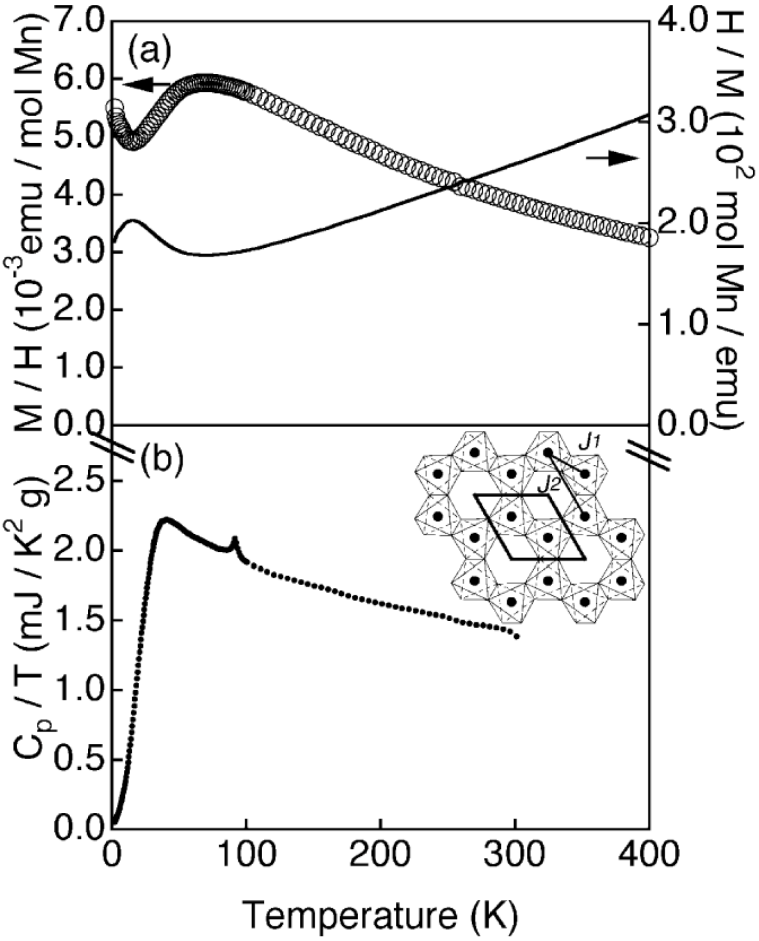


Figure 1.5: Temperature dependence of basic thermodynamic quantities in $Bi_3Mn_4O_{12}(NO_3)$. (a) The magnetic susceptibility (open circles) and the inverse susceptibility (solid line). (b) The specific heat divided by temperature of $Bi_3Mn_4O_{12}(NO_3)$ solidified at 6 GPs. (from Ref. [11])

a sign of the magnetic long-range order, since the specific heat data shown in Fig. 1.5(b) exhibits no clear anomaly. This upturn should come from impurity spins due to structural defects [11].

In the specific heat data of Fig. 1.5(b), the lattice contribution is not subtracted. The small peak at 95K is due to the antiferromagnetic ordering of $MnO_2$ which presents as the secondary phase, and this ordering is detected by Synchrotron X-ray powder diffraction and neutron powder diffraction

| Exchange | U=4.0eV | U=6.0eV | U=8.0eV |
|---|---|---|---|
| $J_1$ | 3.00(34.8) | 1.7(19.7) | 0.9(10.4) |
| $J_2$ | 0.4(4.6) | 0.2(2.3) | 0.1(1.2) |
| $J_3$ | 0.47(5.4) | 0.3(2.7) | 0.2(2.3) |
| $J_\perp$ | 4.10(47.6) | 2.7(31.3) | 2.1(24.4) |
| $J_2/J_1$ | 0.13333 | 0.1176 | 0.1111 |
| $J_3/J_1$ | 0.15667 | 0.17647 | 0.2222 |

Table 1.1: Exchange constants in $Bi_3Mn_4O_{12}(NO_3)$ in units of meV calculated by a density functional approach. Values in units of Kelvin (K) are shown in parentheses. Here $J_3$ is the third nearest neighbor coupling and U is the Coulomb repulsion on the Mn site. (from Ref. [15])

measurements [11]. There is a broad maximum at around 40K, and the specific heat decreases to zero with decreasing temperature. There is no other peak between 0.4 and 300K, which is an indication of the absence of magnetic long-range order in $Bi_3Mn_4O_{12}(NO_3)$ in this period.

Recently, $Bi_3Mn_4O_{12}(NO_3)$ was investigated by neutron scattering experiments [13, 14]. The results did not show any magnetic order down to 3K, confirming that the ground state is magnetically disordered. In Ref. [13], Matsuda *et. al.* have experimentally determined the values of exchange coupling constants. The nearest neighbor coupling $J_1$, the next nearest neighbor coupling $J_2$ and the interlayer coupling $J_\perp$ are the dominant couplings and they compete to each other. Their estimated values are $J_1 = 1.4$ meV, $J_2 = 0.2$ meV and $J_\perp = 0.7$ meV. The magnetic exchange coupling constants have been also calculated using the density functional theory [15], and the results are shown in Table. 1.1. Here positive value means antiferromagnetic. The dominant interactions are the intralayer nearest-neighbor interaction $J_1$ and the interlayer interaction $J_\perp$: $J_1$ is almost an order of magnitude larger than $J_2$, which is similar to the value of $J_3$, and $J_\perp$ is always larger than all the other interactions. Therefore, they claimed that the frustration in this compound is not strong, and that it is necessary to consider the interlayer interaction $J_\perp$ when the magnetic properties are studied. Therefore, an effective model of $Bi_3Mn_4O_{12}(NO_3)$ is an $S = 3/2$ frustrated Heisenberg model

on the bilayer honeycomb lattice. The neutron scattering experiments under applied magnetic fields have also been done, and it was found that the Néel order appears at about 6T [13]. These experimental progresses have raised the interest in the study of magnetically disordered phases in honeycomb lattice antiferromagnets. The substitution of $Mn^{4+}$ in $Bi_3Mn_4O_{12}(NO_3)$ by $V^{4+}$ may realize the $S = 1/2$ Heisenberg model on the honeycomb lattice [11] studied in the thesis.

## 1.3 Previous theoretical results

The Heisenberg model on two-dimensional (2D) bipartite lattices has been intensively studied in the last few decades [1, 2, 16]. In the unfrustrated case, the classical ground state is such that all the spins in one sublattice point in one direction whereas in the other sublattice the spins point in the opposite direction. However, in the quantum case this state is not the real ground state, and quantum effects yield finite corrections. The quantum ground state is exactly known for the one-dimensional Heisenberg model [17], but no exact results are known for the two dimensional Heisenberg antiferromagnets, even for simple lattices like the square lattice. However, several experimental and numerical studies suggested that the ground state is in fact the antiferromagnetically ordered Néel type state [16]. In contrast, when we include frustration in the system, for example by including second neighbor interactions, the ground state may become much more complicated.

In the quantum case, the ground state energy is lower than the classical value, due to the quantum fluctuations. The effects of these fluctuations vary depending on the spatial dimensions, the spin quantum number, the presence of frustrating interactions and the coordination number of the lattice site. One may ask how the quantum fluctuations depend on the coordination number. Two typical examples of 2D unfrustrated systems are the square lattice, with coordination number $z = 4$, and the honeycomb lattice with $z = 3$. Previous results [19–22] have shown that the staggered magnetization is smaller in the honeycomb lattice ($z = 3$) case. For example, the second order spin wave calculations show that it is 0.3034 in the square lattice ($z = 4$)

case [18] while it is 0.2418 in the honeycomb lattice ($z = 3$) case [21]. This behavior is in accord with the tendency towards a less classical behavior for systems with smaller coordination number.

Including frustration in 2D quantum antiferromagnets is expected to enhance quantum spin fluctuations and hence suppresses magnetic order [3]. This idea has motivated many researchers to look for its realization [23–27]. Generally speaking, a combination of strong quantum fluctuations and strong frustration is ideal to realize exotic quantum disordered phases. A good example is the frustrated Heisenberg model on the honeycomb lattice. Due to the small coordination number ($z = 3$) which is minimal in a two dimensional system, quantum fluctuations could be stronger than those on the square lattice and may destroy the antiferromagnetic order [28–31]. Frustration can be easily introduced by the second-nearest-neighbor couplings $J_2$, and also the third-nearest-neighbor couplings $J_3$. Therefore, $S = 1/2$ frustrated Heisenberg models on the honeycomb lattice plays an important role among two dimensional systems.

Other recent interest has also arisen from the possible spin liquid phase found in the Hubbard model on the honeycomb lattice [37,60–66]. The quantum Monte Carlo simulation by Meng *et al.* [60] shows a strong evidence for a gapped spin liquid phase in the range of $3.5 < U/t < 4.3$ ($U$ is the strength of the on-site Coulomb repulsion and $t$ is the nearest-neighbor hopping amplitude), sandwiched between the semimetal phase at smaller $U/t$ and the antiferromagnetic phase at larger $U/t$. In the strong coupling $U \to +\infty$ limit, the low energy Hamiltonian is the $S = 1/2$ Heisenberg model with nearest-neighbor antiferromagnetic interactions $J_1 = 4t^2/U$ [67]. Approaching from the strong coupling side, the physics for some intermediate values of $U$ can be described by $S = 1/2$ Heisenberg model with nearest-neighbor antiferromagnetic interactions $J_1 = 4t^2/U - 16t^4/U^3$ and second-nearest-neighbor antiferromagnetic interactions $J_2 = 4t^4/U^3$ [67].

Last but not least, the studies of graphene [68] and topological insulators [69, 70] have also led to interest in strongly correlated electron systems on the honeycomb lattice with spin-orbit coupling.

Due to these reasons, frustrated Heisenberg models on the honeycomb

lattice have attracted intensive attention recently [31–53]. Most of the previous studies have investigated the single layer case, in which the frustration is due to second-nearest-neighbor interactions [31–41], and the case with also third-nearest-neighbor interactions [42–53]. The phase diagrams were determined and the possibility of quantum disordered phases has been reported [36–41, 48–59]. From the theoretical point of view, it is interesting to study the bilayer case and the effect of an interlayer coupling $J_\perp$ on the stabilization of these disordered phases. In particular in the bilayer models, the ground state at very large $J_\perp$ is a dimer product state [85]. For the unfrustrated models a transition between the Néel phase and the dimer phase is expected to occur as the interlayer coupling is increased [72–81, 84]. One interesting point is the effects of frustration in each layer on the "melting" of Néel order. By contrast in the frustrated case, the system may change from a nonmagnetic nematic phase to a dimer product state as the interlayer coupling is increased. Recently, a few attentions have been given to bilayer honeycomb lattice [32, 85, 86], but the main focus has been on the unfrustrated case [32, 85].

### 1.3.1 Single layer case

Now we review previous theoretical results of the single layer model. The ground state of the classical ($S \to \infty$) $J_1$-$J_2$ Heisenberg model on the honeycomb lattice has been studied extensively [36, 42–44]. The Néel state at $J_2 = 0$ is stable up to $J_2/J_1 = 1/6$. For $J_2/J_1 > 1/6$, it changes to degenerate spin spiral states. As shown in Fig. 1.6, for $1/6 < J_2/J_1 < 1/2$, the spiral wave vectors of the degenerate states form a closed line [36, 42, 43] around the center of the first Brillouin zone. For $J_2/J_1 > 1/2$, they form lines [36] around the Brillouin zone corners. Mulder *et al.* [36] have considered the leading quantum corrections by the spin wave theory, and found that this degeneracy is lifted and some specific wave vectors are favoured by the quantum fluctuations. There are a total of six symmetry related wave vectors for each $J_2/J_1$, and each wave vector is obtained by $2\pi/6$ rotations of the neighbor one. As shown in Fig. 1.6, as $J_2/J_1$ is increased from 1/6 to 1/2,

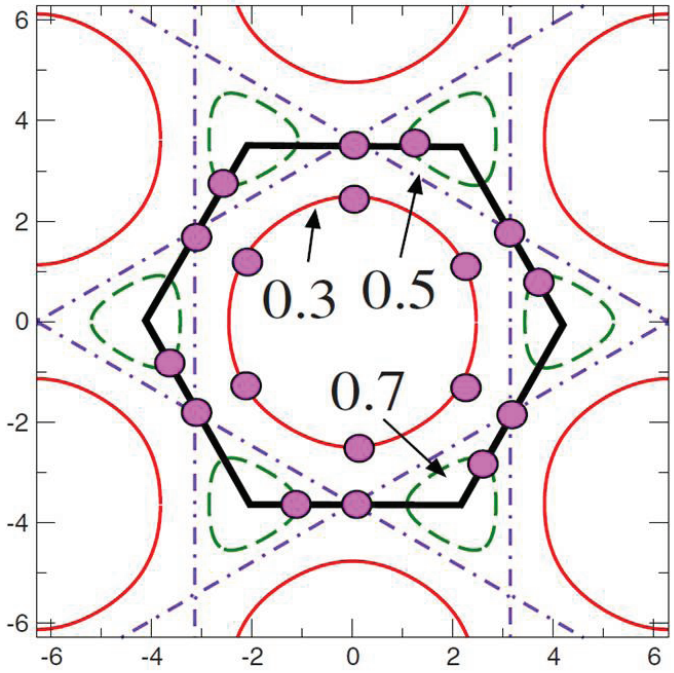


Figure 1.6: Classically degenerate spiral wave vectors for $J_2/J_1 = 0.3$ (red, solid), $J_2/J_1 = 0.3$ (purple, dash-dotted), and $J_2/J_1 = 0.7$ (green, dashed). Magenta dots are the six distinct spiral wave vectors lying on this manifold which are favored by quantum fluctuations. Black (thick solid) hexagon indicates the first Brillouin zone of the lattice.(from Ref. [36])

the wave vectors move from the center of the Brillouin zone towards six edge centers. As $J_2/J_1$ is increased beyond 1/2, each wave vector moves from each edge center along the edge towards each corner of the Brillouin zone. Each point located at a general position in the Brillouin zone has 11 equivalent points. However, for the points on the Brillouin zone boundary, these 12 points are not all different. When a point is on the boundary but not at the corners, it has only 5 equivalent points and the other 6 points are the same since they are shifted from the original ones by one of the reciprocal lattice vectors. In other words, an unmarked point on the green contour is the same as a marked point on the opposite edge of the Brillouin zone, and they differ by a reciprocal lattice vector.

The quantum $J_1$-$J_2$ Heisenberg model on the honeycomb lattice has been studied recently by various approaches, including spin wave theory [31,32,36, 42, 43],a non-linear $\sigma$-model approach [31, 33], mean-field theory [31, 36, 37], exact diagonalization [38, 43, 50], variational Monte Carlo method [39, 40], series expansion [45], pseudofermion functional renormalization group [51] and coupled-cluster method [41, 53]. Most of the studies have focused on the $S = 1/2$ case. However, these studies yielded controversial physical scenarios.

The linear spin wave theory [31, 43] and non-linear $\sigma$-model approach [31, 33] have been used to examine the stability of the Néel state, since they are not suitable to study quantum disordered phases. The linear spin wave theory predicts the critical value $J_2^c \approx 0.1$ [31, 43], above which the Néel state is not stable, while the critical value obtained by the non-linear $\sigma$-model approach is $J_2^c \approx 0.12$ [33]. However, using the approach which includes the quantum corrections by the linear spin wave theory and Schwinger boson mean-field theory, Mattsson *et al.* [31] pointed out that for $S = 1/2$ there is no Néel order even without frustration. They concluded that the non-linear $\sigma$-model approach underestimates the stability of the Néel order for $S = 1/2$.

Using a bond operator mean-field theory, Mulder *et al.* [36] claimed the staggered VBC state (see Fig. 1.2, also called lattice nematic in Ref. [36]) for $J_2 \gtrsim 0.25J_1$, in a wide range of frustration. They assumed the condensation of the singlet operators and replaced them with a c-number. Then the Hamiltonian is represented by triplet operators alone, and they kept in the Hamiltonian quadratic and quartic orders of triplet operators. They have compared its ground state energy with the energy of the spiral state including leading order spin wave corrections. At quadratic level, the energy of the staggered VBC state is lower than the spiral state in a small region near $J_2 = 0.35J_1$. However, at the quartic level, this region expands to $J_2 \gtrsim 0.25J_1$, except for a small region near $J_2 = 0.5J_1$. They also noted that their bond operator mean-field theory does not include the fluctuations of the singlets, which can be taken into account in Schwinger boson formalism.

Mattsson *et al.* [31] used Schwinger boson mean-field theory to study the stability of the Néel state. The critical value $J_2^c \approx 0.2$, which is much larger than the one obtained by linear spin wave theory, $J_2^c \approx 0.1$ [31, 43]. They

explained that the differences of results between Schwinger boson mean-field theory and spin wave theory should vanish in the first-order spin wave theory through the cancellation of two logarithmic divergences [31]. The first-order spin wave theory contains $1/S$ corrections to linear spin wave theory. Therefore, they concluded that quantum fluctuations stabilize a state which is classically forbidden. However, the mean-field decoupling used by Mattsson *et al.* only took into account antiferromagnetic correlations for nearest neighbors and ferromagnetic correlations for next-nearest neighbors. This scheme can correctly describe Néel order only. Another Schwinger boson mean-field theory by Wang [37] included antiferromagnetic correlations for both nearest and next-nearest neighbors. However, the author did not determine the phase diagram with respect to $J_2/J_1$. Generally speaking, both of ferromagnetic and antiferromagnetic correlations should be taken into account for frustrated models [100]. Another point is that both of the two studies assumed that the bond mean fields are independent of the directions of bonds. Therefore, these two schemes can not describe the phases which break the lattice rotational symmetry.

Exact diagonalization was first used by Fouet *et al.* [43] to study the $S = 1/2$ $J_1$-$J_2$-$J_3$ Heisenberg model on the honeycomb lattice for system sizes up to 32 spins. For $J_3 = 0$, they performed calculations for several typical values of $J_2$, and reported the following results. For $J_2/J_1 \lesssim 0.15$, the system remains Néel order. A staggered VBC phase appears around $J_2/J_1 = 0.4$, and for the intermediate frustration $J_2/J_1 = 0.3$, a resonating valence-bond (RVB) spin liquid [3] appears.

Mosadeq *et al.* [38] employed exact diagonalization both with the whole $S_z = 0$ bases and with the limited bases of nearest neighbor singlet valence bond (NNVB). By comparing the ground state energy between these two schemes, they found that for $0.2 < J_2/J_1 < 0.3$, the NNVB bases give a proper ground energy consistent with the exact results. Using NNVB bases, they calculated much larger system sizes up to 54 spins. They showed that for $0.2 < J_2/J_1 < 0.3$, the system favors a plaquette VBC order. By further increasing $J_2/J_1$, the system undergoes a phase transition to a staggered VBC state.

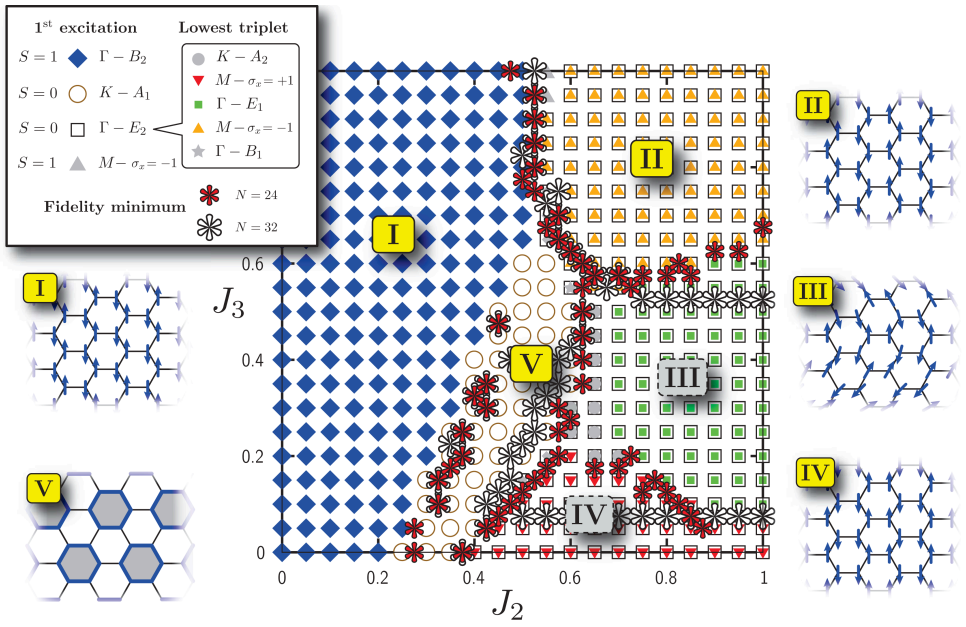


Figure 1.7: Phase diagram of the $S = 1/2$ $J_1$-$J_2$-$J_3$ Heisenberg model honeycomb lattice (with $J_1 \equiv 1$) in the region $J_2, J_3 \in [0, 1]$, based on exact diagonalization results. The five regions identified here correspond to: **(I)** a Néel ordered phase, **(II)** a collinear magnetically ordered phase corresponding to the striped phase in Ref. [53], **(III)** One or several phases corresponding to short or long range ordered non-collinear magnetic order, **(IV)** A different collinear magnetically ordered (or disordered) phase corresponding to the Néel-II phase in Ref. [53, 59] and **(V)** a magnetically disordered phase forming a plaquette VBC. The five phases are sketched in the panels around the phase diagram. Note that the phases highlighted in grey (III), (IV) show substantial finite size effects and are therefore difficult to characterize precisely.(from Ref. [50])

Recently, Albuquerque *et al.* [50] presented a comprehensive study of the phase diagram of $S = 1/2$ $J_1$-$J_2$-$J_3$ Heisenberg model on the honeycomb lattice, using a combination of exact diagonalizations of the original spin model up to 42 spins, a spin model with the NNVB basis up to 96 spins, and of an effective quantum dimer model up to 126 spins, as well as a self-consistent cluster mean-field theory. Their main results are summarized in Fig. 1.7. On the $J_3 = 0$ line, the boundary of the Néel phase is $J_2^c = 0.17 \sim 0.22$, which agrees well with the result of Schwinger boson mean-field theory by

Mattsson *et al.* [31]. Then a weak plaquette VBC phase (or a genuine spin liquid) appears up to a value of $J_2/J_1$ between 0.35 and 0.4. In this region, they did not clearly show whether a quantum spin liquid phase exists. For even larger values of $J_2/J_1$, a staggered VBC as well as spiral phases may appear but it is difficult to confirm it, since it is quite challenging for exact diagonalizations to study the incommensurate behavior. They also claimed that the staggered VBC phase may be actually the Néel-II phase at least in some region of $J_2/J_1$, since both break the same lattice symmetries.

There are two variational Monte Carlo studies recently, using different types of trial wave functions [39,40]. One was done by Clark *et al.* [39], based on comparison of energies of different phases, including generalized Huse-Elser states [87] and RVB states [88]. They concluded that the Néel state is favorable at $J_2/J_1 \lesssim 0.08$, and that a gapped spin liquid that is a sublattice pairing state [37] is favorable at $0.08 \lesssim J_2/J_1 \lesssim 0.3$. At high frustration ($J_2/J_1 \gtrsim 0.3$), the lattice rotational symmetry is broken, giving rise to a VBC state. Compared with the results of other approaches, their critical value $J_2/J_1 = 0.08$ is too small. Albuquerque *et al.* [50] compared the extrapolated ground state energy in their exact diagonalization with the one of Clark *et al.* [39] and claimed that this small value is due to a comparatively poor estimate of the energy of the Néel phase. The other variational study was done by Mezzacapo *et al.* [40], based on an entangled-plaquette variational ansatz [89], which includes a very broad class of entangled-plaquette states. Their estimate of the ground state energy is lower than Clark *et al.*'s result [39]. They found that the Néel order persists for $J_2/J_1 \lesssim 0.2$, whereas for $J_2/J_1 \gtrsim 0.4$, the Néel-II phase appears. In the intermediate region, it was found that all of the examined order parameters vanish in the thermodynamic limit. These order parameters include the square of sublattice magnetization and the plaquette VBC order parameter [38,50]. Therefore, it was concluded that the ground state is a quantum spin liquid. They claimed that the plaquette VBC phase predicted in exact diagonalization studies [38, 50] is due to the small lattice size in the calculations.

The series expansion study [45] of spin-1/2 $J_1$-$J_2$-$J_3$ Heisenberg model on the honeycomb lattice disagrees with most of the other studies on the

$J_3 = 0$ line, since it found no evidence of magnetically disordered phases. However, concerning the stability of the Néel phase, the critical value $J_2^c = 0.2$ agrees well with exact diagonalization [38, 50] and Schwinger boson mean-field theory [31]. For $J_3 > 0.2$, similar to the classical case, it predicts spiral phases, although their spiral angle is significantly renormalized from the classical value.

Reuther *et al.* [51] applied an unbiased pseudofermion functional renormalization group method to this model in the region of $0 \leq J_2, J_3 \leq 1$, and their main results are shown in Fig. 1.8. They found a large magnetically disordered region at intermediate $J_2$ couplings, in addition to Néel, collinear and spiral order regions. Along the $J_3 = 0$ line, the critical value of $J_2/J_1$ for the transition between the Néel phase and the disordered phase is $0.15 \pm 0.02$. As $J_2/J_1$ increases, they also found weak and competitive plaquette and staggered VBC orders for $J_2/J_1 < 0.4$, and claimed that the system is close to a quantum spin liquid. They suggested that this region is related to the expected spin liquid phase of the honeycomb Hubbard model [60, 66], and that introducing charge fluctuations may destroy the weak staggered VBC order. The region of $0.4 < J_2/J_1 < 0.6$ is clearly dominated by a sizable staggered VBC order. For $J_2/J_1 > 0.6$, the system shows a spiral order.

Bishop *et al.* [41] applied the coupled-cluster method to study the spin-1/2 $J_1$-$J_2$ honeycomb Heisenberg model, and later extended their study to include third-nearest neighbor couplings $J_3$ [53]. Their results for the $J_1$-$J_2$-$J_3$ model are summarized in Fig. 1.9. At $J_3 = 0$, the system shows the Néel order for $J_2/J_1 \lesssim 0.207 \pm 0.003$, and the Néel-II order for $J_2/J_1 \gtrsim 0.385 \pm 0.010$. In the intermediate region, a plaquette VBC phase may exist. However, it is difficult to determine the lower boundary of the plaquette VBC phase as accurately as the critical value $J_2/J_1 = 0.207 \pm 0.003$ of the Néel order. Therefore, they could not exclude the possibility of an intermediate phase (maybe a quantum spin liquid) in the range of $0.21 \lesssim J_2/J_1 \lesssim 0.24$.

Table. 1.2 summarizes earlier results of the magnetically disordered region in the quantum $J_1$-$J_2$ Heisenberg model on the single layer honeycomb lattice. It is clear shown that there is a growing consensus that a magnetically disordered region should exist in the intermediate $J_2/J_1$ region but the

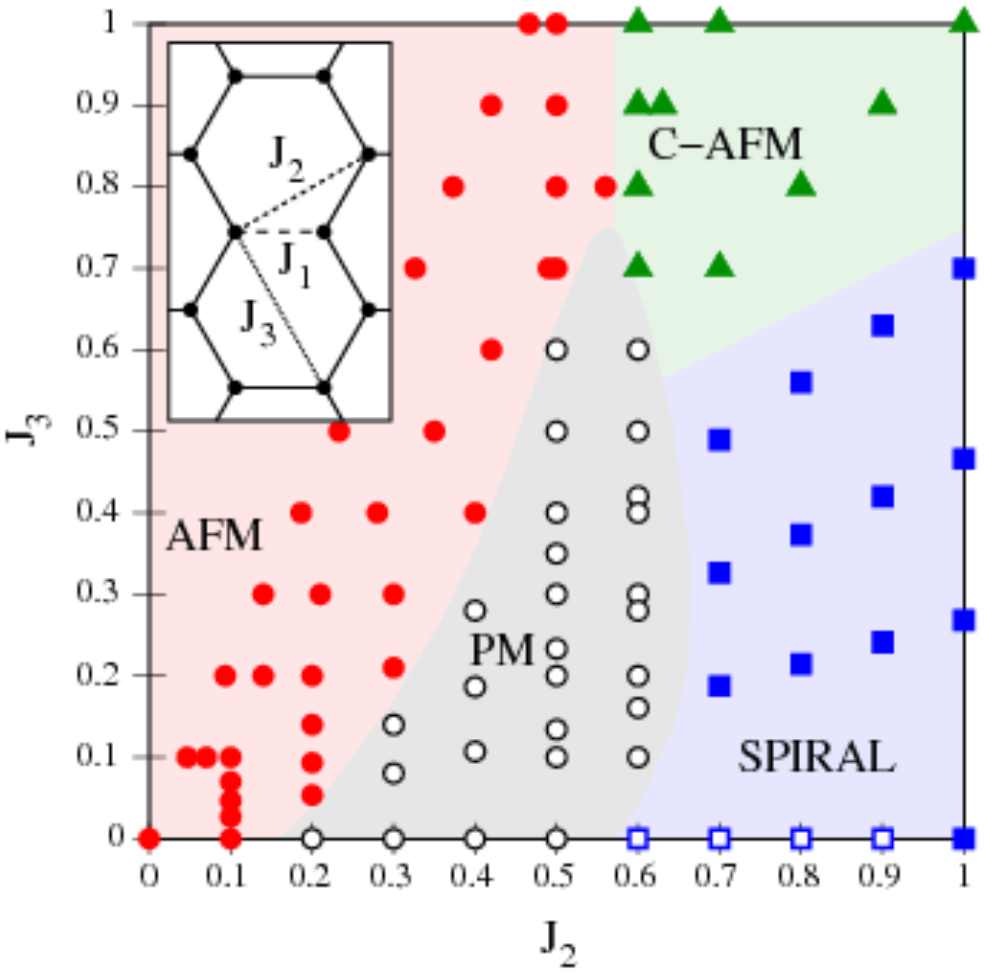


Figure 1.8: Phase diagram of the $S = 1/2$ $J_1$-$J_2$-$J_3$ Heisenberg model on the honeycomb lattice determined by pseudofermion functional renormalization group method. In the depicted $J_2 - J_3$ region ($J_1 \equiv 1$), AFM Néel order (red circles), collinear AFM (C-AFM) order (green triangles), spiral order (blue squares), and a paramagnetic phase (open circles) exist. The spiral-order phase partly shows incommensurability shifts from the spiral phase for dominant $J_2$(open blue squares indicate deviations from commensurability of more than 15%). (from Ref. [51])

nature of this region is controversial.

After our publication [55], there have appeared several works about this model studied by different approaches, including the density matrix renormalization group method [56–58] and the coupled cluster method [59]. We

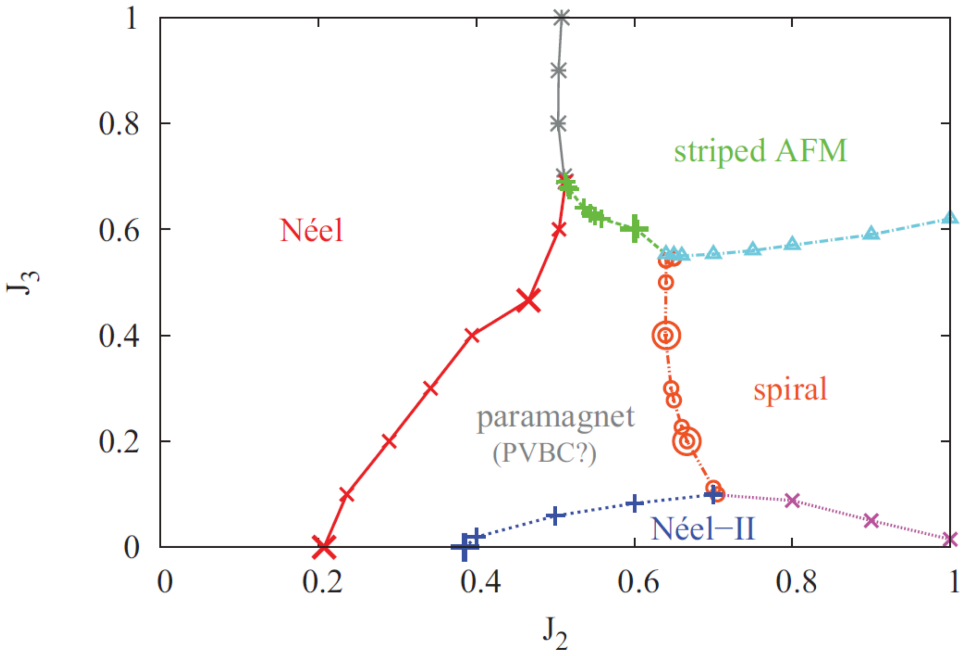


Figure 1.9: Phase diagram of the $S = 1/2$ $J_1$-$J_2$-$J_3$ Heisenberg model on the honeycomb lattice (with $J_1 \equiv 1$) determined by the coupled-cluster method. The five regions correspond to four quasiclassical phases with (a) AFM Néel order, (b) collinear AFM striped order, (c) spiral order, (d)Néel-II order, plus (e) a magnetically disordered phase which exhibits plaquette VBC order on a part of the boundary region. (from Ref. [53])

will review these results in Chapter 3.

### 1.3.2 Bilayer case

The $S = 1/2$ unfrustrated Heisenberg model on the bilayer square lattice, which is related to the well-known high-$T_c$ superconducting cuprates [71], has been studied extensively [72–81]. All of these studies show a Néel to dimer transition at zero temperature with increasing interlayer coupling $J_\perp$. Chubukov *et al.* [76] found an enhancement behavior of sublattice magnetization with increasing the interlayer coupling. There are a few works about the frustrated case on the bilayer square lattice [82–84]. Hida [82] found a spin gapped region in the phase diagram and this phase even persists in

| Method | Magnetically disordered region |
|---|---|
| ED [38] | $0.2 < J_2/J_1 < 0.3$ (PVBC), |
| | $J_2/J_1 > 0.3$ (SVBC) |
| ED [50] | $(0.17 \sim 0.22) < J_2/J_1 < (0.35 \sim 0.4)$ |
| | (weak PVBC or GSL) |
| VMC [39] | $0.08 \lesssim J_2/J_1 \lesssim 0.3$ (GSL), |
| | $J_2/J_1 \gtrsim 0.3$ (VBC) |
| VMC [40] | $0.2 \lesssim J_2/J_1 \lesssim 0.4$ (SL) |
| PFFRG [51] | $0.15 \pm 0.02 < J_2/J_1 < 0.4$ (weak PVBC or SVBC), |
| | $0.4 < J_2/J_1 < 0.6$ (SVBC) |
| CCM [41, 53] | $0.207 \pm 0.003 \lesssim J_2/J_1 \lesssim 0.385 \pm 0.010$ (PVBC) |

Table 1.2: Earlier results of the magnetically disordered region in the quantum $J_1$-$J_2$ Heisenberg model on the single layer honeycomb lattice by various methods. Here ED stands for exact diagonalization; VMC stands for variational Monte Carlo; PFFRG stands for pseudofermion functional renormalization group; CCM stands for coupled-cluster method; PVBC stands for plaquette VBC; SVBC stands for staggered VBC.

the single layer limit. He also observed the enhancement behavior of sublattice magnetization with increasing $J_\perp$ [83]. Yu *et al.* [84] did not find the enhancement behavior of sublattice magnetization with increasing $J_\perp$, therefore, their melting curve of Néel order does not show a reentrant behavior. For the honeycomb lattice case, there have been also a few studies about the bilayer case [32, 85, 86]. Using bond operator formalism and exact stochastic series expansion quantum Monte Carlo (QMC) calculations, Ganesh *et al.* [32, 85] studied the unfrustrated Heisenberg model on the bilayer honeycomb lattice, with in-plane nearest neighbor couplings $J_1$ and interlayer couplings $J_\perp$. For $S = 1/2$, 1 and 3/2, they determined the Néel to dimer transition points $J_{\perp c}$, which are summarized in Table. 1.3. There is a large discrepancy between the bond operator mean field results and QMC results, which increases for larger spin. For $S = 1/2$, including triplet-triplet interaction corrections by a variational approach leads to a transition point which agrees well with the QMC result. For $S = 1$ and 3/2, they included the high energy quintet modes, and obtained the transition points that agree within 5% with the QMC value.

| S | QMC | MFT | MFT + triplet interactions | MFT + quintet coupling |
|---|---|---|---|---|
| 1/2 | 1.645(1) | 1.312 | 1.588 | - |
| 1 | 4.785(1) | 3.498 | 3.774 | 4.80(9) |
| 3/2 | 9.194(3) | 6.559 | 6.837 | 9.58(18) |

Table 1.3: Value of $J_{\perp c}/J_1$ on the honeycomb lattice from different methods for different values of spin. MFT stands for mean field theory. (from Ref. [85])

Oitmaa *et al.* [86] used Ising and dimer series expansion to study this model. Their results of transition points are $J_\perp/J_1 = 1.66 \pm 0.01$ for $S = 1/2$ and $J_\perp/J_1 = 9.34 \pm 0.20$ for $S = 3/2$, which are in very good agreement with the QMC value [85]. For $S = 3/2$ case, they introduced the frustrating second-neighbor interaction $J_2$, and found that the increase of $J_2$ rapidly decreases the critical value of $J_\perp/J_1$. It was found that when $J_2/J_1 > 0.15$, a magnetically disordered phase appears at $J_\perp/J_1 < 2$, which may explain the quantum disordered ground state of $Bi_3Mn_4O_{12}(NO_3)$ [11].

## 1.4 Schwinger boson formalism

It is well known that the Schwinger boson mean-field theory provides a unified description for both magnetically ordered and disordered phases based on the resonating valence bond picture [3, 91–93]. A big advantage of this method is that it does not need to start from a magnetically ordered state in contrast to spin wave theory. A long-range magnetic order emerges naturally when the Schwinger bosons condense at some wave vector in the Brillouin zone [94–96]. At this wave vector, the excitation spectrum of the Schwinger bosons should be gapless. This picture has been put forward by Yoshioka [94, 95] for the first time in the antiferromagnetic Heisenberg model on the square lattice. In Ref. [94], it has been shown that the Schwinger bosons condensation appears at zero temperature, and the Néel order emerges. This method has been applied to the model with a magnetic field in Ref. [95]. On the other hand, if the Schwinger boson excitations are gapped in the

| | $E/JN$ | $m$ |
|---|---|---|
| Schwinger boson with one mean field $A$ | $-0.7119$ | 0.328 |
| Schwinger boson with two mean fields $AB$ | $-0.5697$ | 0.275 |
| QMC | $-0.5458(1)$ | 0.205(1) |

Table 1.4: Energy and magnetization of the 120° Néel ground state of the spin-$\frac{1}{2}$ Heisenberg antiferromagnet on the triangular lattice obtained by Schwinger boson mean-field approach with one mean field ($A$) [101] and two mean fields ($AB$) [98] as well as Quantum Monte Carlo (QMC) method [102].

whole Brillouin zone, the phase is magnetically disordered. In the following, we will use the rotationally invariant version of Schwinger boson mean field theory introduced by Ceccatto *et al.* [97–99]. The details of this method will be presented in Chapter 2. Chapter 3 uses an extension tailored for the bilayer lattice structure. This improved version of Schwinger boson formalism includes both ferromagnetic and antiferromagnetic correlations, which is particularly useful near transition points between ordered and disordered phases, because it treats antiferromagnetic and ferromagnetic correlations on equal footing [97–100]. This scheme has been tested to obtain results which show good agreements with more direct numerical methods, such as exact diagonalizations and quantum Monte Carlo method. The following is the comparison with the numerical data taken from the literature.

Table. 1.4 summarizes the results of the ground state energy and local magnetization of the spin-1/2 triangular Heisenberg model obtained by the Schwinger boson mean-field theory including antiferromagnetic correlations ($A$) [101], a similar theory but now with both ferromagnetic and antiferromagnetic correlations ($AB$) [98], and quantum Monte Carlo (QMC) simulations [102]. It is clear that the improved formalism which includes two types of mean fields provides much better results.

In Ref. [48], Cabra *et al.* have studied the spin-1/2 Heisenberg model on the $J_1$-$J_2$-$J_3$ honeycomb lattice with $J_2 = J_3$ with this improved Schwinger boson formalism. Fig. 1.10 shows the ground state energy per unit cell as a function of $J_2/J_1$ for a system of 32 sites and it is compared with the exact diagonalizations result. The agreement is quite nice.

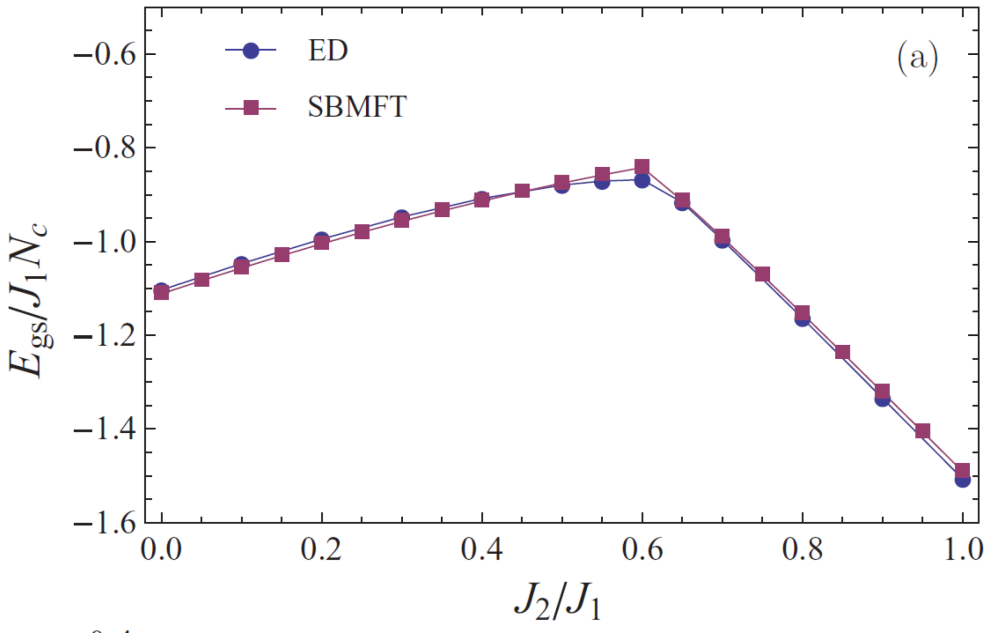


Figure 1.10: Ground state energy per unit cell as a function of $J_2/J_1$ for a lattice of 32 sites. The circles are exact diagonalizations results and the squares are the Schwinger boson mean-field theory results. (from Ref. [48])

Compared with other approaches, the biggest advantage of the Schwinger boson formalism is that it provides a unified way to treat both magnetically ordered and disordered phases and it is a versatile method which potentially allows for an estimation of all the phase boundaries, irrespective of whether the transition is first or second order. Therefore, it is possible to capture the overall structure of phase diagrams and indicate generally the nature of phases within the Schwinger boson formalism. For this reason, we will use the Schwinger boson formalism to study the frustrated honeycomb antiferromagnets throughout the thesis. Since we will include mean field approximations in this approach, we will also apply other methods to support the results of the Schwinger boson formalism.

## 1.5 Purpose and overview of this study

This thesis aims at studying the quantum disordered phases in the frustrated Heisenberg model on the single layer and bilayer honeycomb lattices. As we have summarized in Sec. 1.3, recently there are huge interests on possible magnetically disordered phases in the single layer case [36–41, 48–53]. However, these studies based on different methods have proposed conflicting physical scenarios. The most interesting part which is under debate is about the intermediate frustration ($J_2/J_1$) region and the issue is if exotic magnetically disordered ground states may appear. There are two major scenarios in previous studies. One is the plaquette VBC state which was proposed based on the results of exact diagonalizations [38, 50] and coupled-cluster method [41,53]. The other is a gapped spin liquid which was proposed based on the results of variational Monte Carlo methods [39, 40]. The results of these studies have already been explained in Sec. 1.3. It is well known that exact diagonalizations are possible only for rather small systems, but this method itself is exact. The coupled-cluster method starts from a selection of a suitable reference state, and its drawback is that it needs truncations of many spin configurations. The variational Monte Carlo methods are also approximate, and their predictive power depends on the choice of the trial wave functions. In addition, it also has finite size limitations. Since the physical scenarios from previous studies are conflicting and the approaches of these studies have various disadvantages as we have mentioned, it is interesting to use an improved approach to study the phase diagram of this region.

For the bilayer case, as we have summarized in Sec. 1.3, there is no theoretical investigation about the phase diagram of the frustrated Heisenberg model on the bilayer honeycomb lattice. In this thesis, we aim at determining its ground state phase diagram. There are two ways to introduce frustration in the bilayer systems. One is from the frustrating intralayer couplings, and the other is to include interlayer frustration. For the first case, as will be explained later, we have used an improved version of Schwinger boson mean-field theory to study the single layer case, and found some exotic disordered phases in the intermediate region of frustration [55]. It is a

natural extension to include the interlayer coupling $J_\perp$, and we expect some interesting disordered phases may emerge, especially for $S = 1/2$ due to the strong quantum fluctuations. The main issue in this part is the competition between the frustration coupling $J_2$ and the interlayer coupling $J_\perp$. After we obtain theoretical results, we will compare our theory with experimental results. The substitution of $Mn^{4+}$ in $Bi_3Mn_4O_{12}(NO_3)$ by $V^{4+}$ may realize the $S = 1/2$ Heisenberg model on the honeycomb lattice [11]. For the second case of introducing frustration, it is about interlayer couplings. In a certain region of the interlayer frustration, the model is exactly solvable and has an exact dimer product ground state. It is a natural extension to study the quantum phases of the model in the exchange parameter space near the part of the exact dimer state. We focus on the $S = 1/2$ case, where quantum fluctuations become more important, although some results remain valid for larger values of the spin, as we discuss in the following.

The present thesis is organized as follows. In Chapter 2, we explain the improved version of Schwinger boson mean-field theory and apply it to the spin-1/2 $J_1$-$J_2$ Heisenberg model on the honeycomb lattice. We focus on the possibility of exotic disordered phases induced by the frustration. We find a strong evidence for the existence of an intermediate disordered region where a spin gap opens and spin-spin correlations are short ranged in space. This magnetically disordered region turns out to quantitatively agree well with recent numerical simulation results [40, 41, 50, 53]. The key finding of our work is the presence of two kinds of magnetically disordered phases in this region. In the previous studies, only one kind of magnetically disordered phases has been proposed in the intermediate frustration region, such as a gapped spin liquid (GSL) state [39, 40] or the plaquette valence bond crystal (VBC) state [38, 41, 50, 53]. One of the two disordered phases is a GSL [8, 9] with short-range Néel correlations, maintaining the lattice translational and rotational symmetry. The other phase is a staggered VBC, which is also called lattice nematic [36]. This is nematic in the sense that this phase breaks lattice rotational symmetry, but preserves lattice translational symmetry. Spin liquids are interesting and important, since they have a prominent role in theories of high temperature superconductivity [3, 103] and the properties of

these states may have applications in quantum information [104]. VBC states are also interesting and important because they are useful in the experiment of studying Bose-Einstein condensation of magnons [105]. As we know, the strong quantum fluctuations induced by the low coordination number and the frustration tend to suppress the magnetic long-range order. As we will discuss in Chapter 2, the frustration due to the next nearest neighbor antiferromagnetic couplings tends to break the $C_3$ lattice rotational symmetry. The appearance of these two quantum disordered phases is the consequence of these two physical mechanisms, and should play an important role in the understanding of these physical concepts in frustrated magnets. Main results of Chapter 2 were published in Ref. [55].

In Chapter 3, we study the ground-state phase diagram of the frustrated Heisenberg model on the bilayer honeycomb lattice using the same method, complemented with the exact diagonalizations done by Lamas [90]and linear spin wave theory. We focus on the melting of Néel order and magnetically disordered phases induced by the frustration and interlayer couplings. We observe a novel reentrant behavior of the melting curve. This behavior is interesting and important because it clearly reflects the competition between the frustration from the next nearest neighbor antiferromagnetic couplings and the unfrustrated interlayer antiferromagnetic couplings. It should play an important role in the understanding of bilayer frustrated magnets. The behavior of the local magnetization gives a physical explanation to this effect, since the frustration coupling $J_2$ tends to melt the Néel order but a small $J_\perp$ has a tendency to stabilize magnetically orders. The results of mean-field calculations are compared to the exact diagonalizations done by Lamas [90]. Furthermore, the linear spin wave theory is used to describe the general behavior as a function of the spin $S$. Main results of Chapter 3 were published in Ref. [90].

In Chapter 4, we study the ground-state phase diagram of a frustrated Heisenberg model on the bilayer honeycomb lattice including interlayer frustration. We focus on both the properties of the quantum phases and determine the phase boundaries. In a region with the maximum interlayer frustration, the model is exactly solvable and has a dimerized ground state. This

result is valid for arbitrary site spin $S$. We explore the quantum phases of the model for the $S = 1/2$ case in the exchange parameter space surrounding the exact dimer state, using various complementary techniques, including bond operator (BO) approaches, Schwinger boson mean field theory (SB-MFT) and series expansion (SE) based on the continuous unitary transformation method. These studies will be complemented with exact diagonalization (ED) using Lanczos on finite size systems. Among these approaches, SE is mainly performed by M. Arlego and W. Brenig [106], and ED is mainly performed by C. A. Lamas [106]. Here bond operator approaches and series expansion are natural approaches to treat the interlayer dimer phase, since they are both exact in the fully decoupled dimer-product phase. SB-MFT is the only method used in our work, which potentially allows for an estimation of all critical lines, independently of the character of the transition, i.e. first or second order. We show results for ground state energies, spin gaps, spin correlation functions, and determine the quantum phase diagram, and then discuss the nature of the quantum phase transitions. Main results of Chapter 4 were published in Ref. [106].

Finally, we present our conclusions and perspectives in Chapter 5.

# Chapter 2

# Exotic disordered phases in the quantum $J_1$-$J_2$ model on the honeycomb lattice

This chapter presents our study of $S = 1/2$ frustrated $J_1$-$J_2$ Heisenberg antiferromagnetic model on the honeycomb lattice. In Sec. 2.1 we introduce our model and give a quick overview of the final phase diagram. In Sec. 2.2 we give a description of the Schwinger boson mean-field approach which we have used in this chapter. In Sec. 2.3, using the solutions of mean-field equations, we discuss the phase diagram, especially the magnetically disordered region. In Sec. 2.4, we summarize the present results and discuss the relation and comparison with earlier works about this model. Finally, in the end of this chapter, Sec. 2.5, we review the theoretical results after our publication, and compare our results with them.

## 2.1 Model and overview of the phase diagram

The $J_1$-$J_2$ Heisenberg model on the honeycomb lattice is given by

$$\hat{H} = J_1 \sum_{\langle \mathbf{xy} \rangle_1} \hat{\mathbf{S}}_\mathbf{x} \cdot \hat{\mathbf{S}}_\mathbf{y} + J_2 \sum_{\langle \mathbf{xy} \rangle_2} \hat{\mathbf{S}}_\mathbf{x} \cdot \hat{\mathbf{S}}_\mathbf{y}, \tag{2.1}$$

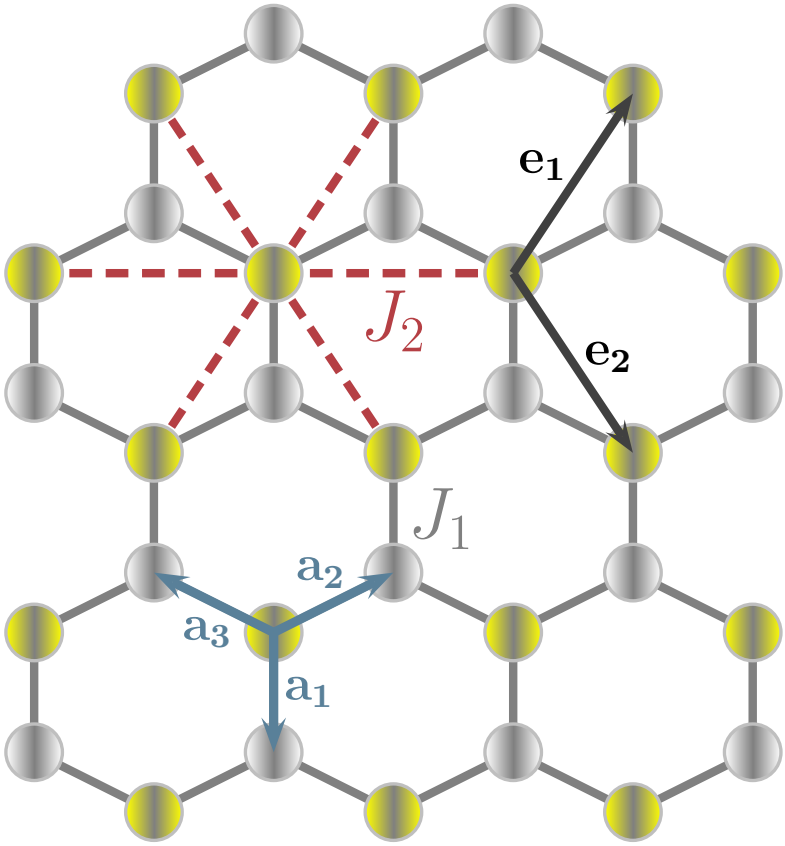


Figure 2.1: The honeycomb lattice with $J_1$ and $J_2$ couplings considered in this chapter. The lattice sites with different colors belong to different sublattices. The primitive translation vectors of the direct lattice are $\left[\mathbf{e}_1 = \left(\sqrt{3}/2, 3/2\right), \mathbf{e}_2 = \left(\sqrt{3}/2, -3/2\right)\right]$. $\mathbf{a}_1 = (0, -1), \mathbf{a}_2 = \left(\sqrt{3}/2, 1/2\right)$ and $\mathbf{a}_3 = \left(-\sqrt{3}/2, 1/2\right)$ correspond to the nearest neighbor bonds.

where $\hat{\mathbf{S}}_\mathbf{x}$ is the spin operator on site $\mathbf{x}$ and $\langle \mathbf{xy} \rangle_n$ indicates sum over the $n$-th neighbors (see Fig. 2.1). In this thesis we are interested in the antiferromagnetic case ($J_1, J_2 \geq 0$), and we focus on the region $J_2/J_1 \in [0, 0.5]$.

In the classical limit, $S \to \infty$, the model displays different zero temperature phases [42–44], see Fig. 2.2(a). For $J_2/J_1 < 1/6$, the system is Néel ordered, while for $J_2/J_1 > 1/6$, the system shows spiral phases. Details about the classical ground-state phase diagram are explained in the section 1.3.1. In this thesis, we study the Hamiltonian (2.1) in the strong quantum limit($S = 1/2$) using a rotationally invariant technique which has proven

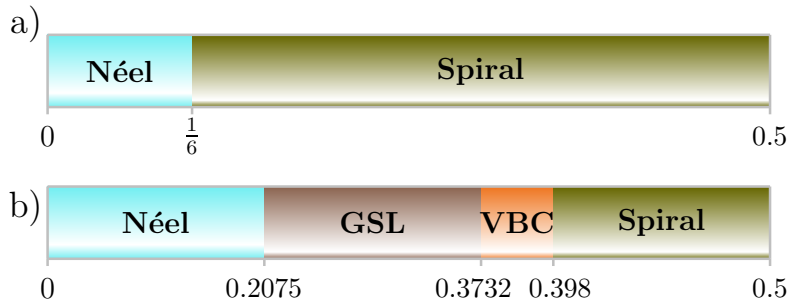


Figure 2.2: Phase diagram as a function of the frustration $J_2/J_1$. a) Classical phase diagram. b) Quantum phase diagram corresponding to $S = \frac{1}{2}$ obtained by means of the Schwinger boson mean-field theory.

successful in incorporating quantum fluctuations [48, 49, 97–100, 107–111].

Our main results are summarized in Fig. 2.2(b). The ground-state phase diagram is divided into four regions. [112] At small values of the frustrating coupling $J_2/J_1$, the system presents a Néel-like ground state. By increasing the frustration, we find at $J_2/J1 \simeq 0.2075$ a continuous transition to a gapped spin liquid phase. When the value of the frustrating coupling exceeds $J_2/J_1 \simeq 0.3732$, we find a continuous transition into a staggered VBC (lattice nematic) with broken $C_3$ symmetry, which transforms at $J_2/J_1 \simeq 0.398$ into a spiral phase.

## 2.2 Schwinger boson mean-field approach

Now we present the formulation of Schwinger boson mean-field approach which we use in this chapter. Following Schwinger [113], the spin operator $\hat{\mathbf{S}}_{\mathbf{R}}$ at each lattice site is replaced by the two pieces of Schwinger bosons $\hat{b}_{\mathbf{R}\mu}$,$(\mu = \uparrow, \downarrow)$ as

$$\hat{\mathbf{S}}_{\mathbf{R}} = \frac{1}{2} \begin{pmatrix} \hat{b}^{\dagger}_{\mathbf{R}\uparrow} & \hat{b}^{\dagger}_{\mathbf{R}\downarrow} \end{pmatrix} \sigma \begin{pmatrix} \hat{b}_{\mathbf{R}\uparrow} \\ \hat{b}_{\mathbf{R}\downarrow} \end{pmatrix}, \tag{2.2}$$

Here $\hat{b}^{\dagger}_{\mathbf{R}\mu}$ creates a boson on site $\mathbf{R}$ with spin $\mu$, and $\sigma = (\sigma^x, \sigma^y, \sigma^z)$ is the vector of Pauli matrices. To fix the magnitude of the spin, we need to have $\sum_{\mu} \hat{b}^{\dagger}_{\mathbf{R}\mu} \hat{b}_{\mathbf{R}\mu} = 2S$ bosons per site.

Now we are ready to follow Arovas and Auerbach [91–93] and intro-

duce two types of bond operators: the RVB-type bond operators $\hat{A}_{\mathbf{R},\mathbf{R}+\delta} = \frac{1}{2}\left(\hat{b}_{\mathbf{R}\uparrow}\hat{b}_{\mathbf{R}+\delta\downarrow} - \hat{b}_{\mathbf{R}\downarrow}\hat{b}_{\mathbf{R}+\delta\uparrow}\right)$ and $\hat{B}_{\mathbf{R},\mathbf{R}+\delta} = \frac{1}{2}\left(\hat{b}^{\dagger}_{\mathbf{R}\uparrow}\hat{b}_{\mathbf{R}+\delta\uparrow} + \hat{b}^{\dagger}_{\mathbf{R}\downarrow}\hat{b}_{\mathbf{R}+\delta\downarrow}\right)$. Therefore we can decompose the Hamiltonian as:

$$\begin{aligned}\hat{H} &= J_1 \sum_{\mathbf{r}^{(1)},m}\left(:\hat{B}^{\dagger}_{\mathbf{r}^{(1)},\mathbf{r}^{(1)}+\alpha_m}\hat{B}_{\mathbf{r}^{(1)},\mathbf{r}^{(1)}+\alpha_m}: -\hat{A}^{\dagger}_{\mathbf{r}^{(1)},\mathbf{r}^{(1)}+\alpha_m}\hat{A}_{\mathbf{r}^{(1)},\mathbf{r}^{(1)}+\alpha_m}\right) \\ &+J_2\left[\sum_{\mathbf{r}^{(1)},m}\left(:\hat{B}^{\dagger}_{\mathbf{r}^{(1)},\mathbf{r}^{(1)}+\beta_m}\hat{B}_{\mathbf{r}^{(1)},\mathbf{r}^{(1)}+\beta_m}: -\hat{A}^{\dagger}_{\mathbf{r}^{(1)},\mathbf{r}^{(1)}+\beta_m}\hat{A}_{\mathbf{r}^{(1)},\mathbf{r}^{(1)}+\beta_m}\right)\right. \\ &\left.+\sum_{\mathbf{r}^{(2)},m}\left(:\hat{B}^{\dagger}_{\mathbf{r}^{(2)},\mathbf{r}^{(2)}+\beta_m}\hat{B}_{\mathbf{r}^{(2)},\mathbf{r}^{(2)}+\beta_m}: -\hat{A}^{\dagger}_{\mathbf{r}^{(2)},\mathbf{r}^{(2)}+\beta_m}\hat{A}_{\mathbf{r}^{(2)},\mathbf{r}^{(2)}+\beta_m}\right)\right] \quad (2.3)\end{aligned}$$

where $\mathbf{r}^{(1)}$ and $\mathbf{r}^{(2)}$ are the positions of lattice sites of sublattice 1 and 2. $\alpha_m$ are the nearest neighbor vectors and $\beta_m$ are three of the next nearest neighbor vectors:

$$\alpha_1 = -\mathbf{e}_y, \qquad \beta_1 = -\frac{\sqrt{3}}{2}\mathbf{e}_x - \frac{3}{2}\mathbf{e}_y, \quad (2.4)$$

$$\alpha_2 = \frac{\sqrt{3}}{2}\mathbf{e}_x + \frac{1}{2}\mathbf{e}_y, \qquad \beta_2 = -\frac{\sqrt{3}}{2}\mathbf{e}_x + \frac{3}{2}\mathbf{e}_y, \quad (2.5)$$

$$\alpha_3 = -\frac{\sqrt{3}}{2}\mathbf{e}_x + \frac{1}{2}\mathbf{e}_y, \qquad \beta_3 = -\sqrt{3}\mathbf{e}_x, \quad (2.6)$$

where the unit vector is the lattice constant. The lattice point of $\mathbf{r}^{(1)} + \alpha_m$ is a position of the sublattice 2, and $\mathbf{r}^{(i)} + \beta_m$ is a position of the sublattice $i$ ($i = 1, 2$). The double dots (: ... :) indicate the normal ordering of operators $\hat{b}$ and $\hat{b}^{\dagger}$. One of the advantages of this rotational invariant decomposition is that it enables us to treat ferromagnetism and antiferromagnetism on equal footing. This decomposition has been successfully used to describe quantum disordered phases in two-dimensional frustrated antiferromagnets [48, 49, 97, 99, 109–111].

Then we apply the mean-field approximation to this Hamiltonian, and the order parameters are assumed to be uniform in space but dependent on the directions of bonds:

$$
\begin{aligned}
A_m &\equiv \left\langle \hat{A}_{\mathbf{r}^{(1)},\mathbf{r}^{(1)}+\alpha_m} \right\rangle, \qquad & B_m &\equiv \left\langle \hat{B}_{\mathbf{r}^{(1)},\mathbf{r}^{(1)}+\alpha_m} \right\rangle, \\
A_m^{(n)} &\equiv \left\langle \hat{A}_{\mathbf{r}^{(n)},\mathbf{r}^{(n)}+\beta_m} \right\rangle, \qquad & B_m^{(n)} &\equiv \left\langle \hat{B}_{\mathbf{r}^{(n)},\mathbf{r}^{(n)}+\beta_m} \right\rangle
\end{aligned} \tag{2.7}
$$

with $n$=1,2 for different sublattices and $m$=1,2,3 for the directions of bonds.

By using the Hartree-Fock decoupling:

$$
\begin{aligned}
\hat{A}^{\dagger}_{\mathbf{r}^{(1)},\mathbf{r}^{(1)}+\alpha_m}\hat{A}_{\mathbf{r}^{(1)},\mathbf{r}^{(1)}+\alpha_m} &\longrightarrow A_m^{*}\hat{A}_{\mathbf{r}^{(1)},\mathbf{r}^{(1)}+\alpha_m} + A_m\hat{A}^{\dagger}_{\mathbf{r}^{(1)},\mathbf{r}^{(1)}+\alpha_m} \\
&\quad - |A_m|^2, \\
\hat{A}^{\dagger}_{\mathbf{r}^{(n)},\mathbf{r}^{(n)}+\beta_m}\hat{A}_{\mathbf{r}^{(n)},\mathbf{r}^{(n)}+\beta_m} &\longrightarrow A_m^{(n)*}\hat{A}_{\mathbf{r}^{(n)},\mathbf{r}^{(n)}+\beta_m} + A_m^{(n)}\hat{A}^{\dagger}_{\mathbf{r}^{(n)},\mathbf{r}^{(n)}+\beta_m} \\
&\quad - \left|A_m^{(n)}\right|^2, \\
:\hat{B}^{\dagger}_{\mathbf{r}^{(1)},\mathbf{r}^{(1)}+\alpha_m}\hat{B}_{\mathbf{r}^{(1)},\mathbf{r}^{(1)}+\alpha_m}: &\longrightarrow B_m^{*}\hat{B}_{\mathbf{r}^{(1)},\mathbf{r}^{(1)}+\alpha_m} + B_m\hat{B}^{\dagger}_{\mathbf{r}^{(1)},\mathbf{r}^{(1)}+\alpha_m} \\
&\quad - |B_m|^2, \\
:\hat{B}^{\dagger}_{\mathbf{r}^{(n)},\mathbf{r}^{(n)}+\beta_m}\hat{B}_{\mathbf{r}^{(n)},\mathbf{r}^{(n)}+\beta_m}: &\longrightarrow B_m^{(n)*}\hat{B}_{\mathbf{r}^{(n)},\mathbf{r}^{(n)}+\beta_m} + B_m^{(n)}\hat{B}^{\dagger}_{\mathbf{r}^{(n)},\mathbf{r}^{(n)}+\beta_m} \\
&\quad - \left|B_m^{(n)}\right|^2,
\end{aligned} \tag{2.8}
$$

we can generate the mean-field Hamiltonian:

$$
\begin{aligned}
\hat{H}_{MF} &= J_1 \sum_{\mathbf{r}^{(1)},m} \left[ \left( B_m^{*}\hat{B}_{\mathbf{r}^{(1)},\mathbf{r}^{(1)}+\alpha_m} - A_m^{*}\hat{A}_{\mathbf{r}^{(1)},\mathbf{r}^{(1)}+\alpha_m} \right) + h.c. \right. \\
&\quad \left. - \left( |B_m|^2 - |A_m|^2 \right) \right] \\
&\quad + J_2 \sum_{n} \sum_{\mathbf{r}^{(n)},m} \left[ \left( B_m^{(n)*}\hat{B}_{\mathbf{r}^{(n)},\mathbf{r}^{(n)}+\beta_m} - A_m^{(n)*}\hat{A}_{\mathbf{r}^{(n)},\mathbf{r}^{(n)}+\beta_m} \right) + h.c. \right. \\
&\quad \left. - \left( \left|B_m^{(n)}\right|^2 - \left|A_m^{(n)}\right|^2 \right) \right].
\end{aligned}
$$

The constraint about the boson number is enforced by a Lagrange multiplier $\lambda_{\mathbf{R}}$ at each site. We replace the local Lagrange multipliers $\lambda_{\mathbf{R}}$ by parameters $\lambda^{(n)}$ for each sublattice, which is a crucial approximation in Schwinger bosons mean-field theory:

$$
\hat{H}_{MF} \rightarrow \hat{H}_{MF} + \hat{H}_{\lambda} \tag{2.9}
$$

with

$$\hat{H}_\lambda = \sum_n \lambda^{(n)} \sum_{\mathbf{r}^{(n)}} \left( \sum_\mu \hat{b}^\dagger_{\mathbf{r}^{(n)}\mu} \hat{b}_{\mathbf{r}^{(n)}\mu} - 2S \right). \tag{2.10}$$

After Fourier transforming the Schwinger bosons on each sublattice:

$$\hat{b}_{\mathbf{r}^{(n)}\mu} = \frac{1}{\sqrt{N/2}} \sum_{\mathbf{k}\in BZ} \hat{b}^{(n)}_{\mathbf{k}\mu} \exp\left(i\mathbf{k}\cdot\mathbf{r}^{(n)}\right), \tag{2.11}$$

where $N$ is the number of lattice sites, one arrives at the mean field Hamiltonian in a compact form. (In the following we will assume the mean fields $A$ and $B$ to be real):

$$\hat{H}_{MF} = \sum_{\mathbf{k}} \hat{\phi}^\dagger_{\mathbf{k}} M_{\mathbf{k}} \hat{\phi}_{\mathbf{k}} + E_0 \tag{2.12}$$

where we introduce the bosonic Nambu spinor in the momentum space:

$$\hat{\phi}_{\mathbf{k}} = \left( \begin{array}{cccc} \hat{b}^{(1)}_{\mathbf{k}\uparrow} & \hat{b}^{(2)}_{\mathbf{k}\uparrow} & \hat{b}^{(1)\dagger}_{-\mathbf{k}\downarrow} & \hat{b}^{(2)\dagger}_{-\mathbf{k}\downarrow} \end{array} \right)^{\mathsf{T}}, \tag{2.13}$$

and

$$\begin{aligned} -E_0 &= \frac{N}{2} J_1 \sum_m \left(B_m^2 - A_m^2\right) + \frac{N}{2} J_2 \sum_{n,m} \left[ \left(B_m^{(n)}\right)^2 - \left(A_m^{(n)}\right)^2 \right] \\ &\quad + (2S+1)\frac{N}{2}\left(\lambda^{(1)} + \lambda^{(2)}\right). \end{aligned} \tag{2.14}$$

The $4 \times 4$ dynamical matrix $M_{\mathbf{k}}$ is given by

$$M_{\mathbf{k}} = \left( \begin{array}{cc} \Gamma^B_{\mathbf{k}} + \Lambda & -\Gamma^A_{\mathbf{k}} \\ \Gamma^A_{\mathbf{k}} & \Gamma^B_{\mathbf{k}} + \Lambda \end{array} \right), \tag{2.15}$$

where

$$\Lambda = \left( \begin{array}{cc} \lambda^{(1)} & 0 \\ 0 & \lambda^{(2)} \end{array} \right), \tag{2.16}$$

$$\Gamma^B_{\mathbf{k}} = \left( \begin{array}{cc} J_2 \sum_m B_m^{(1)} \cos\left(\mathbf{k}\cdot\beta_m\right) & \frac{J_1}{2} \sum_m B_m \exp\left(i\mathbf{k}\cdot\alpha_m\right) \\ \frac{J_1}{2} \sum_m B_m \exp\left(-i\mathbf{k}\cdot\alpha_m\right) & J_2 \sum_m B_m^{(2)} \cos\left(\mathbf{k}\cdot\beta_m\right) \end{array} \right), \tag{2.17}$$

$$\Gamma_{\mathbf{k}}^{A} = \begin{pmatrix} iJ_2 \sum_m A_m^{(1)} \sin(\mathbf{k}\cdot\beta_m) & \frac{J_1}{2}\sum_m A_m \exp(i\mathbf{k}\cdot\alpha_m) \\ -\frac{J_1}{2}\sum_m A_m \exp(-i\mathbf{k}\cdot\alpha_m) & iJ_2 \sum_m A_m^{(2)} \sin(\mathbf{k}\cdot\beta_m) \end{pmatrix} \quad (2.18)$$

It is clear that $M_{\mathbf{k}}$ is a Hermitian matrix, since $\Lambda^{\dagger} = \Lambda$, $\left(\Gamma_{\mathbf{k}}^{B}\right)^{\dagger} = \Gamma_{\mathbf{k}}^{B}$, and $\left(\Gamma_{\mathbf{k}}^{A}\right)^{\dagger} = -\Gamma_{\mathbf{k}}^{A}$.

The diagonalization of the mean-field Hamiltonian amounts to a homogeneous linear transformation of the set of destruction operators $\hat{\phi}_{\mathbf{k}}$ into a suitable analogous set of destruction operators $\hat{\psi}_{\mathbf{k}}$ as $\hat{\phi}_{\mathbf{k}} = F_{\mathbf{k}}\hat{\psi}_{\mathbf{k}}$. The transformation matrix $F_{\mathbf{k}}$ should transform $\hat{H}_{MF}$ into a diagonal form according to the scheme

$$\sum_{\mathbf{k}} \hat{\phi}_{\mathbf{k}}^{\dagger} M_{\mathbf{k}} \hat{\phi}_{\mathbf{k}} = \sum_{\mathbf{k}} \hat{\psi}_{\mathbf{k}}^{\dagger} F_{\mathbf{k}}^{\dagger} M_{\mathbf{k}} F_{\mathbf{k}} \hat{\psi}_{\mathbf{k}} = \sum_{\mathbf{k}} \hat{\psi}_{\mathbf{k}}^{\dagger} \xi_{\mathbf{k}} \hat{\psi}_{\mathbf{k}}, \quad (2.19)$$

where $\xi_{\mathbf{k}}$ is a diagonal matrix, and hold that the $\psi_{\mathbf{k}}$ constitutes a set of boson operators. Therefore, $F_{\mathbf{k}}$ should be the so-called para-unitary matrix which satisfies $F_{\mathbf{k}}\hat{\varphi}F_{\mathbf{k}}^{\dagger} = \hat{\varphi}$ or $F_{\mathbf{k}}^{\dagger}\hat{\varphi}F_{\mathbf{k}} = \hat{\varphi}$ or $F_{\mathbf{k}}^{\dagger}\hat{\varphi} = \hat{\varphi}F_{\mathbf{k}}^{-1}$, where the para-unit matrix $\hat{\varphi} \equiv \mathrm{diag}(1, 1, -1, -1)$, and the inverse $F_{\mathbf{k}}^{-1}$ of a para-unitary matrix $F_{\mathbf{k}}$ is also para-unitary [114]. Using the properties of the para-unitary matrix, we obtain

$$\hat{\varphi}M_{\mathbf{k}}F_{\mathbf{k}} = F_{\mathbf{k}}\hat{\varphi}F_{\mathbf{k}}^{\dagger}M_{\mathbf{k}}F_{\mathbf{k}} = F_{\mathbf{k}}\hat{\varphi}\xi_{\mathbf{k}}. \quad (2.20)$$

Therefore,

$$F_{\mathbf{k}}^{-1}\hat{\varphi}M_{\mathbf{k}}F_{\mathbf{k}} = \hat{\varphi}\xi_{\mathbf{k}}, \quad (2.21)$$

where the columns of $F_{\mathbf{k}}$ are the eigenvectors of the matrix $\hat{\varphi}M_{\mathbf{k}}$, and the diagonal elements of $\hat{\varphi}\xi_{\mathbf{k}}$ are the corresponding eigenvalues. Through solving the equation

$$\mathtt{det}\left(\omega I_0 - \hat{\varphi}M_{\mathbf{k}}\right) = 0, \quad (2.22)$$

we get two branches $\omega_{\pm}(\mathbf{k})$, and each branch is doubly degenerate. Inserting the eigenvalues into $(\omega I_0 - \hat{\varphi}M_{\mathbf{k}})\,\mathbf{X}(\mathbf{k}) = 0$, we can get the corresponding eigenvectors which are the columns of $F_{\mathbf{k}}$. Therefore, the mean-field Hamil-

tonian is diagonalized as follows:

$$\begin{aligned}\hat{H}_{MF} &= \sum_{\mathbf{k}} \left( \begin{array}{cccc} \hat{\alpha}^{\dagger}_{\mathbf{k}\uparrow} & \hat{\beta}^{\dagger}_{\mathbf{k}\uparrow} & \hat{\alpha}_{-\mathbf{k}\downarrow} & \hat{\beta}_{-\mathbf{k}\downarrow} \end{array} \right) \cdot \mathbf{E}\left(\mathbf{k}\right) \cdot \left( \begin{array}{c} \hat{\alpha}_{\mathbf{k}\uparrow} \\ \hat{\beta}_{\mathbf{k}\uparrow} \\ \hat{\alpha}^{\dagger}_{-\mathbf{k}\downarrow} \\ \hat{\beta}^{\dagger}_{-\mathbf{k}\downarrow} \end{array} \right) + E_0 \\ &= \sum_{\mathbf{k}} \left[ \omega_+\left(\mathbf{k}\right) \left( \hat{\alpha}^{\dagger}_{\mathbf{k}\uparrow} \hat{\alpha}_{\mathbf{k}\uparrow} + \hat{\alpha}^{\dagger}_{-\mathbf{k}\downarrow} \hat{\alpha}_{-\mathbf{k}\downarrow} \right) + \omega_-\left(\mathbf{k}\right) \left( \hat{\beta}^{\dagger}_{-\mathbf{k}\uparrow} \hat{\beta}_{-\mathbf{k}\uparrow} + \hat{\beta}^{\dagger}_{\mathbf{k}\downarrow} \hat{\beta}_{\mathbf{k}\downarrow} \right) \right] \\ &\quad + \sum_{\mathbf{k}} \left( \omega_+\left(\mathbf{k}\right) + \omega_-\left(\mathbf{k}\right) \right) + E_0, \end{aligned} \tag{2.23}$$

where $\mathbf{E}\left(\mathbf{k}\right)$ =diag$(\omega_+\left(\mathbf{k}\right), \omega_-\left(\mathbf{k}\right), \omega_+\left(\mathbf{k}\right), \omega_-\left(\mathbf{k}\right))$. Such a para-unitary diagonalization is done numerically. The ground-state energy is given by $E_{gs} = \sum_{\mathbf{k}} \left( \omega_+\left(\mathbf{k}\right) + \omega_-\left(\mathbf{k}\right) \right) + E_0$ in the zero temperature case, and the free energy at the temperature $T = 1/\beta$ is

$$\begin{aligned} F &= -\frac{1}{\beta} \ln\left( \mathrm{Tr} e^{-\beta H_{MF}} \right) \\ &= \sum_{\mathbf{k}} \left[ \frac{2}{\beta} \left( \ln\left( 1 - e^{-\beta \omega_+(\mathbf{k})} \right) + \ln\left( 1 - e^{-\beta \omega_-(\mathbf{k})} \right) \right) \right. \\ &\quad \left. + \omega_+\left(\mathbf{k}\right) + \omega_-\left(\mathbf{k}\right) \right] + E_0. \end{aligned} \tag{2.24}$$

The mean-field equations yield the order parameters that minimize the free energy (finite temperature) or the ground-state energy (zero temperature). On the other hand, from the inverse of the Bogoliubov transformation matrix [114]

$$F_{\mathbf{k}} = \left( \begin{array}{cc} U_{\mathbf{k}} & -V_{\mathbf{k}} \\ V_{\mathbf{k}} & U_{\mathbf{k}} \end{array} \right), \tag{2.25}$$

we can establish the mean-field equations of the zero temperature case by calculating the expectation values of corresponding operators directly:

$$A_m = \frac{1}{2} \times \frac{2}{N} \sum_{\mathbf{k},\mathbf{k}'} \exp\left[ i\mathbf{k} \cdot \mathbf{r}^{(1)} + i\mathbf{k}' \cdot \left( \mathbf{r}^{(1)} + \alpha_m \right) \right] \left( \left\langle \hat{b}^{(1)}_{\mathbf{k}\uparrow} \hat{b}^{(2)}_{\mathbf{k}'\downarrow} \right\rangle - \left\langle \hat{b}^{(1)}_{\mathbf{k}\downarrow} \hat{b}^{(2)}_{\mathbf{k}'\uparrow} \right\rangle \right)$$

$$= \frac{1}{N}\sum_{\mathbf{k}}\left[\left(U_{\mathbf{k}}V_{\mathbf{k}}^{\dagger}\right)_{12}\exp\left(-i\mathbf{k}\cdot\alpha_m\right)+c.c.\right], \tag{2.26}$$

$$\begin{aligned} A_m^{(n)} &= \frac{1}{2}\times\frac{2}{N}\sum_{\mathbf{k},\mathbf{k}'}\exp\left[i\mathbf{k}\cdot\mathbf{r}^{(n)}+i\mathbf{k}'\cdot\left(\mathbf{r}^{(n)}+\beta_m\right)\right]\left(\left\langle\hat{b}_{\mathbf{k}\uparrow}^{(n)}\hat{b}_{\mathbf{k}'\downarrow}^{(n)}\right\rangle-\left\langle\hat{b}_{\mathbf{k}\downarrow}^{(n)}\hat{b}_{\mathbf{k}'\uparrow}^{(n)}\right\rangle\right) \\ &= \frac{1}{N}\sum_{\mathbf{k}}\left[\left(U_{\mathbf{k}}V_{\mathbf{k}}^{\dagger}\right)_{nn}\exp\left(-i\mathbf{k}\cdot\beta_m\right)+c.c.\right], \qquad (n=1,2) \end{aligned} \tag{2.27}$$

$$\begin{aligned} B_m &= \frac{1}{2}\times\frac{2}{N}\sum_{\mathbf{k},\mathbf{k}'}\exp\left[-i\mathbf{k}\cdot\mathbf{r}^{(1)}+i\mathbf{k}'\cdot\left(\mathbf{r}^{(1)}+\alpha_m\right)\right]\left(\left\langle\hat{b}_{\mathbf{k}\uparrow}^{(1)\dagger}\hat{b}_{\mathbf{k}'\uparrow}^{(2)}\right\rangle+\left\langle\hat{b}_{\mathbf{k}\downarrow}^{(1)\dagger}\hat{b}_{\mathbf{k}'\downarrow}^{(2)}\right\rangle\right) \\ &= \frac{1}{N}\sum_{\mathbf{k}}\left[\left(V_{\mathbf{k}}V_{\mathbf{k}}^{\dagger}\right)_{12}\exp\left(-i\mathbf{k}\cdot\alpha_m\right)+c.c.\right], \end{aligned} \tag{2.28}$$

$$\begin{aligned} B_m^{(n)} &= \frac{1}{2}\times\frac{2}{N}\sum_{\mathbf{k},\mathbf{k}'}\exp\left[-i\mathbf{k}\cdot\mathbf{r}^{(n)}+i\mathbf{k}'\cdot\left(\mathbf{r}^{(n)}+\beta_m\right)\right]\left(\left\langle\hat{b}_{\mathbf{k}\uparrow}^{(n)\dagger}\hat{b}_{\mathbf{k}'\uparrow}^{(n)}\right\rangle+\left\langle\hat{b}_{\mathbf{k}\downarrow}^{(n)\dagger}\hat{b}_{\mathbf{k}'\downarrow}^{(n)}\right\rangle\right) \\ &= \frac{1}{N}\sum_{\mathbf{k}}\left[\left(V_{\mathbf{k}}V_{\mathbf{k}}^{\dagger}\right)_{nn}\exp\left(-i\mathbf{k}\cdot\beta_m\right)+c.c.\right]. \qquad (n=1,2) \end{aligned} \tag{2.29}$$

The two constraints in the number of Schwinger bosons can be written in the momentum space as

$$\begin{aligned} 2S &= \frac{2}{N}\sum_{\mathbf{k},\mathbf{k}'}\exp\left[i\left(\mathbf{k}'-\mathbf{k}\right)\cdot\mathbf{r}^{(n)}\right]\left(\left\langle\hat{b}_{\mathbf{k}\uparrow}^{(n)\dagger}\hat{b}_{\mathbf{k}'\uparrow}^{(n)}\right\rangle+\left\langle\hat{b}_{\mathbf{k}\downarrow}^{(n)\dagger}\hat{b}_{\mathbf{k}'\downarrow}^{(n)}\right\rangle\right) \\ &= \frac{2}{N}\sum_{\mathbf{k}}\left[\left(V_{\mathbf{k}}V_{\mathbf{k}}^{\dagger}\right)_{nn}+c.c.\right]. \qquad (n=1,2) \end{aligned} \tag{2.30}$$

We need to solve 18 coupled nonlinear mean-field equations for the order parameters $A$ and $B$, plus two constraint equations for the Lagrange multipliers $\lambda^{(n)}$. They are solved numerically on finite but very large lattices with periodic boundary conditions (up to 5000 lattice sites in the present work), and then we extrapolate the results to the thermodynamic limit of the system size. As we have shown in Fig. 2.1, the lattice translation vectors are $\mathbf{e}_1=\left(\sqrt{3}/2,3/2\right)$ and $\mathbf{e}_2=\left(\sqrt{3}/2,-3/2\right)$, where the unit is the distance

between the nearest neighbor sites. Therefore, the reciprocal lattice vectors are $\mathbf{b}_1 = \left(2\pi/\sqrt{3}, 2\pi/3\right)$ and $\mathbf{b}_2 = \left(2\pi/\sqrt{3}, -2\pi/3\right)$. We consider the system on a torus of the size $L\mathbf{e}_1 \times L\mathbf{e}_2$ with the periodic boundary condition in both of the directions. The mesh of the $\mathbf{k}$ summation is

$$\begin{aligned} \mathbf{k} &= \frac{n_1}{L}\mathbf{b}_1 + \frac{n_2}{L}\mathbf{b}_2 \\ &= \left(\frac{2\pi}{\sqrt{3}L}\left(n_1+n_2\right), \frac{2\pi}{3L}\left(n_1-n_2\right)\right), \end{aligned} \tag{2.31}$$

with

$$-L/2 \le n_1 < L/2, \qquad -L/2 \le n_2 < L/2. \tag{2.32}$$

We have studied systems of sizes $N = 2L^2$, with $L = 8, 14, 20, 26, 32, 38, 44, 50$ to extrapolate to $N \to \infty$. In Fig. 2.3, we show two examples of the extrapolation of the gap in the boson dispersion: in Fig. 2.3(a) the extrapolated gap at $J_2/J_1 = 0.16$ is zero, while in Fig. 2.3(b) the extrapolated gap at $J_2/J_1 = 0.29$ is 0.0808. The fitting function is a fourth order polynomial function of $1/L$, and the optimized one is $0.0808 - 0.0058/L + 0.292/L^2 - 6.31/L^3 + 50.2/L^4$.

Once the self-consistent equations are solved, we can compute physical quantities such as the ground-state energy, excitation spectrum and gap, spin correlation function and local magnetization. In the following, we fix the energy scale by setting the value of the nearest-neighbor coupling $J_1 = 1$.

For considering the possibility of the plaquette VBC state, we also extend our formalism to include six sites in one unit cell and also introduce the previous two types of mean field order parameters(A and B). In this case, we have the following mean field order parameters:

$$\begin{aligned} A^{(p)}_{\alpha_m} &\equiv \left\langle A_{\mathbf{r}^{(1)},\mathbf{r}^{(1)}+\alpha_m}\right\rangle, \qquad & B^{(p)}_{\alpha_m} &\equiv \left\langle B_{\mathbf{r}^{(1)},\mathbf{r}^{(1)}+\alpha_m}\right\rangle, \\ A^{(n)}_{\beta_m} &\equiv \left\langle A_{\mathbf{r}^{(n)},\mathbf{r}^{(n)}+\beta_m}\right\rangle, \qquad & B^{(n)}_{\beta_m} &\equiv \left\langle B_{\mathbf{r}^{(n)},\mathbf{r}^{(n)}+\beta_m}\right\rangle \end{aligned} \tag{2.33}$$

with $n$=1,2,3,4,5,6 for different sites in one unit cell, $p$=1,2,3 for three sites which are the next nearest neighbors of each other in one unit cell, and $m$=1,2,3 for the directions of bonds. Considering the translational and rota-

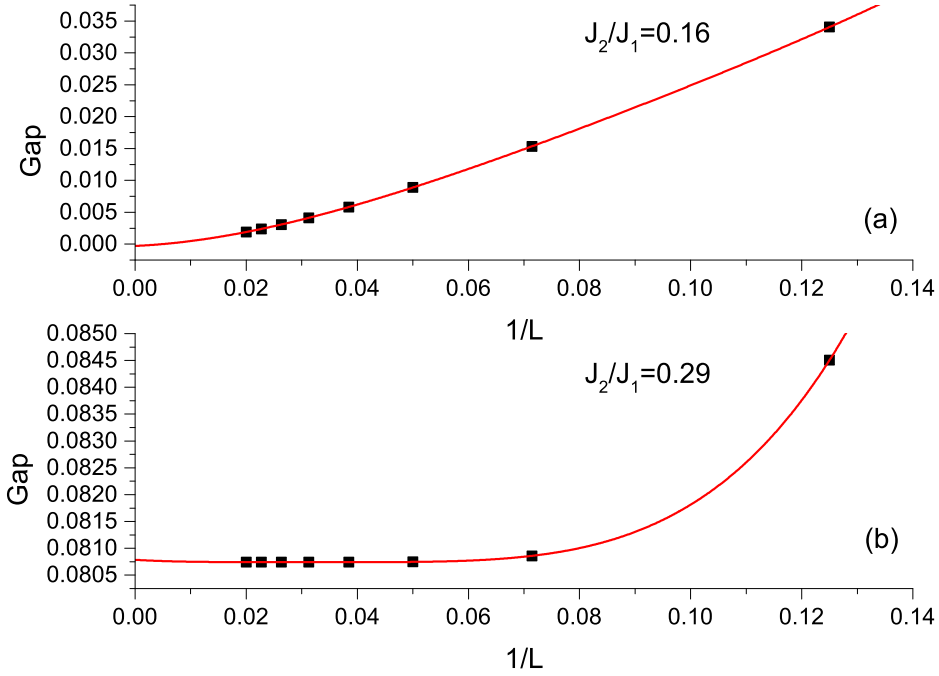


Figure 2.3: The extrapolation of the gap in the boson dispersion for (a) $J_2/J_1 = 0.16$ and (b) $J_2/J_1 = 0.29$.

tional symmetries of the plaquette VBC state, we use the following plaquette VBC ansatz for the mean field order parameters:

$$\begin{aligned}
A(B)^{(1)}_{\alpha_1} &= A(B)^{(2)}_{\alpha_2} = A(B)^{(3)}_{\alpha_3}, \\
A(B)^{(1)}_{\alpha_2} &= A(B)^{(2)}_{\alpha_3} = A(B)^{(3)}_{\alpha_1}, \\
A(B)^{(1)}_{\alpha_3} &= A(B)^{(2)}_{\alpha_1} = A(B)^{(3)}_{\alpha_2}, \\
A(B)^{(1)}_{\beta_1} &= A(B)^{(2)}_{\beta_2} = A(B)^{(3)}_{\beta_3}, \\
A(B)^{(1)}_{\beta_2} &= A(B)^{(2)}_{\beta_3} = A(B)^{(3)}_{\beta_1}, \\
A(B)^{(1)}_{\beta_3} &= A(B)^{(2)}_{\beta_1} = A(B)^{(3)}_{\beta_2}, \\
A(B)^{(4)}_{\beta_1} &= A(B)^{(5)}_{\beta_3} = A(B)^{(6)}_{\beta_2}, \\
A(B)^{(4)}_{\beta_2} &= A(B)^{(5)}_{\beta_1} = A(B)^{(6)}_{\beta_3}, \\
A(B)^{(4)}_{\beta_3} &= A(B)^{(5)}_{\beta_2} = A(B)^{(6)}_{\beta_1}.
\end{aligned} \tag{2.34}$$

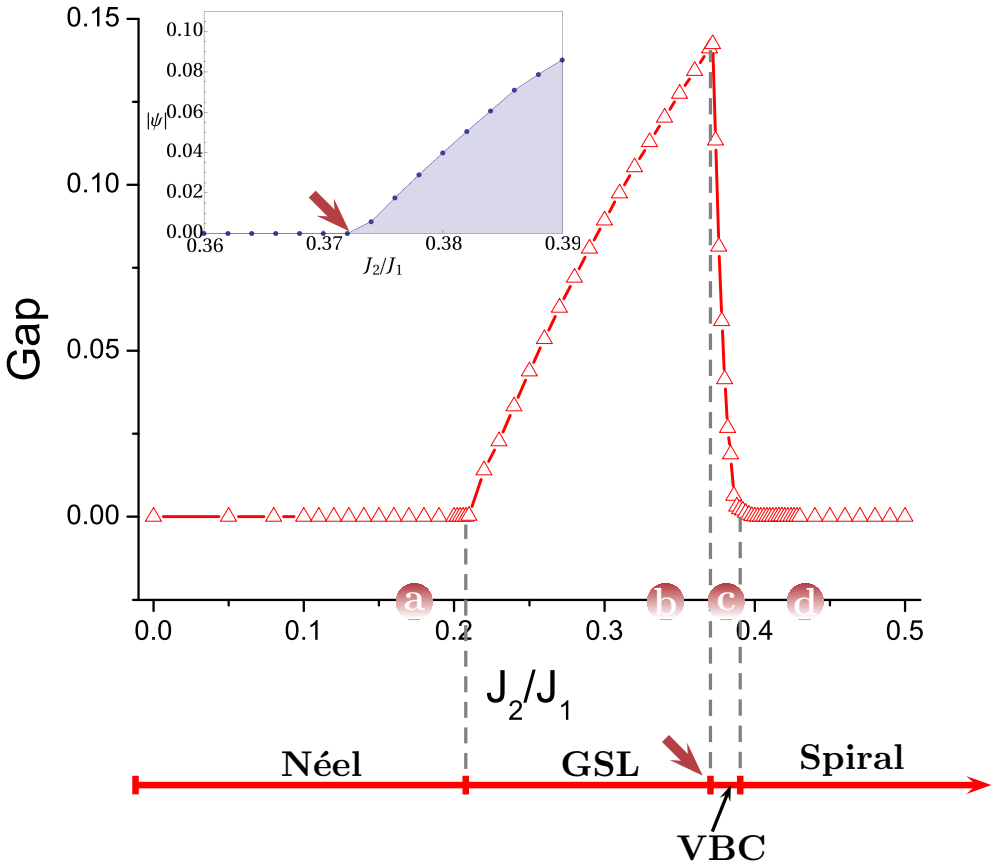


Figure 2.4: Gap in the boson dispersion extrapolated to the thermodynamic limit as a function of the frustration $J_2/J_1$ corresponding to $S = 1/2$. The gapped region corresponds to two different magnetically disordered phases: one is GSL, the other is staggered VBC. Inset: $C_3$ order parameter defined in Eq. (2.36) obtained by Schwinger boson mean-field approach extrapolated to the thermodynamic limit. The onset of the VBC phase is determined by the value of $J_2/J_1$ where $|\psi|$ is non-zero (red arrows)

## 2.3 Results

In Fig. 2.4, we show the boson dispersion relation gap extrapolated to the thermodynamic limit as a function of the frustration ($J_2/J_1$). In the gapped region, the absence of Bose condensation indicates that the ground state is magnetically disordered. This result agrees well with recent exact diagonalization [50], variational Monte Carlo [40] and coupled-cluster method [41,53] studies. In the gapless region, the excitation spectrum is zero at a given

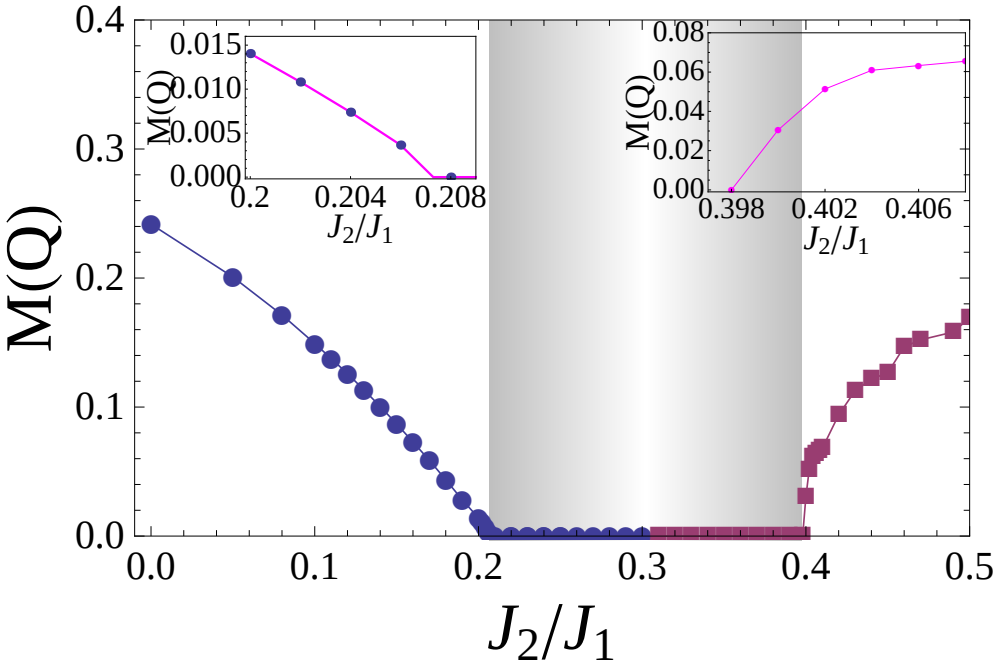


Figure 2.5: Local magnetization determined by Eq. (2.35) extrapolated to the thermodynamic limit as a function of the frustration $J_2/J_1$. The shaded region corresponds to the magnetically disordered phases. Insets correspond to the regions where the magnetization for Néel (left) and Spiral (right) phases becomes zero.

wave vector $\mathbf{k}^* = \mathbf{Q}/2$, where the Boson condensation occurs. This is characteristic of the magnetically ordered phases. The structure of these phases can be understood through the spin correlation function and the excitation spectrum. Some typical examples for different phases will be shown later.

To pin down the precise phase boundaries between the magnetically ordered and disordered phases, we introduce the local magnetization $M(\mathbf{Q})$ as an order parameter, which is obtained from the long distance behavior of the spin correlation function [97, 98]:

$$\lim_{|\mathbf{x}-\mathbf{y}|\to\infty} \left\langle \hat{\mathbf{S}}_{\mathbf{x}} \cdot \hat{\mathbf{S}}_{\mathbf{y}} \right\rangle \approx M^2(\mathbf{Q}) \cos\left[\mathbf{Q}\cdot(\mathbf{x}-\mathbf{y})\right]. \tag{2.35}$$

In Fig. 2.5, we show the local magnetization for $J_2/J_1 \in [0, 0.5]$. For $J_2/J_1 = 0$, the local magnetization is $M(\mathbf{Q})$ =0.24176, which is in excellent agreement

with the second order spin wave calculation result of 0.2418 [21]. This value is significantly reduced by quantum fluctuations compared with the classical value 0.5. The quantum Monte Carlo (QMC) result [22] is 0.2677(6), which is considerably larger than ours. For the unfrustrated case, all the mean-field approaches are quite inaccurate compared with much more controlled techniques like QMC. The difference in the $M(\mathbf{Q})$ values of about 10%, provides, in the absence of any other quantitative evidence for the accuracy of the method as applied to this model, an indication of the accuracy of the method and of all the results quoted that depend on the order parameters, including the phase boundaries. However, the mean-field approach is still very useful to study gapped phases in frustrated systems. On one hand it is well known that for frustrated systems QMC presents the famous sign problem. On the other hand, the study of quantities like energy gap requires the study of big sizes clusters and the use of exact diagonalization for small size clusters makes it very difficult to extrapolate the results.

As $J_2/J_1$ increases, the local magnetization decreases. It vanishes continuously at $J_2/J_1 \simeq 0.2075$, as shown in Fig. 2.5. [112] This value is in excellent agreement with recent numerical results, such as 0.2 by Mezzacapo *et al.* [40] using the variational Monte Carlo method with an entangled-plaquette variational ansatz, as well as $0.207 \pm 0.003$ by Bishop *et al.* [41] using the coupled-cluster method. The shift of Néel boundary compared with the classical estimate 1/6 is due to quantum fluctuations which prefer to collinear Néel rather than spiral phases in some cases. [50] In this region, the spin correlation function is antiferromagnetic in all directions, and the Boson condensation happens at the $\Gamma$ point of the first Brillouin zone: $\mathbf{k}^* = (0, 0)$, which corresponds to the ordering vector $\mathbf{Q} = (0, 0)$. As $J_2/J_1$ decreases from 0.5, the local magnetization $M(\mathbf{Q})$ decreases. It vanishes continuously at $J_2/J_1 \simeq 0.398$, as shown in Fig. 2.5. [112] This value is also in good agreement with recent numerical results, such as 0.4 by Mezzacapo *et al.* [40], as well as $0.385 \pm 0.010$ by Bishop *et al.* [41]. In this region, the spin correlation function shows different properties in different directions, however, it exhibits long-range order in all directions. The gapless points of the excitation spectrum move continuously inside the first Brillouin zone

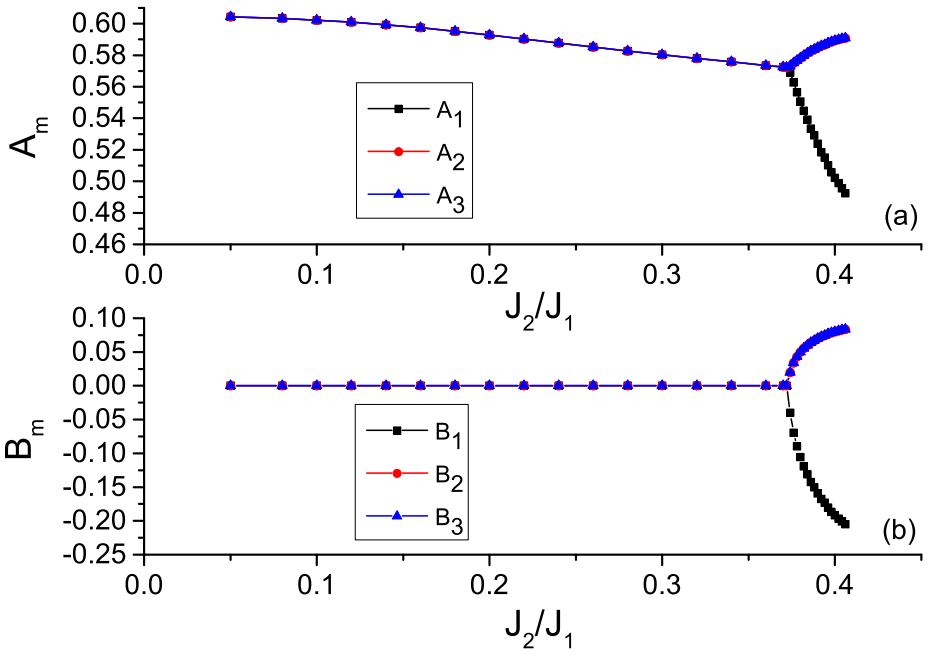


Figure 2.6: The values of (a) $A_m$ and (b) $B_m$ ($m = 1, 2, 3$) extrapolated to the thermodynamic limit as a function of the frustration $J_2/J_1$.

as $J_2/J_1$ changes. This results correspond to a spiral phase. In the classical version ($S \to \infty$) of the model (See Fig. 2.2(a)), for $J_2/J_1 > 1/6$ there remains a line-type degeneracy in which the spiral wave number is not determined uniquely and is allowed on a ring in the Brillouin zone. [42, 43] Our results suggest that the classical degeneracy is lifted in the quantum version, where some spiral wave vectors are favored by quantum fluctuations from the manifold of classically degenerate spiral wave vectors. This spiral order by disorder selection was already seen by using a spin wave approach by Mulder *et al.*, [36] and we have recovered this selection with a different approach.

The most interesting part of the phase diagram is the intermediate region which has no classical counterpart. In this region, the nonmagnetic ground state retains SU(2) spin rotational symmetry and the lattice translational symmetry, However, it may break the $C_3$ rotational symmetry of the lattice. Following Mulder *et al.* [36] we introduce the $C_3$ rotational symmetry

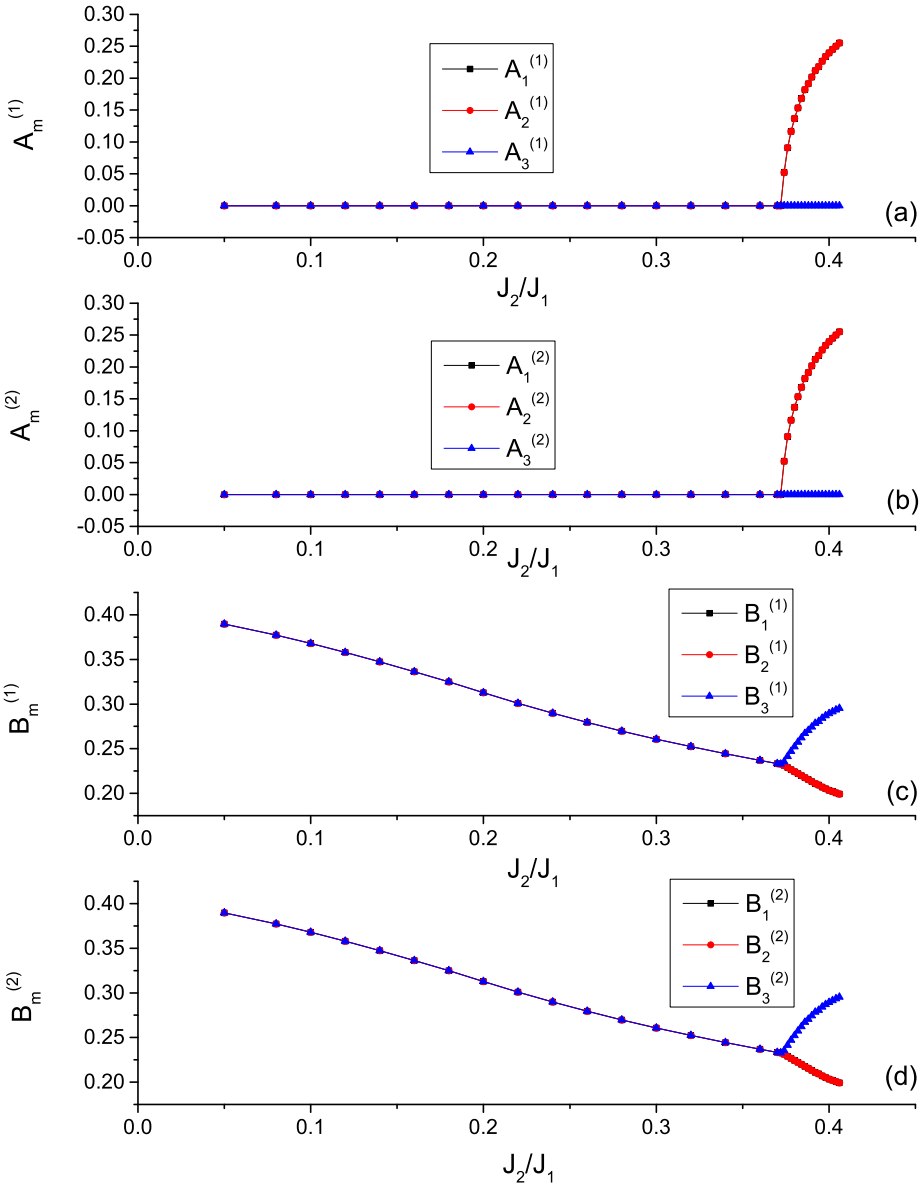


Figure 2.7: The values of (a) $A_m^{(1)}$, (b) $A_m^{(2)}$, (c) $B_m^{(1)}$, and (d) $B_m^{(2)}$ $(m = 1, 2, 3)$ extrapolated to the thermodynamic limit as a function of the frustration $J_2/J_1$.

breaking order parameter $|\psi|$ where

$$\begin{aligned}\psi &= \left\langle \hat{\mathbf{S}}_A(\mathbf{r}) \cdot \hat{\mathbf{S}}_B(\mathbf{r}) \right\rangle + \omega \left\langle \hat{\mathbf{S}}_A(\mathbf{r}) \cdot \hat{\mathbf{S}}_B(\mathbf{r}+\mathbf{e}_1) \right\rangle \\ &\quad + \omega^2 \left\langle \hat{\mathbf{S}}_A(\mathbf{r}) \cdot \hat{\mathbf{S}}_B(\mathbf{r}-\mathbf{e}_2) \right\rangle . \end{aligned} \tag{2.36}$$

Here $A$ and $B$ correspond to the two different sublattices, $\mathbf{r}$ denotes the unit cell position, and $\omega = \exp(i2\pi/3)$. Equivalently, Okumura *et al.* [34] define $\mathbf{m}_3 = \varepsilon_1\mathbf{a}_1 + \varepsilon_2\mathbf{a}_2 + \varepsilon_3\mathbf{a}_3$, where $\varepsilon_\mu$ ($\mu = 1, 2, 3$) are bond energies corresponding to the three nearest neighbor bonds $\mathbf{a}_\mu$ ($\mu = 1, 2, 3$). It is trivial to see $|\psi| = |\mathbf{m}_3|$. This order parameter is zero when the spin correlations along the three directions are equal. This is calculated by the Schwinger boson mean-field theory and we find that $|\psi|$ keeps zero when $J_2/J_1 \lesssim 0.3732$; it becomes non-zero continuously at $J_2/J_1 \simeq 0.3732$ as shown in Fig. 2.4 [112] obtained by Schwinger boson mean-field approach. Therefore, in the region $0.2075 \lesssim J_2/J_1 \lesssim 0.3732$, the ground state preserves the $C_3$ lattice rotational symmetry. The spin correlation function shows short-range antiferromagnetic correlations in all directions, and the minimum of the excitation spectrum remains pinned at the $\Gamma$ point. Namely, the system remains to be a GSL. The appearance of the GSL agrees with recent two different variational Monte Carlo studies. [39, 40] In the region $0.3732 \lesssim J_2/J_1 \lesssim 0.398$, the $C_3$ lattice rotational symmetry is broken. We find that the values of the mean fields $A$ and $B$: $A(B)_2 = A(B)_3 \neq A(B)_1$; the bond energies have the same property: $\varepsilon_2 = \varepsilon_3 \neq \varepsilon_1$. Therefore, the system should belong to the staggered VBC (lattice nematic). The existence of the staggered VBC is in agreement with a recent exact diagonalization study, [38] a bond operator mean-field study, [36] and a variational Monte Carlo study [39]. In Fig. 2.6 and Fig. 2.7 we show the values of mean-field order parameters $A(B)_m$ and $A(B)_m^{(n)}$ ($n = 1, 2; m = 1, 2, 3$) as a function of the frustration $J_2/J_1$. It is shown that $B_m$ and $A_m^{(n)}$ are zero in the Néel and GSL region, since the Néel state shows long-range antiferromagnetic correlations and the GSL state shows short-range antiferromagnetic correlations. The phase boundary of the Néel state agrees with $J_2^c \approx 0.2$ from the previous work including only $A_m$ and $B_m^{(n)}$ by Mattsson *et al.* [31], since $B_m$ and $A_m^{(n)}$ are zero in the Néel

and GSL region. All of the nearest and next-nearest neighbor mean-field parameters do not show any kink at the phase boundary of the Néel state, since the Néel and GSL phases have the same short-range behavior and show antiferromagnetic correlations, but only the Néel phase shows long-range antiferromagnetic order. The behavior of the local magnetization at this phase boundary as shown in Fig. 2.5 also supports that this phase transition is continuous. The values of $A(B)_m$ and $A(B)_m^{(n)}$ as a function of the frustration $J_2/J_1$ change continuously at the three phase transition points. This supports that the three quantum phase transitions are continuous. For the next nearest neighbor case, as it is shown in Fig. 2.7, the mean fields $A(B)_m^{(1)}$ and $A(B)_m^{(2)}$ are always the same, since the symmetry between the two sublattices is not broken.

All the values of the phase boundaries presented in this chapter correspond to mean-field estimations. In order to improve these values, it is necessary to study in detail the phase transitions beyond the mean-field level, which is out of the scope of the present thesis.

An isotropic frustrated Heisenberg model with a ground state which breaks the lattice rotational symmetry is well known from previous works, both at finite and zero temperature [115, 116]. In the square-lattice $J_1$-$J_2$ model, the broken lattice rotational symmetry survives even at finite temperature [115]. This is a lattice nematic phase which breaks the $C_4$ rotational symmetry of the square lattice.

Similarly, in the $J_1$-$J_2$ Heisenberg model on the honeycomb lattice the $C_3$ rotational symmetry about a lattice site is broken in the spiral state. This symmetry may still be broken even if spin rotational symmetry is restored by introducing quantum fluctuations. The mechanism of the stabilization of the staggered VBC state compared with the GSL state is that the frustration from the next nearest neighbor antiferromagnetic couplings ($J_2$) tends to break the $C_3$ lattice rotational symmetry. This physical mechanism exists in both of the classical and quantum cases. In the classical case, as we have explained in Chapter 1, the system exhibits Néel order for $J_2/J_1 < 1/6$. For $J_2/J_1 > 1/6$, it has a family of degenerate spiral ground states, and each state breaks the $C_3$ lattice rotational symmetry. Large value of $J_2/J_1$ is the reason

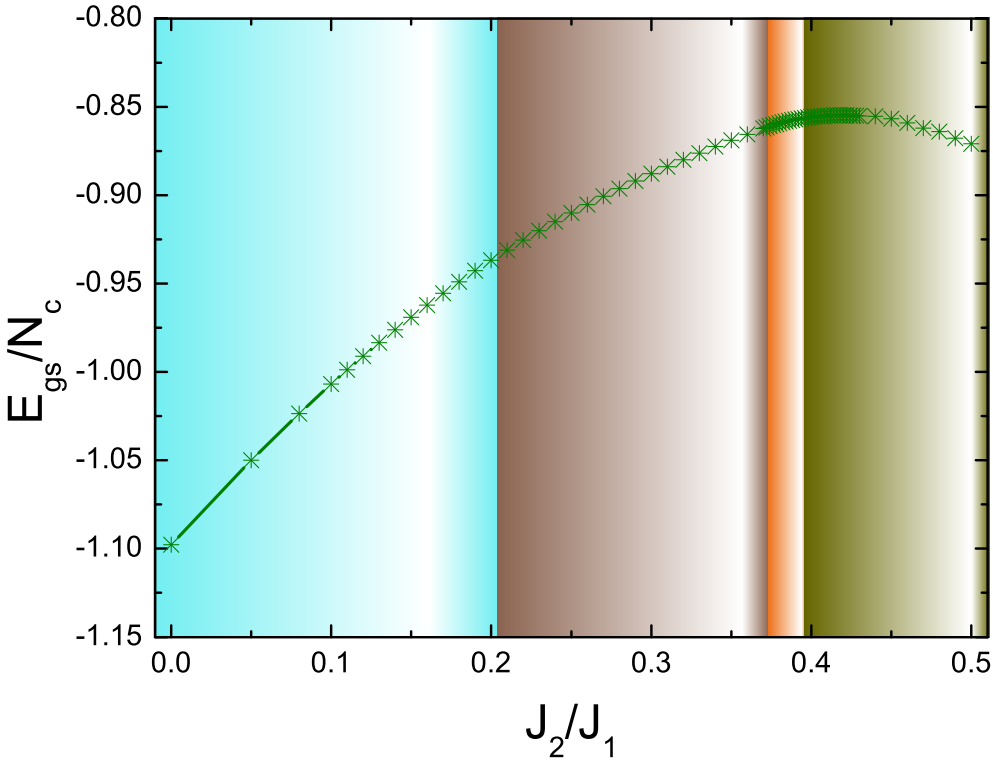


Figure 2.8: Ground-state energy per unit cell extrapolated to the thermodynamic limit as a function of the frustration $J_2/J_1$. The regions of the four different phases are indicated using the same colors that are used in Fig. 2.2.

of the $C_3$ lattice rotational symmetry breaking. The quantum fluctuations about the spiral state can lead to a lattice nematic state (staggered VBC state) which also breaks the $C_3$ lattice rotational symmetry [36, 43]. The existence of the staggered VBC state was also confirmed by using a bond operator formalism by Mulder *et al.* [36], and proposed by Fouet *et al.* [43] on the basis of exact diagonalization results.

There is substantial evidence of the existence of the staggered VBC phase, while the nature of the GSL phase is less clear. Up to now we only know few spin-1/2 models exhibiting true resonating valence bond (RVB) phases [3, 4] such as the quantum dimer model on the triangular lattice [117].

In Fig. 2.8 we show the results for the ground state energy per unit cell extrapolated to the thermodynamic limit. For the unfrustrated case ($J_2 = 0$), $E_{gs}/N_c = -1.09779$, which is in excellent agreement with the second order

spin wave calculation result of $-1.0978$ [21]. Compared with published QMC results by Reger *et al.* [118]: $-1.0890(9)$, and more recently by Löw [119]: $-1.08909(39)$, it has appreciable difference, as our previous discussion of the difference in the $M(\mathbf{Q})$ values. In the following we would like to comment on the nature of the three phase transitions. For the two transition points between the magnetic long-range order region and the magnetically disordered region, as we show in Fig. 2.4 and Fig. 2.5, the gap closing appears and the local magnetization vanishes continually at both $J_2/J_1 \simeq 0.2075$ and $J_2/J_1 \simeq 0.398$. These suggest that the two transitions are continuous. For the transition point in the magnetically disordered region, as we show in the inset of Fig. 2.4, the $C_3$ rotational symmetry breaking order parameter vanishes continually at $J_2/J_1 \simeq 0.3732$. This also suggests that the transition is continuous. Our result is also supported by the behavior of mean-field order parameters. As we show in Fig. 2.6 and Fig. 2.7, the mean-field order parameters $A(B)_m$ and $A(B)_m^{(n)}$ change continuously at the three phase transition points. It is an interesting topic for future study to investigate the nature of these quantum phase transitions by numerical methods, and more work is clearly required to study the vicinity of these transitions.

As we have shown in the introduction chapter, the plaquette VBC state has been proposed to be the ground state in the intermediate frustration region by some other approaches, such as the coupled-cluster method [41,53]. Since this state breaks the lattice translational symmetry, it cannot be treated if we only include two sites in one unit cell in our formalism. Therefore, for considering the possibility of this state, we extend our formalism to include six sites in one unit cell and also introduce the previous two types of mean fields ($A$ and $B$). The energy per site of the plaquette VBC state extrapolated to the thermodynamic limit in the intermediate frustration region is shown in Fig. 2.9. It is clear that the GSL state and the staggered VBC state are energetically favorable over the plaquette VBC state.

In the following we show several typical examples for the four different phases. The spin correlation function along zigzag and armchair directions for a system of 5000 sites is shown in Fig. 2.10 and Fig. 2.11 for $J_2/J_1 = 0.18$ (Néel), 0.36 (GSL), 0.38 (staggered VBC) and 0.48 (spiral). The correspond-

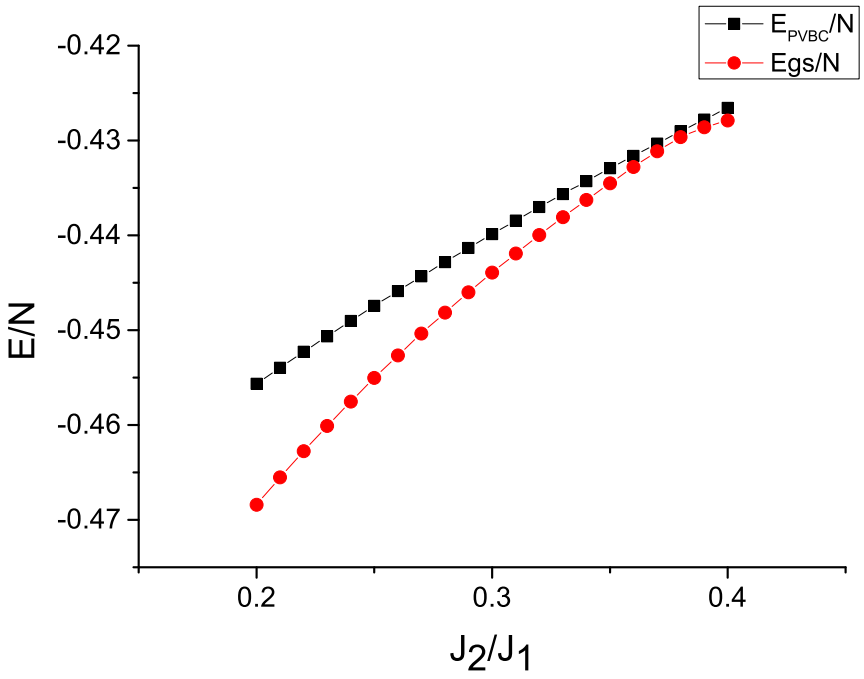


Figure 2.9: energies per site of the plaquette VBC and the ground states (GSL and staggered VBC) extrapolated to the thermodynamic limit as a function of the frustration $J_2/J_1$ in the intermediate frustration region.

ing lowest excitation spectrum is shown in Fig. 2.12. It is also shown along the line $k_x = 0$ in the first Brillouin zone in Fig. 2.13. Although it is a finite size system, we can still see differences in the four phases. For $J_2/J_1 = 0.18$, the spin correlation function in both of the zigzag and armchair directions shows long-range Néel correlations, and the lowest excitation spectrum becomes gapless at the $\Gamma$ point (for a finite size system there is a small gap which disappears after the extrapolation). For $J_2/J_1 = 0.36$, the spin correlation function in both of the zigzag and armchair directions shows only short-range antiferromagnetic correlations. The minimum of the excitation spectrum remains at the $\Gamma$ point, but a large gap there does not vanish after the $N \to \infty$ extrapolation. For $J_2/J_1 = 0.38$, the spin correlation function does not show any long-range correlation, and the short-range correlations are different between along the zigzag and armchair directions, which is an

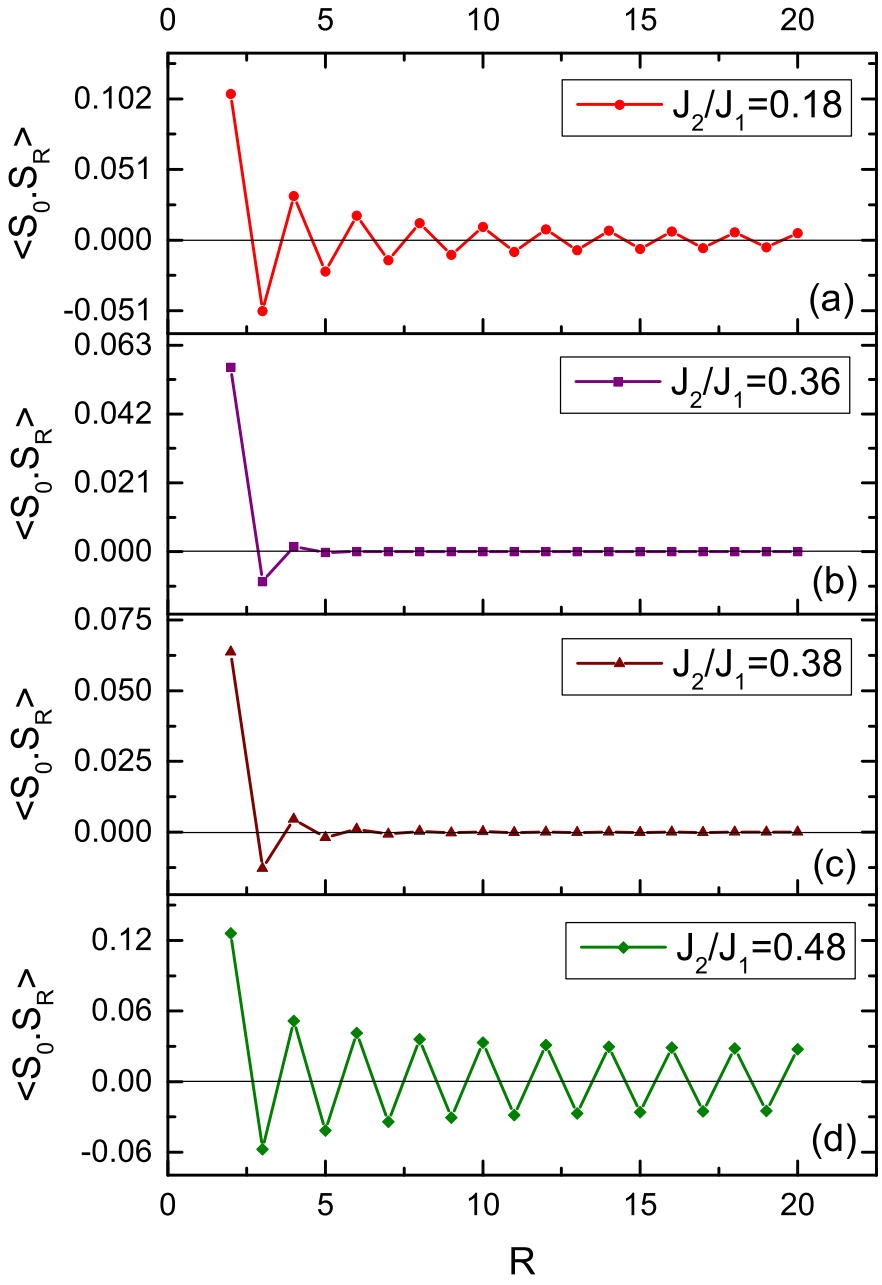


Figure 2.10: Spin correlations in the zigzag direction corresponding to the four different phases: (a)$J_2/J_1 = 0.18$ (Néel), (b)$J_2/J_1 = 0.36$ (GSL), (c)$J_2/J_1 = 0.38$ (staggered VBC), and (d)$J_2/J_1 = 0.48$ (spiral). The system size is $N = 2 \times 50 \times 50$.

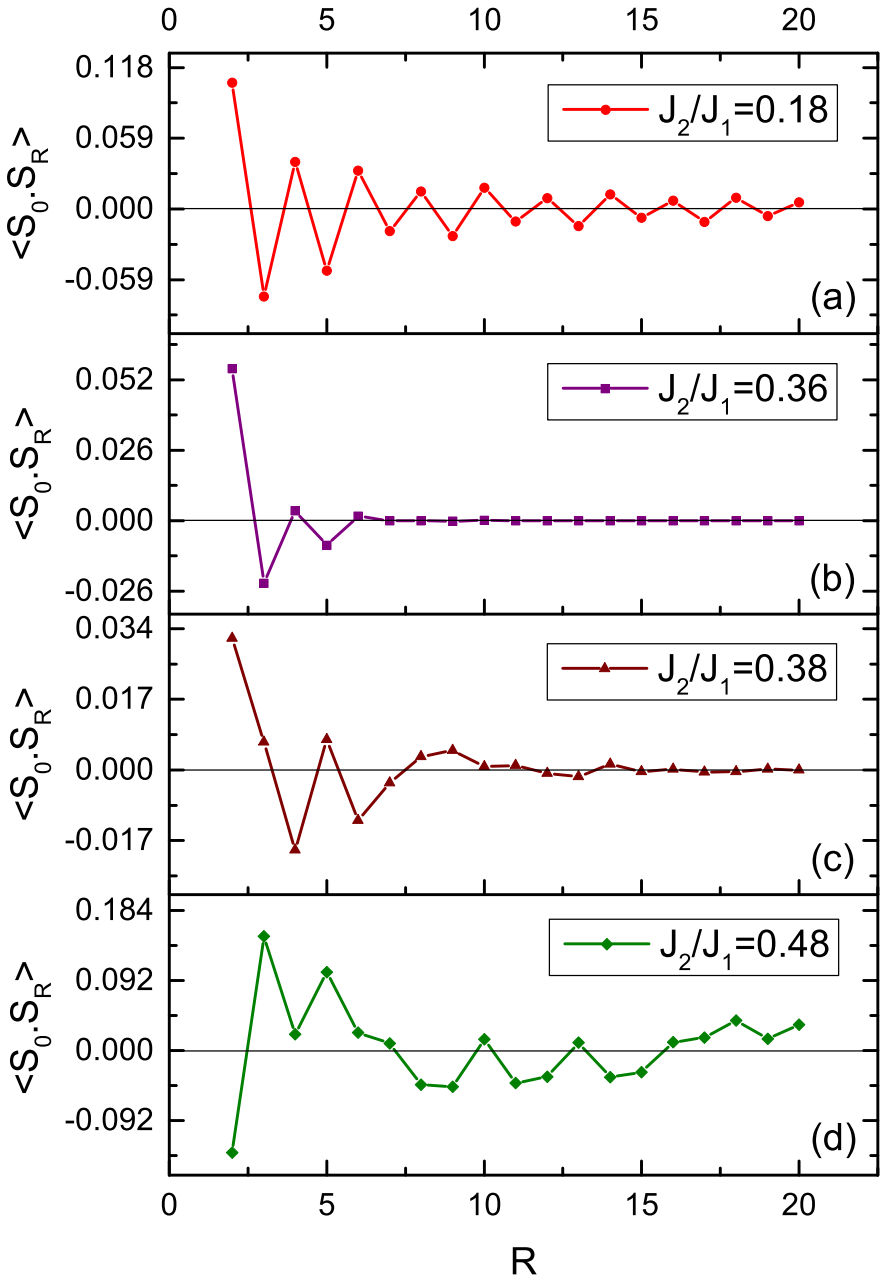


Figure 2.11: Spin correlations in the armchair direction corresponding to the four different phases: (a)$J_2/J_1 = 0.18$ (Néel), (b)$J_2/J_1 = 0.36$ (GSL), (c)$J_2/J_1 = 0.38$ (staggered VBC), and (d)$J_2/J_1 = 0.48$ (spiral). The system size is $N = 2 \times 50 \times 50$.

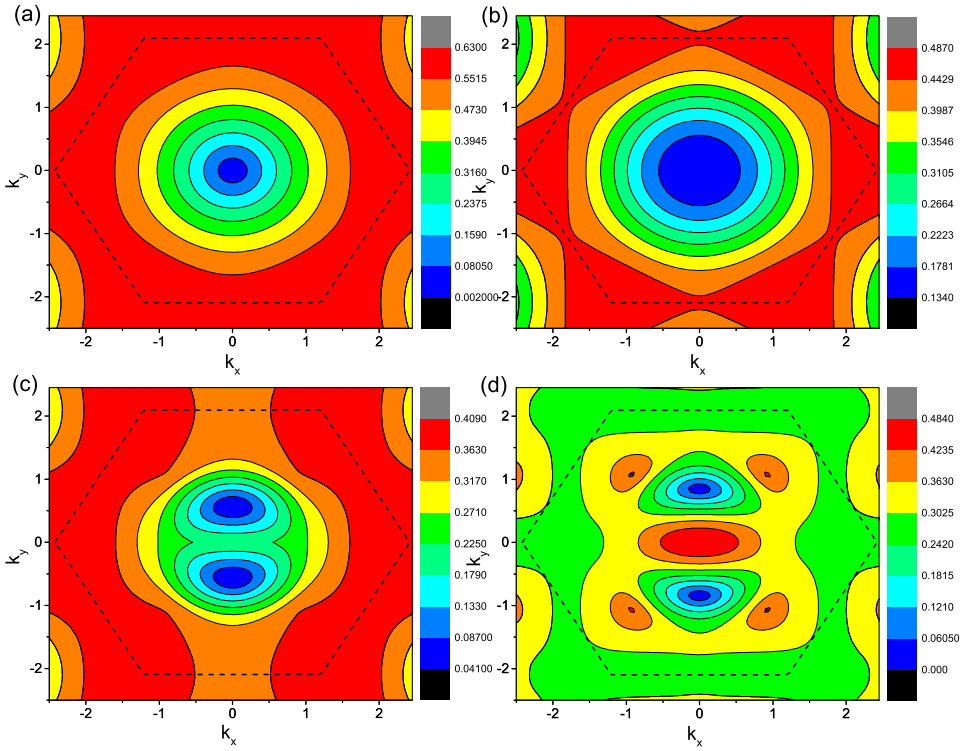


Figure 2.12: Momentum dependence of the lowest excitation spectrum for a system of size $N = 2 \times 50 \times 50$ corresponding to the four different phases: (a)$J_2/J_1 = 0.18$ (Néel), (b)$J_2/J_1 = 0.36$ (GSL), (c)$J_2/J_1 = 0.38$ (staggered VBC), and (d)$J_2/J_1 = 0.48$ (spiral). The dashed hexagon denotes the first Brillouin zone of the lattice.

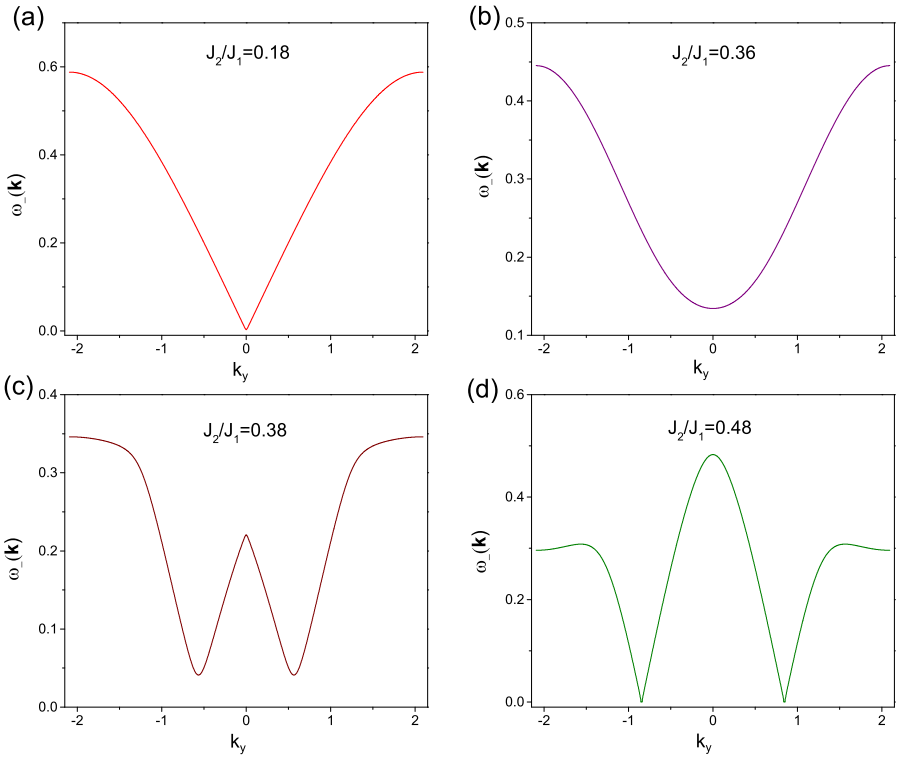


Figure 2.13: Momentum dependence of the lowest excitation spectrum along the line $k_x = 0$ in the first Brillouin zone for a system of size $N = 2 \times 50 \times 50$ corresponding to the four different phases: (a)$J_2/J_1 = 0.18$ (Néel), (b)$J_2/J_1 = 0.36$ (GSL), (c)$J_2/J_1 = 0.38$ (staggered VBC), and (d)$J_2/J_1 = 0.48$ (spiral).

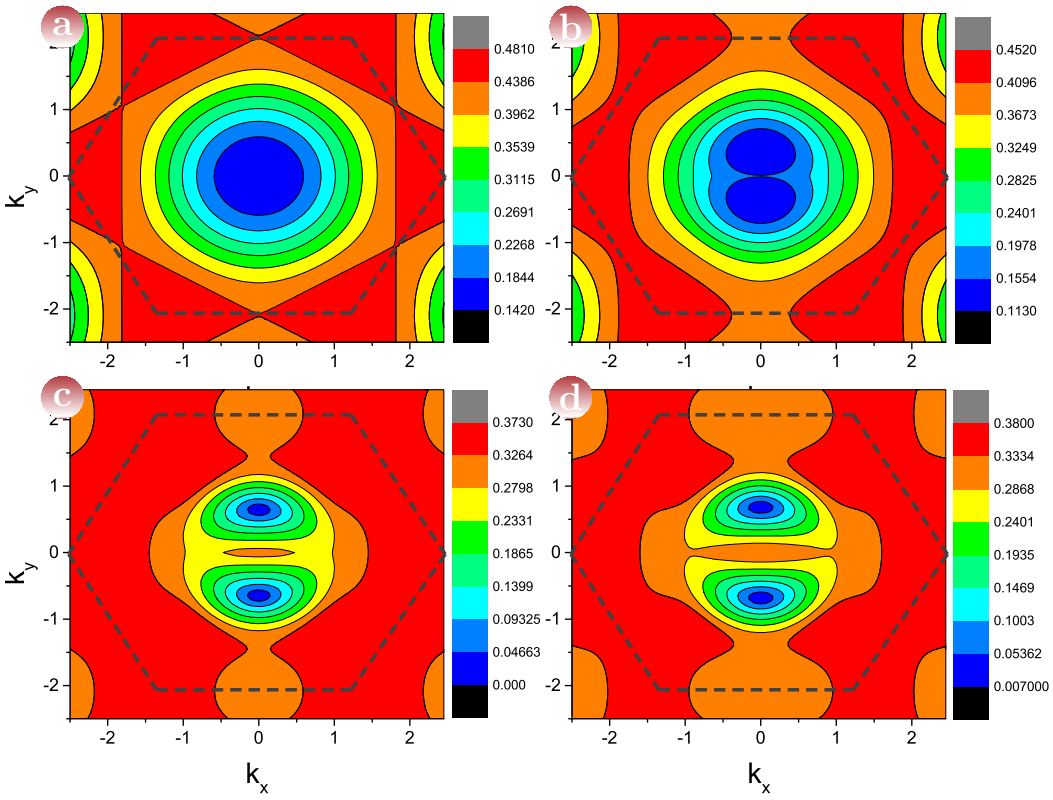


Figure 2.14: Momentum dependence of the lowest excitation spectrum for a system of size $N = 2 \times 50 \times 50$ corresponding to four points near the phase transition positions: (a)$J_2/J_1 = 0.372$ (GSL), (b)$J_2/J_1 = 0.374$ (staggered VBC), (c)$J_2/J_1 = 0.392$ (staggered VBC), and (d)$J_2/J_1 = 0.402$ (spiral). The dashed hexagon denotes the first Brillouin zone of the lattice.

indication that the lattice rotational symmetry is broken. Simultaneously, the minimum of the lowest excitation spectrum is away from the Γ point and the lattice rotational symmetry is clearly broken. There is also a gap in this region which remains finite in the thermodynamic limit. For $J_2/J_1 = 0.48$, the spin correlation function shows magnetic long-range correlations in both directions. Since one component of the ordering vector $Q_x = 0$ (corresponding to $k_x^* = 0$ in the lowest excitation spectrum), the spin correlation function is Néel-like along the zigzag directions. This result agrees well with the spin wave calculations by Mulder *et al.* [36]. In Fig. 2.14, we show the lowest excitation spectrum for the same system size for $J_2/J_1 = 0.372$ (GSL), 0.374 (staggered VBC), 0.392 (staggered VBC) and 0.402 (spiral). The former two values are near the second transition point in Fig. 2.2 b), while the latter two are near the third transition point. After the phase transition from the GSL phase to the staggered VBC phase, the number of the minimum points of the lowest excitation spectrum becomes two, and these two points move away from the Γ point. This behavior provides the evidence that the lattice rotational symmetry is broken in the staggered VBC phase. The behavior of the lowest excitation spectrum also supports that these phase transitions are continuous.

In the following, we would like to comment on the nature of the GSL phase. Wang [37] applied the projective symmetry group method [120, 121] to classify possible GSLs within the Schwinger boson mean field formalism on the honeycomb lattice. Our GSL phase may correspond to the zero-flux $Z_2$ spin liquid proposed by Wang [37]. However, as we have reviewed in Chapter 1, the author only included antiferromagnetic correlations for both nearest and next-nearest neighbors and did not determine the phase diagram with respect to $J_2/J_1$. Generally speaking, both of ferromagnetic and antiferromagnetic correlations should be taken into account for frustrated models [100]. Another point is that the author assumed that the bond mean fields are independent of the directions of bonds. Therefore, this scheme can not describe the phases which break the lattice rotational symmetry. Since the unit cell contains two cites on the honeycomb lattice, the Hastings generalization [122] of the Lieb-Schultz-Mattis theorem [123] does not apply and

it is possible to have a GSL without a topological order [8]. The affirmative answer was finally given by Kimchi *et al.* [124]. It would be very interesting to study such phase in the $J_1$-$J_2$ model on the honeycomb lattice.

Finally, we would like to comment on the future step of our work. We have used a mean-field approach based on the Schwinger boson representation of the spin operators. This mean-field approach has the drawback that unphysical configurations are allowed since the constraint about the bosonic space is treated only as an average restriction. This drawback can be partially corrected by including local fluctuations of the bosonic chemical potential [125]. This correction was calculated by Trumper *et al.* [99] for the $J_1$-$J_2$ square lattice using collective coordinate methods, and a comparison between the mean field results and the corrected results was made. However, this hard calculation allows only to calculate some special quantities like the ground state energy and spin stiffness. The corrections developed by Trumper *et al.* could be extended to spiral phases [126], and would allow us to investigate the present model.

## 2.4 Summary and discussions

### 2.4.1 Summary

In the present chapter, we have investigated the quantum $J_1$-$J_2$ Heisenberg model on the honeycomb lattice within a rotationally invariant version of the Schwinger boson mean-field theory. In the region $0 \leq J_2/J_1 \leq 0.5$, the quantum phase diagram of the model has four different regions [112]. The magnetic long-range order of Néel and spiral types is found for $J_2/J_1 \lesssim 0.2075$ and $J_2/J_1 \gtrsim 0.398$, respectively. For the spiral region, the spiral order is stabilized by quantum fluctuations, which agrees with Mulder *et al.* [36] using spin wave theory. In the intermediate region, the energy gap is finite while the local magnetization is zero, which indicates the presence of a magnetically disordered ground state. We have used the $C_3$ rotational symmetry breaking order parameter $|\psi|$ defined in Eq. (2.36) and classified this part into two different magnetically disordered phases. One is a GSL

which shows short-range Néel correlations ($0.2075 \lesssim J_2/J_1 \lesssim 0.3732$), and the other is staggered VBC (lattice nematic), which breaks the $C_3$ rotational symmetry ($0.3732 \lesssim J_2/J_1 \lesssim 0.398$). Considering the properties of order parameters, these three quantum phase transitions are continuous.

### 2.4.2 Discussions and comparison with other previous theoretical works

As we have mentioned above, recent theoretical studies of the phase diagram of the spin-1/2 $J_1$-$J_2$ Heisenberg model on the honeycomb lattice have reported conflicting results. The central controversial point is the existence and nature of magnetically disordered phases when the Néel order becomes unstable with increasing the frustration $J_2/J_1$. There is a growing consensus [36, 38–41, 43, 50, 51, 53] that a magnetically disordered region should appear. However, the nature of this region is still not clear, since different approaches have given different results. An early exact diagonalization work by Fouet *et al.* [43] first claimed that a GSL might appear in the region $J_2/J_1 \approx 0.3 - 0.35$, and for $J_2/J_1 \approx 0.4$ the system might be the staggered VBC. A recent exact diagonalization study by Mosadeq *et al.* [38] claimed that a plaquette VBC might exist in the region $0.2 < J_2/J_1 < 0.3$, and a phase transition from plaquette VBC to the staggered VBC exists at a point in the region $0.35 \leq J_2/J_1 \leq 0.4$. However, a more recent exact diagonalization work by Albuquerque *et al.* [50], which treated larger system sizes, was unable to determine whether this magnetically disordered region is a plaquette VBC with a small order parameter or a GSL. It is possible that the plaquette VBC correlation may just be due to finite size effects [40]. For larger $J_2/J_1$, it is also hard to distinguish the staggered VBC from spiral phases, since exact diagonalization is especially difficult to examine an incommensurate behavior of spin correlations due to limited lattice sizes.

There are two recent studies of this model using variational Monte Carlo methods with different trial wave functions. Clark *et al.* [39] used Huse-Elser states and resonating valence bond (RVB) states, and claimed that a GSL appears in the region $0.08 \leq J_2/J_1 \leq 0.3$, and it is replaced by a

dimerized state which breaks lattice rotational symmetry for $J_2/J_1 \gtrsim 0.3$. A more recent work by Mezzacapo *et al.* [40] using an entangled-plaquette variational ansatz obtained lower energy estimates, and claimed that in the magnetically disordered region $0.2 \lesssim J_2/J_1 \lesssim 0.4$, the plaquette VBC order parameter vanishes in the thermodynamic limit. They claimed that the plaquette VBC obtained by exact diagonalization studies [38, 50] may just come from the finite size effects. Since the $C_3$ rotational symmetry breaking order parameter was not considered in Ref. [40], it is still not clear that the lattice rotational symmetry is broken or not in the region $0.2 \lesssim J_2/J_1 \lesssim 0.4$ from their study. Our result of the magnetically disordered region shows excellent agreement with Ref. [40]. However, we calculate the $C_3$ rotational symmetry breaking order parameter, and show that a GSL phase and a staggered VBC phase exist in this region. The latter phase breaks the $C_3$ lattice rotational symmetry.

In a recent study using the pseudofermion functional renormalization group method [51], Reuther *et al.* claimed that within the magnetically disordered region for larger $J_2/J_1$, there is a strong tendency for the staggered VBC ordering, and that for small $J_2/J_1$, both of plaquette and staggered VBC responses are very weak. A further recent study using the coupled-cluster method [41] reported more quantitatively about magnetically disordered state and the region of $0.207 \pm 0.003 < J_2/J_1 < 0.385 \pm 0.010$ is the plaquette VBC phase. However, the ground state for $0.21 \lesssim J_2/J_1 \lesssim 0.24$ is hard to identify using this approach.

Another controversial point is the form of the magnetic long-range order when $J_2/J_1$ exceeds the boundary of the magnetically disordered region. There are two proposals: the anti-Néel order [40, 41] or the spiral order [45, 51]. It is difficult to conclude by exact diagonalization since it is hard to examine incommensurate spin correlations due to limited lattice sizes [50]. Both of the recent series expansion [45] and the pseudofermion functional renormalization group [51] studies did not find any evidence for the existence of the anti-Néel order and concluded that the spiral state should be the stable ground state. However, both of the variational Monte Carlo with the entangled-plaquette variational ansatz [40] and the coupled-cluster

method [41] studies support the anti-Néel order. We are interested in the exotic disordered phases in the magnetically disordered region and focus on the region of $0 \leq J_2/J_1 \leq 0.5$, and we obtain the spiral order in the region $0.398 \lesssim J_2/J_1 \leq 0.5$. We do not examine the possibility that the anti-Néel order state exists for $J_2/J_1 > 0.5$.

Recently, the density matrix renormalization group (DMRG) [127–129] study was performed to the spin-1/2 Kagome Heisenberg model [130, 131] and the square $J_1$-$J_2$ Heisenberg model [132], and reported GSLs as the ground state. Since quantum fluctuations are expected to be stronger in the honeycomb lattice than in the square lattice, it would be very interesting to apply DMRG to the spin-1/2 $J_1$-$J_2$ Heisenberg model on the honeycomb lattice.

### 2.4.3 Implication for understanding experimental results

Finally, we briefly discuss possible experimental realization of the physics discussed in this chapter. The bismuth manganese oxynitrate $Bi_3Mn_4O_{12}(NO_3)$ studied by Smirnova *et al.* [11] appears to be an example of honeycomb lattice quantum antiferromagnets. In this compound the $Mn^{4+}$ ions form $S = 3/2$ honeycomb lattice without any distortion. The estimated values of $J_1$ and $J_2$ by neutron scattering experiments [13, 14] are $J_1 = 1.4$ meV and $J_2 = 0.2$ meV. Here $J_2/J_1$ is smaller than our theoretical result of the Néel phase boundary $(J_2/J_1)_c \simeq 0.2075$ for $S = 1/2$ case. As we have shown in Sec. 2.3, our result of the Néel phase boundary agrees well with recent numerical simulation results [40, 41, 50, 53], and larger than the classical result 1/6. Albuquerque *et al.* [50] discussed this shift of the Néel phase boundary and claimed that in some cases quantum fluctuations prefer collinear over spiral states, such as in the $J_1$-$J_3$ model on the square lattice [133–135] and in the $J_1$-$J_2$ model on the honeycomb lattice [50]. On the other hand, strong quantum fluctuations may suppress the magnetic long-range order. There is competition between these two physical mechanisms for the stability of the Néel phase. Therefore, it is possible that $S = 3/2$ case has smaller $(J_2/J_1)_c$

than $S = 1/2$ case. Since $Bi_3Mn_4O_{12}(NO_3)$ shows short-range antiferromagnetic correlations at low temperatures [13, 14], as we have observed in the GSL state, we expect that the ground state of this compound may be the GSL state, which also shows short-range antiferromagnetic correlations. The successful substitutions of $Mn^{4+}(S = 3/2)$ in $Bi_3Mn_4O_{12}(NO_3)$ by $V^{4+}$ could lead to the realization of $S = 1/2$ Heisenberg model on the honeycomb lattice [11]. This material is a possible candidate for observing the magnetically disordered phases discussed in this chapter.

## 2.5 Theoretical results after our publication

After our publication [55] of the main results of Chapter 2, there have appeared several studies on the ground-state phase diagram of the spin-1/2 honeycomb $J_1$-$J_2$ Heisenberg model by different approaches, including DMRG [56–58] and coupled-cluster method [59]. Ganesh *et al.* [56] used a two dimensional DMRG which treats clusters with geometries properly chosen for various ordering patterns. It was found that as the frustration increases, the Néel order vanishes at $J_2/J_1 \simeq 0.22$, and is replaced by a plaquette VBC phase for $0.22 \lesssim J_2/J_1 \lesssim 0.35$, and a staggered VBC phase exists for $J_2/J_1 \gtrsim 0.35$. The Néel and plaquette VBC order parameters vanish continuously at the same transition point $J_2/J_1 \simeq 0.22$, and the plaquette VBC and staggered VBC order parameters vanish continuously at the other transition point $J_2/J_1 \simeq 0.35$. Thus they claimed that these two transitions belong to the deconfined quantum criticality [136, 137]. Independently, Zhu *et al.* [57] used various cylindrical boundary conditions with open ends in their DMRG calculations, and found that the Néel order vanishes at $J_2/J_1 \simeq 0.26$, and a magnetically disordered phase exists for $0.26 \lesssim J_2/J_1 \lesssim 0.36$. The correlation length of plaquette valence bond order grows strongly with cylinder circumference, suggesting the system is either at quantum criticality or has a weak plaquette valence bond order. For $J_2/J_1 \gtrsim 0.36$, it was suggested that a staggered VBC phase exists.

Gong *et al.* [58] used another version of DMRG implemented with spin rotational SU(2) symmetry. Therefore, they can treat larger system sizes

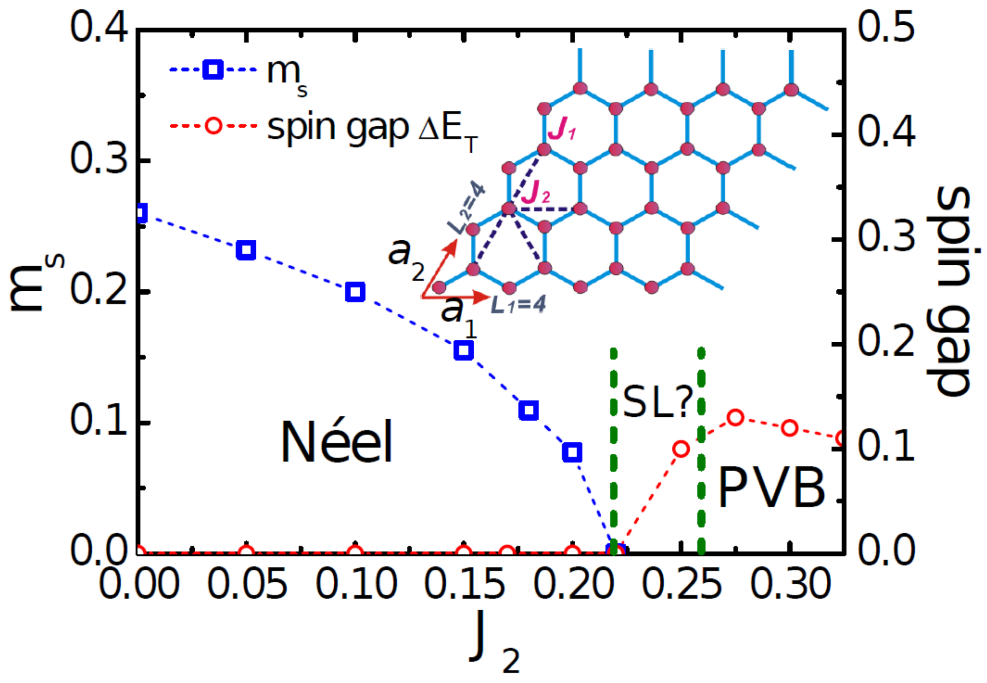


Figure 2.15: Phase diagram of the $J_1$-$J_2$ honeycomb Heisenberg model for $J_2 \leq 0.35$ obtained by SU(2) DMRG studies ($J_1 \equiv 1$). With increasing $J_2$, the model has a Néel phase for $J_2 \lesssim 0.22$ and a plaquette VBC phase for $0.25 \lesssim J_2 \lesssim 0.35$. Between these two phases, there is a small region that exhibits no order in the calculations. The main panel shows local magnetization $m_s$ and spin gap $\Delta E_T$. The inset is the sketch of the $J_1$-$J_2$ honeycomb lattice on a $N = 2 \times L_1 \times L_2$ torus (here with four unit cells, $L_1 = L_2 = 4$, along the two primitive vector directions). (from Ref. [58])

with high accuracy. They studied the model on both a torus and a cylinder, and obtained the results which are summarized in Fig. 2.15. It was shown that the Néel order vanishes at $J_2/J_1 \simeq 0.22$ and a plaquette VBC phase exists for $0.25 \lesssim J_2/J_1 \lesssim 0.35$. For $0.22 < J_2/J_1 < 0.25$, both spin and dimer orders vanish in the thermodynamic limit, which corresponds to a gapped spin liquid. The variational Monte Carlo results also support the existence of a gapped spin liquid in this region.

Bishop *et al.* [59] used the coupled-cluster method to study a larger region of $J_2/J_1$. Their results are summarized in Fig 2.16. The Néel order vanishes at $J_2/J_1 \simeq 0.207(3)$, and is replaced by a plaquette VBC phase

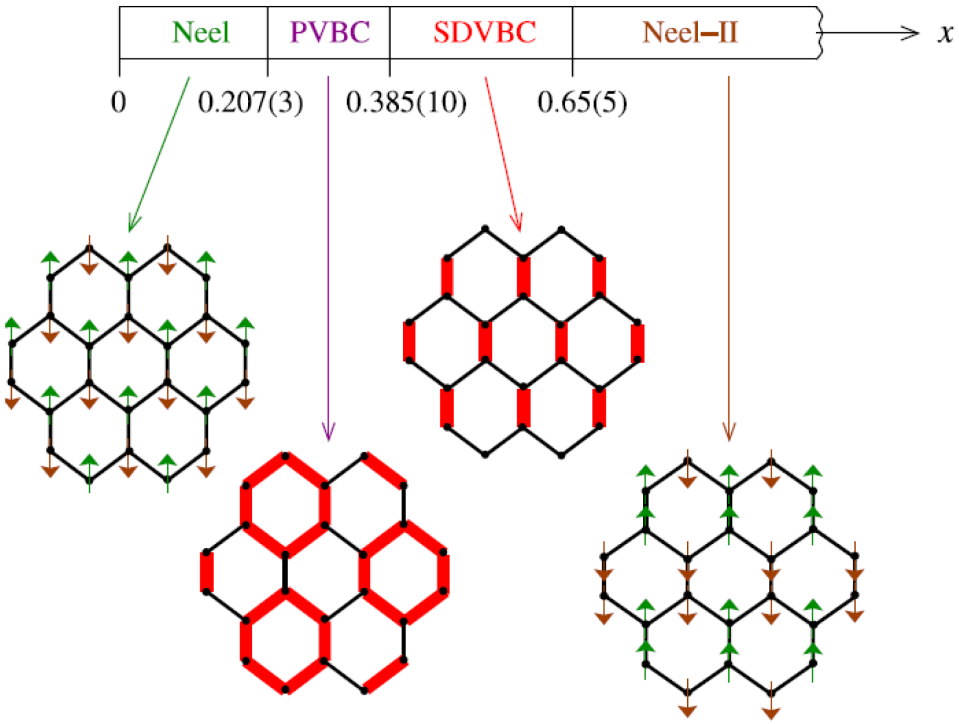


Figure 2.16: Phase diagram of the $S = 1/2$ $J_1$-$J_2$ honeycomb Heisenberg model (with $J_1 > 0$ and $x \equiv J_2/J_1 > 0$) determined by a coupled-cluster method analysis. The quantum critical points are at $x_{c_1} \approx 0.207(3)$, $x_{c_2} \approx 0.385(10)$, and $x_{c_3} \approx 0.65(5)$, as shown in the diagram. (from Ref. [59])

for $0.207(3) \lesssim J_2/J_1 \lesssim 0.385(10)$, and a staggered VBC phase exists for $0.385(10) \lesssim J_2/J_1 \lesssim 0.65(5)$. For $J_2/J_1 \gtrsim 0.65(5)$, the ground state is Néel-II state (also called anti-Néel state in Ref. [41]). The coupled-cluster method calculation needs a suitable reference state as a starting point, and the Néel state is chosen for small value of $J_2/J_1$, while Néel-II state for large value of $J_2/J_1$. Therefore, actually their results can not rule out the possibility of the spiral order for $J_2/J_1 < 0.5$. Since the upper boundary of the staggered VBC phase was determined by vanishing Néel-II order, this phase boundary is likely to change if the spiral order is treated carefully in the coupled-cluster method.

Table. 2.1 summarizes theoretical results of the magnetically disordered region after our publication. All of these studies agrees well with our results

| Method | Magnetically disordered region |
|---|---|
| DMRG [56] | $0.22 \lesssim J_2/J_1 \lesssim 0.35$ (PVBC), |
| | $J_2/J_1 \gtrsim 0.35$ (SVBC) |
| DMRG [57] | $0.26 \lesssim J_2/J_1 \lesssim 0.36$ (weak PVBC), |
| | $J_2/J_1 \gtrsim 0.36$ (SVBC) |
| DMRG [58] | $0.22 < J_2/J_1 < 0.25$ (GSL), |
| | $0.25 \lesssim J_2/J_1 \lesssim 0.35$ (PVBC) |
| CCM [59] | $0.207(3) \lesssim J_2/J_1 \lesssim 0.385(10)$ (PVBC), |
| | $0.385(10) \lesssim J_2/J_1 \lesssim 0.65(5)$ (SVBC) |

Table 2.1: Theoretical results of the magnetically disordered region in the quantum $J_1$-$J_2$ Heisenberg model on the single layer honeycomb lattice after our publication.

for the melting of the Néel order and the appearance of the magnetically disordered phases in the intermediate region of the frustration. Ganesh *et al.* [56], Zhu *et al.* [57] and Bishop *et al.* [59] have suggested the existence of the staggered VBC phase. The existence of gapped spin liquid claimed by Gong *et al.* [58] also agrees with our results. The appearance of the plaquette VBC phase is not consistent with our results.

# Chapter 3

# Melting of Néel order and magnetically disordered phases in the $J_1$-$J_2$ Heisenberg model on the bilayer honeycomb lattice

This chapter presents our study of $S = 1/2$ frustrated Heisenberg antiferromagnetic model on the bilayer honeycomb lattice. In Sec. 3.1 we introduce our model. In Sec. 3.2 we describe the Schwinger boson mean-field formalism specialized for this model. In Sec. 3.3 we apply the Schwinger boson mean-field approach for $S = 1/2$ case, complemented with exact diagonalization calculation. In Sec. 3.4 we apply the linear spin wave theory for general spin $S$. We close with a conclusion and discussion in Sec. 3.5.

## 3.1 Bilayer model

The $J_1 - J_2 - J_\perp$ Heisenberg model on the bilayer honeycomb lattice is given by

$$\hat{H} = J_1 \sum_{\langle i,j\rangle_1,l} \hat{\mathbf{S}}_i^l \cdot \hat{\mathbf{S}}_j^l + J_2 \sum_{\langle i,j\rangle_2,l} \hat{\mathbf{S}}_i^l \cdot \hat{\mathbf{S}}_j^l + J_\perp \sum_i \hat{\mathbf{S}}_i^1 \cdot \hat{\mathbf{S}}_i^2. \tag{3.1}$$

Here $l = 1, 2$ denotes the spins in the two layers. $\langle i, j\rangle_n$ indicates sum over the $n$-th neighbors, and the second sum runs over the neighboring spins between the two layers (see Fig. 3.1).

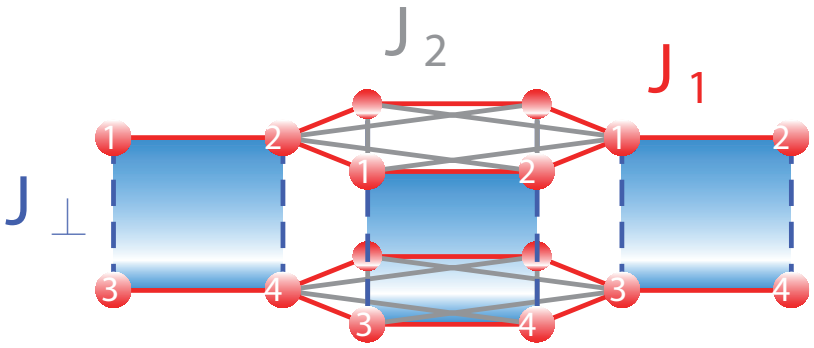


Figure 3.1: The honeycomb lattice with $J_1$, $J_2$ and $J_\perp$ couplings considered in this chapter. Colored areas correspond to the unit cells. The sites in each unit cell are labeled from 1 to 4.

## 3.2 Schwinger boson mean-field approach for the bilayer model

Now we present the formulation of Schwinger boson mean-field approach which we will use in this chapter. We represent the spin operators at each lattice site by two types of Schwinger bosons with a local constraint of the number of Schwinger bosons per site to fix the magnitude of the spin, and introduce two types of bond operators as we have done in chapter 2. In the following, $\hat{A}^l_{\mathbf{R},\mathbf{R}+\delta}$ and $\hat{B}^l_{\mathbf{R},\mathbf{R}+\delta}$ correspond to two types of bond operators within the two layers. $\hat{A}^\perp_{\mathbf{R},\mathbf{R}} = \frac{1}{2}\left(\hat{b}^1_{\mathbf{R}\uparrow}\hat{b}^2_{\mathbf{R}\downarrow} - \hat{b}^1_{\mathbf{R}\downarrow}\hat{b}^2_{\mathbf{R}\uparrow}\right)$ and $\hat{B}^\perp_{\mathbf{R},\mathbf{R}} = \frac{1}{2}\left(\hat{b}^{1\dagger}_{\mathbf{R}\uparrow}\hat{b}^2_{\mathbf{R}\uparrow} + \hat{b}^{1\dagger}_{\mathbf{R}\downarrow}\hat{b}^2_{\mathbf{R}\downarrow}\right)$

correspond to two types of bond operators for the neighboring spins between the two layers. Therefore, we can decompose the Hamiltonian as

$$\begin{aligned}\hat{H} &= J_1 \sum_{\mathbf{r}^{(1)},lm} \left( :\hat{B}^{l\dagger}_{\mathbf{r}^{(1)},\mathbf{r}^{(1)}+\alpha_m} \hat{B}^{l}_{\mathbf{r}^{(1)},\mathbf{r}^{(1)}+\alpha_m}: -\hat{A}^{l\dagger}_{\mathbf{r}^{(1)},\mathbf{r}^{(1)}+\alpha_m} \hat{A}^{l}_{\mathbf{r}^{(1)},\mathbf{r}^{(1)}+\alpha_m} \right) \\ &+J_2 \sum_{n} \sum_{\mathbf{r}^{(n)},lm} \left( :\hat{B}^{l\dagger}_{\mathbf{r}^{(n)},\mathbf{r}^{(n)}+\beta_m} \hat{B}^{l}_{\mathbf{r}^{(n)},\mathbf{r}^{(n)}+\beta_m}: -\hat{A}^{l\dagger}_{\mathbf{r}^{(n)},\mathbf{r}^{(n)}+\beta_m} \hat{A}^{l}_{\mathbf{r}^{(n)},\mathbf{r}^{(n)}+\beta_m} \right) \\ &+J_\perp \sum_{n} \sum_{\mathbf{r}^{(n)}} \left( :\hat{B}^{\perp\dagger}_{\mathbf{r}^{(n)},\mathbf{r}^{(n)}} \hat{B}^{\perp}_{\mathbf{r}^{(n)},\mathbf{r}^{(n)}}: -\hat{A}^{\perp\dagger}_{\mathbf{r}^{(n)},\mathbf{r}^{(n)}} \hat{A}^{\perp}_{\mathbf{r}^{(n)},\mathbf{r}^{(n)}} \right). \end{aligned} \tag{3.2}$$

Here $\mathbf{r}^{(n)}$ are the positions of lattice sites of sublattice $n$ ($n = 1, 2$). $\alpha_m$ are the nearest neighbor vectors and $\beta_m$ are three of the next nearest neighbor vectors as we have chosen in Chapter 2, with $m = 1, 2, 3$ for the directions of bonds. Then we introduce mean fields corresponding to these bond operators. We assume that they are uniform in space, but dependent on the directions of bonds:

$$\begin{aligned} A^{l}_{m} &\equiv \left\langle \hat{A}^{l}_{\mathbf{r}^{(1)},\mathbf{r}^{(1)}+\alpha_m} \right\rangle, & B^{l}_{m} &\equiv \left\langle \hat{B}^{l}_{\mathbf{r}^{(1)},\mathbf{r}^{(1)}+\alpha_m} \right\rangle, \\ A^{l(n)}_{m} &\equiv \left\langle \hat{A}^{l}_{\mathbf{r}^{(n)},\mathbf{r}^{(n)}+\beta_m} \right\rangle, & B^{l(n)}_{m} &\equiv \left\langle \hat{B}^{l}_{\mathbf{r}^{(n)},\mathbf{r}^{(n)}+\beta_m} \right\rangle, \\ A^{\perp(n)} &\equiv \left\langle \hat{A}^{\perp}_{\mathbf{r}^{(n)},\mathbf{r}^{(n)}} \right\rangle, & B^{\perp(n)} &\equiv \left\langle \hat{B}^{\perp}_{\mathbf{r}^{(n)},\mathbf{r}^{(n)}} \right\rangle. \end{aligned} \tag{3.3}$$

with $l$=1,2 for different layers, $n$=1,2 for different sublattices and $m$=1,2,3 for the directions of bonds.

By using the Hartree-Fock decoupling, we obtain the mean-field Hamiltonian:

$$\begin{aligned}\hat{H}_{MF} &= J_1 \sum_{\mathbf{r}^{(1)},lm} \Big[ \left( B^{l*}_{m} \hat{B}^{l}_{\mathbf{r}^{(1)},\mathbf{r}^{(1)}+\alpha_m} - A^{l*}_{m} \hat{A}^{l}_{\mathbf{r}^{(1)},\mathbf{r}^{(1)}+\alpha_m} \right) + h.c. \\ &\quad - \left( \left| B^{l}_{m} \right|^2 - \left| A^{l}_{m} \right|^2 \right) \Big] \\ &\quad +J_2 \sum_{n} \sum_{\mathbf{r}^{(n)},lm} \Big[ \left( B^{l(n)*}_{m} \hat{B}^{l}_{\mathbf{r}^{(n)},\mathbf{r}^{(n)}+\beta_m} - A^{l(n)*}_{m} \hat{A}^{l}_{\mathbf{r}^{(n)},\mathbf{r}^{(n)}+\beta_m} \right) + h.c. \\ &\quad - \left( \left| B^{l(n)}_{m} \right|^2 - \left| A^{l(n)}_{m} \right|^2 \right) \Big] \end{aligned}$$

$$+J_{\perp}\sum_{n}\sum_{\mathbf{r}^{(n)}}\Big[\Big(B^{\perp(n)*}\hat{B}^{\perp}_{\mathbf{r}^{(n)},\mathbf{r}^{(n)}}-A^{\perp(n)*}\hat{A}^{\perp}_{\mathbf{r}^{(n)},\mathbf{r}^{(n)}}\Big)+h.c.$$
$$-\Big(\big|B^{\perp(n)}\big|^2-\big|A^{\perp(n)}\big|^2\Big)\Big]. \tag{3.4}$$

As we have done in Chapter 2, the local constraint of the number of Schwinger bosons per site is enforced by a Lagrange multiplier $\lambda_{\mathbf{R}}$ at each site. We replace the local Lagrange multiplier $\lambda_{\mathbf{R}}$ by parameters $\lambda^{(n)}$ for each sublattice, which is a crucial approximation in Schwinger bosons mean-field theory:

$$\hat{H}_{MF}\rightarrow\hat{H}_{MF}+\hat{H}_{\lambda} \tag{3.5}$$

with

$$\hat{H}_{\lambda}=\sum_{n=1,2}\sum_{\mathbf{r}^{(n)},l=1,2}\lambda^{l(n)}\left(\sum_{\mu=\uparrow,\downarrow}\hat{b}^{l\dagger}_{\mathbf{r}^{(n)}\mu}\hat{b}^{l}_{\mathbf{r}^{(n)}\mu}-2S\right). \tag{3.6}$$

We perform Fourier transformation for Schwinger bosons on each sublattice:

$$\hat{b}^{l}_{\mathbf{r}^{(n)}\mu}=\frac{1}{\sqrt{N/2}}\sum_{\mathbf{k}\in BZ}\hat{b}^{l(n)}_{\mathbf{k}\mu}\exp\left(i\mathbf{k}\cdot\mathbf{r}^{(n)}\right), \tag{3.7}$$

where $N$ is the total number of lattice sites for one layer. In the $\mathbf{k}$-space, the mean-field Hamiltonian can be represented in the following compact form (In the following we will assume the mean fields $A$ and $B$ to be real):

$$\hat{H}_{MF}=\sum_{\mathbf{k}}\hat{\phi}^{\dagger}_{\mathbf{k}}\tilde{M}_{\mathbf{k}}\hat{\phi}_{\mathbf{k}}+E_0, \tag{3.8}$$

where we introduce the Nambu spinor in the momentum space:

$$\hat{\phi}_{\mathbf{k}}=\Big(\ \hat{b}^{1(1)}_{\mathbf{k}\uparrow},\ \hat{b}^{1(2)}_{\mathbf{k}\uparrow},\ \hat{b}^{2(1)}_{\mathbf{k}\uparrow},\ \hat{b}^{2(2)}_{\mathbf{k}\uparrow},\ \hat{b}^{1(1)\dagger}_{-\mathbf{k}\downarrow},\ \hat{b}^{1(2)\dagger}_{-\mathbf{k}\downarrow},\ \hat{b}^{2(1)\dagger}_{-\mathbf{k}\downarrow},\ \hat{b}^{2(2)\dagger}_{-\mathbf{k}\downarrow}\ \Big)^{\mathsf{T}}, \tag{3.9}$$

and

$$\begin{aligned}-E_0 \ &= \ \frac{N}{2}J_1\sum_{lm}\Big(\big(B^{l}_{m}\big)^2-\big(A^{l}_{m}\big)^2\Big)+\frac{N}{2}J_2\sum_{l,n,m}\Big(\big(B^{l(n)}_{m}\big)^2-\big(A^{l(n)}_{m}\big)^2\Big)\\ &\quad+\frac{N}{2}J_{\perp}\sum_{n}\Big(\big(B^{\perp(n)}\big)^2-\big(A^{\perp(n)}\big)^2\Big)+(2S+1)\,\frac{N}{2}\sum_{ln}\lambda^{l(n)}. \end{aligned}\tag{3.10}$$

is a constant. The $8 \times 8$ dynamical matrix $\tilde{M}_{\mathbf{k}}$ is given by

$$\tilde{M}_{\mathbf{k}} = \begin{pmatrix} M_{\mathbf{k}}^{B} & -M_{\mathbf{k}}^{A} \\ M_{\mathbf{k}}^{A} & M_{\mathbf{k}}^{B} \end{pmatrix}, \tag{3.11}$$

where

$$M_{\mathbf{k}}^{B} = \begin{pmatrix} \Gamma_{\mathbf{k}}^{B1} + \Lambda^{1} & \Gamma^{B\perp} \\ \Gamma^{B\perp} & \Gamma_{\mathbf{k}}^{B2} + \Lambda^{2} \end{pmatrix}, \quad M_{\mathbf{k}}^{A} = \begin{pmatrix} \Gamma_{\mathbf{k}}^{A1} & \Gamma^{A\perp} \\ -\Gamma^{A\perp} & \Gamma_{\mathbf{k}}^{A2} \end{pmatrix} \tag{3.12}$$

with the following definitions of matrices:

$$\Lambda^{l} = \begin{pmatrix} \lambda^{l(1)} & 0 \\ 0 & \lambda^{l(2)} \end{pmatrix}, \tag{3.13}$$

$$\Gamma_{\mathbf{k}}^{Bl} = \begin{pmatrix} J_2 \sum_m B_m^{l(1)} \cos\left(\mathbf{k}\cdot\beta_m\right) & \frac{J_1}{2} \sum_m B_m^{l} \exp\left(i\mathbf{k}\cdot\alpha_m\right) \\ \frac{J_1}{2} \sum_m B_m^{l} \exp\left(-i\mathbf{k}\cdot\alpha_m\right) & J_2 \sum_m B_m^{l(2)} \cos\left(\mathbf{k}\cdot\beta_m\right) \end{pmatrix}, \tag{3.14}$$

$$\Gamma_{\mathbf{k}}^{Al} = \begin{pmatrix} iJ_2 \sum_m A_m^{l(1)} \sin\left(\mathbf{k}\cdot\beta_m\right) & \frac{J_1}{2} \sum_m A_m^{l} \exp\left(i\mathbf{k}\cdot\alpha_m\right) \\ -\frac{J_1}{2} \sum_m A_m^{l} \exp\left(-i\mathbf{k}\cdot\alpha_m\right) & iJ_2 \sum_m A_m^{l(2)} \sin\left(\mathbf{k}\cdot\beta_m\right) \end{pmatrix} \tag{3.15}$$

$$\Gamma^{B\perp} = \frac{J_\perp}{2} \begin{pmatrix} B^{\perp(1)} & 0 \\ 0 & B^{\perp(2)} \end{pmatrix}, \tag{3.16}$$

$$\Gamma^{A\perp} = \frac{J_\perp}{2} \begin{pmatrix} A^{\perp(1)} & 0 \\ 0 & A^{\perp(2)} \end{pmatrix}. \tag{3.17}$$

As we have done in Chapter 2, para-unitary diagonalization [114] of $M_{\mathbf{k}}$ can be achieved by defining the new boson operators $\hat{\phi}_{\mathbf{k}} = F_{\mathbf{k}}\hat{\psi}_{\mathbf{k}}$, where $F_{\mathbf{k}}$ satisfies

$$F_{\mathbf{k}}^{\dagger}\varphi F_{\mathbf{k}} = \varphi, \quad \varphi = \begin{pmatrix} I_{4\times4} & 0 \\ 0 & -I_{4\times4} \end{pmatrix}. \tag{3.18}$$

Therefore, the mean-field Hamiltonian is diagonalized as follows:

$$\hat{H}_{MF} = \sum_{\mathbf{k}} \hat{\psi}_{\mathbf{k}}^{\dagger} \cdot \mathbf{E}\left(\mathbf{k}\right) \cdot \hat{\psi}_{\mathbf{k}} + E_0, \tag{3.19}$$

where

$$\mathbf{E}\left(\mathbf{k}\right) = \mathrm{diag}\left[\omega_1\left(\mathbf{k}\right), \omega_2\left(\mathbf{k}\right), \omega_3\left(\mathbf{k}\right), \omega_4\left(\mathbf{k}\right), \omega_1\left(\mathbf{k}\right), \omega_2\left(\mathbf{k}\right), \omega_3\left(\mathbf{k}\right), \omega_4\left(\mathbf{k}\right)\right]. \tag{3.20}$$

On the other hand, from the inverse of the Bogoliubov transformation matrix [114]

$$F_{\mathbf{k}} = \begin{pmatrix} U_{\mathbf{k}} & -V_{\mathbf{k}} \\ V_{\mathbf{k}} & U_{\mathbf{k}} \end{pmatrix}, \tag{3.21}$$

we can establish the mean-field equations by calculating the expectation values of corresponding operators directly:

$$\begin{aligned} A_m^l &= \frac{1}{2} \times \frac{2}{N} \sum_{\mathbf{k},\mathbf{k}'} \exp\left[i\mathbf{k}\cdot\mathbf{r}^{(1)} + i\mathbf{k}'\cdot\left(\mathbf{r}^{(1)}+\alpha_m\right)\right] \left(\left\langle \hat{b}_{\mathbf{k}\uparrow}^{l(1)} \hat{b}_{\mathbf{k}'\downarrow}^{l(2)} \right\rangle - \left\langle \hat{b}_{\mathbf{k}\downarrow}^{l(1)} \hat{b}_{\mathbf{k}'\uparrow}^{l(2)} \right\rangle\right) \\ &= \frac{1}{N} \sum_{\mathbf{k}} \left[\left(U_{\mathbf{k}} V_{\mathbf{k}}^{\dagger}\right)_{2l-1,2l} \exp\left(-i\mathbf{k}\cdot\alpha_m\right) + c.c.\right], \end{aligned} \tag{3.22}$$

$$\begin{aligned} A_m^{l(n)} &= \frac{1}{2} \times \frac{2}{N} \sum_{\mathbf{k},\mathbf{k}'} \exp\left[i\mathbf{k}\cdot\mathbf{r}^{(n)} + i\mathbf{k}'\cdot\left(\mathbf{r}^{(n)}+\beta_m\right)\right] \left(\left\langle \hat{b}_{\mathbf{k}\uparrow}^{l(n)} \hat{b}_{\mathbf{k}'\downarrow}^{l(n)} \right\rangle - \left\langle \hat{b}_{\mathbf{k}\downarrow}^{l(n)} \hat{b}_{\mathbf{k}'\uparrow}^{l(n)} \right\rangle\right) \\ &= \frac{1}{N} \sum_{\mathbf{k}} \left[\exp\left(-i\mathbf{k}\cdot\beta_m\right) \left(U_{\mathbf{k}} V_{\mathbf{k}}^{\dagger}\right)_{2l+n-2,2l+n-2} + c.c.\right], \end{aligned} \tag{3.23}$$

$$\begin{aligned} A^{\perp(n)} &= \frac{1}{2} \times \frac{2}{N} \sum_{\mathbf{k},\mathbf{k}'} \exp\left[i\left(\mathbf{k}+\mathbf{k}'\right)\cdot\mathbf{r}^{(n)}\right] \left(\left\langle \hat{b}_{\mathbf{k}\uparrow}^{1(n)} \hat{b}_{\mathbf{k}'\downarrow}^{2(n)} \right\rangle - \left\langle \hat{b}_{\mathbf{k}\downarrow}^{1(n)} \hat{b}_{\mathbf{k}'\uparrow}^{2(n)} \right\rangle\right) \\ &= \frac{1}{N} \sum_{\mathbf{k}} \left[\left(U_{\mathbf{k}} V_{\mathbf{k}}^{\dagger}\right)_{n,n+2} + c.c.\right], \end{aligned} \tag{3.24}$$

$$
\begin{aligned}
B_m^l &= \frac{1}{2}\times\frac{2}{N}\sum_{\mathbf{k},\mathbf{k}'}\exp\left[-i\mathbf{k}\cdot\mathbf{r}^{(1)}+i\mathbf{k}'\cdot\left(\mathbf{r}^{(1)}+\alpha_m\right)\right]\left(\left\langle\hat{b}_{\mathbf{k}\uparrow}^{l(1)\dagger}\hat{b}_{\mathbf{k}'\uparrow}^{l(2)}\right\rangle+\left\langle\hat{b}_{\mathbf{k}\downarrow}^{l(1)\dagger}\hat{b}_{\mathbf{k}'\downarrow}^{l(2)}\right\rangle\right)\\
&= \frac{1}{N}\sum_{\mathbf{k}}\left[\left(V_{\mathbf{k}}V_{\mathbf{k}}^{\dagger}\right)_{2l-1,2l}\exp\left(-i\mathbf{k}\cdot\alpha_m\right)+c.c.\right], \qquad (3.25)
\end{aligned}
$$

$$
\begin{aligned}
B_m^{l(n)} &= \frac{1}{2}\times\frac{2}{N}\sum_{\mathbf{k},\mathbf{k}'}\exp\left[-i\mathbf{k}\cdot\mathbf{r}^{(n)}+i\mathbf{k}'\cdot\left(\mathbf{r}^{(n)}+\beta_m\right)\right]\left(\left\langle\hat{b}_{\mathbf{k}\uparrow}^{l(n)\dagger}\hat{b}_{\mathbf{k}'\uparrow}^{l(n)}\right\rangle+\left\langle\hat{b}_{\mathbf{k}\downarrow}^{l(n)\dagger}\hat{b}_{\mathbf{k}'\downarrow}^{l(n)}\right\rangle\right)\\
&= \frac{1}{N}\sum_{\mathbf{k}}\left[\left(V_{\mathbf{k}}V_{\mathbf{k}}^{\dagger}\right)_{2l+n-2,2l+n-2}\exp\left(-i\mathbf{k}\cdot\beta_m\right)+c.c.\right], \qquad (3.26)
\end{aligned}
$$

$$
\begin{aligned}
B^{\perp(n)} &= \frac{1}{2}\times\frac{2}{N}\sum_{\mathbf{k},\mathbf{k}'}\exp\left[i\left(\mathbf{k}'-\mathbf{k}\right)\cdot\mathbf{r}^{(n)}\right]\left(\left\langle\hat{b}_{\mathbf{k}\uparrow}^{1(n)\dagger}\hat{b}_{\mathbf{k}'\uparrow}^{2(n)}\right\rangle+\left\langle\hat{b}_{\mathbf{k}\downarrow}^{1(n)\dagger}\hat{b}_{\mathbf{k}'\downarrow}^{2(n)}\right\rangle\right)\\
&= \frac{1}{N}\sum_{\mathbf{k}}\left[\left(V_{\mathbf{k}}V_{\mathbf{k}}^{\dagger}\right)_{n,n+2}+c.c.\right]. \qquad (3.27)
\end{aligned}
$$

The four constraints in the number of Schwinger bosons can be written in the momentum space as

$$
\begin{aligned}
2S &= \frac{2}{N}\sum_{\mathbf{k},\mathbf{k}'}\exp\left[i\left(\mathbf{k}'-\mathbf{k}\right)\cdot\mathbf{r}^{(n)}\right]\left(\left\langle\hat{b}_{\mathbf{k}\uparrow}^{l(n)\dagger}\hat{b}_{\mathbf{k}'\uparrow}^{l(n)}\right\rangle+\left\langle\hat{b}_{\mathbf{k}\downarrow}^{l(n)\dagger}\hat{b}_{\mathbf{k}'\downarrow}^{l(n)}\right\rangle\right)\\
&= \frac{2}{N}\sum_{\mathbf{k}}\left[\left(V_{\mathbf{k}}V_{\mathbf{k}}^{\dagger}\right)_{\nu\nu}+c.c.\right], \qquad (3.28)
\end{aligned}
$$

where $\nu = 1, 2, 3, 4$. The number of parameters to be determined is 44. Since we have two layers, for three nearest neighbor bonds, we have six $A_m^l$ and six $B_m^l$ in total. For three second neighbor bonds, we have again six $A_m^{l(n)}$ and six $B_m^{l(n)}$ for each sublattice ($n = 1, 2$). For the interlayer coupling, we have two $A^{\perp(n)}$ and two $B^{\perp(n)}$. In addition to these 40 mean-field parameters, we also need to determine four Lagrange multipliers, which are chemical potential of Schwinger bosons. In the following, unless being explicitly specified, we fix the energy scale by taking $J_1 = 1$ to simplify the notation.

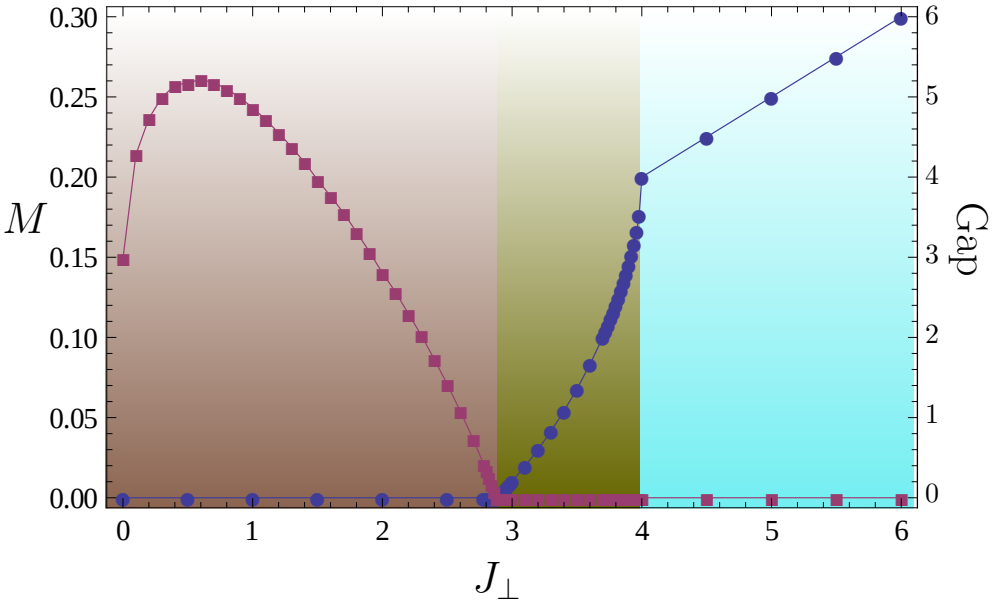


Figure 3.2: The spin gap (blue circles) and sublattice magnetization (red squares) obtained by the Schwinger boson mean-field theory extrapolated to the thermodynamic limit at $J_2 = 0.1$, corresponding to the dashed line in Fig. 3.3. For $J_\perp > 4$ the gap is proportional to $J_\perp$. The sublattice magnetization is enhanced by small interlayer coupling, reaching a maximum at $J_\perp \sim 1/2$, after that it decreases until disappearing at $J_\perp \sim 2.9$. The brown shaded region corresponds to the Néel phase. In the green and light-blue regions, there is no evidence of any kind of magnetic order, and the light-blue region presents a gap that depends linearly with $J_\perp$.

## 3.3 Results

Using the Schwinger boson mean-field theory we study some features of the ground-state phase diagram in the $J_2$-$J_\perp$ plane. The line $J_\perp = 0$ corresponds to the phase diagram for the single layer honeycomb lattice. The phase diagram of the single layer model was studied in detail in Chapter 2. The Schwinger boson mean-field theory is useful to determine whether the system remains gapless or not within its approximation. To obtain the phase boundary between the magnetically ordered and disordered phases we use the value of the gap in the excitation spectrum extrapolated to the thermo-

dynamic limit. The fitting function is also a fourth order polynomial function of $1/L$, which is similar to the one we use in Chapter 2. In the gapless region the excitation spectrum is zero at $\mathbf{k} = 0$, where the boson condensation occurs, and this is characteristic of the Néel ordered phase. On the other hand, in the gapped region, the absence of gapless point indicates that the ground state is magnetically disordered. In Fig. 3.2 the extrapolated value of the spin gap and sublattice magnetization [55, 97, 98] for $J_2 = 0.1$ (dashed line in Fig. 3.3) is presented as a function of the interlayer coupling $J_\perp$. For small values of the interlayer coupling the system remains gapless, and the sublattice magnetization is nonzero. As we increase $J_\perp$ the spin gap opens and the sublattice magnetization vanishes at a value $J_\perp^*(J_2)$. In Fig. 3.2, $J_\perp^*(0.1) \sim 2.9$. The sublattice magnetization has an initial growth at small $J_\perp$ and suppression at larger $J_\perp$. At the critical value $J_\perp^*(J_2)$ the Néel order is destroyed leading to a nonmagnetic ground state composed of correlated interlayer dimers. Increasing further the interlayer coupling, the gap becomes a nearly linear function of $J_\perp$, and this corresponds to the triplon gap in the interlayer dimer ground state. For $J_\perp > 4$ clearly the spin gap is $\Delta \approx J_\perp$, which is a signature of the perfect dimer product phase within our treatment. Since a small bilayer coupling enhances the antiferromagnetic long-range order [76, 83], the sublattice magnetization is enhanced by small interlayer coupling, reaching a maximum at $J_\perp \sim 1/2$, after that it decreases until disappearing at $J_\perp \sim 2.9$. As is known, mean-field techniques are not the most convenient methods to study the properties of a system near a phase transition, so it may be difficult to determine quantitatively the transition between Neel and disordered phases using only Schwinger boson mean-field theory. For this reason, in our case, we would tend to conclude that the abrupt change of behavior in the spin gap at $J_\perp = 4$ in Fig. 3.2 does not indicate a phase transition, but could be an indication of the breakdown of the mean-field calculation. If we consider the quantum fluctuations beyond the mean field level, this abrupt change may change to the crossover. Actual physical quantities, such as the sublattice magnetization and spin-spin correlations, calculated in green and light-blue shadowed regions of Fig. 3.2 do not show qualitative differences.

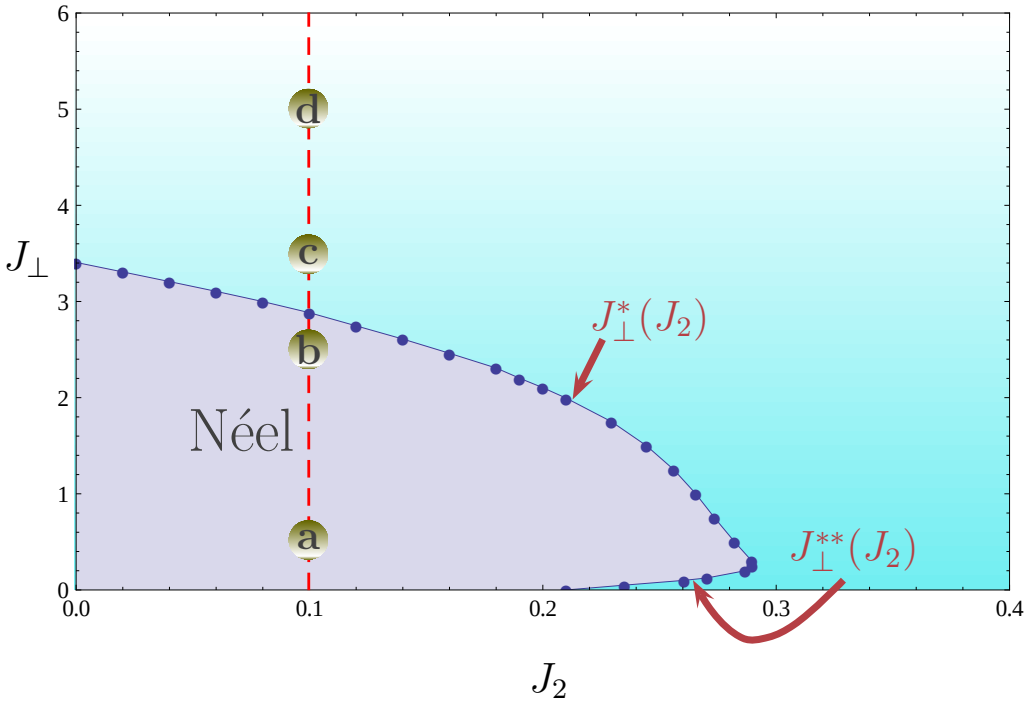


Figure 3.3: Néel phase boundary in the $J_2$-$J_\perp$ plane obtained by means of the Schwinger boson mean-field theory (spin $S = 1/2$). Along the dashed line ($J_2 = 0.1$), we choose four typical points: $J_\perp/J_1 =$ (a) 0.5, (b) 2.5, (c) 3.5, and (d) 5.0. In the region $0.2075 \lesssim J_2 \lesssim 0.289$, a reentrant behavior exists. $J_\perp^*(J_2)$ is the upper phase boundary, and $J_\perp^{**}(J_2)$ is the lower phase boundary.

In Fig. 3.3 we show the ground-state phase diagram in the $J_2$-$J_\perp$ plane for the $S = 1/2$. To determine the phase boundary we use the value where the gap in the excitation spectrum vanishes in the thermodynamic limit. The fitting function for extrapolation to the thermodynamic limit is also a fourth order polynomial function of $1/L$, which is similar to the one we use in Chapter 2. For $J_\perp \gg J_2$ one expects a interlayer dimer ground state that adiabatically connects with the limit of decoupled dimers, i.e. two singlets per unit cell made of spins 1 and 3, and 2 and 4 (see Fig. 3.1). In this limit the ground state energy per dimer is $E = -\frac{3}{4}J_\perp$, with an energy gap $\Delta = J_\perp$ to triplet magnetic excitations. In Fig. 3.2 for $J_\perp > 4$ clearly the spin gap

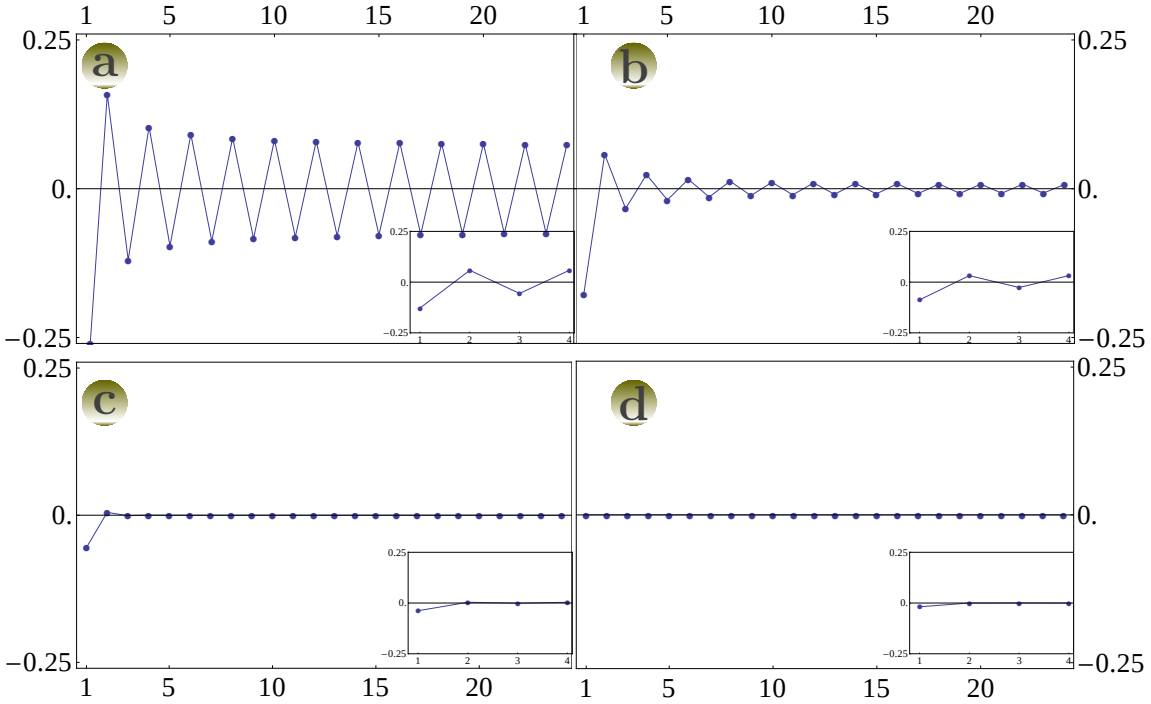


Figure 3.4: Spin correlations obtained by Schwinger boson mean-field theory for $2 \times 2 \times 50 \times 50$ sites system. The labels a,b,c,d correspond to the points showed in Fig. 3.3 ((a)$J_\perp/J_1 = 0.5$, (b)$J_\perp/J_1 = 2.5$, (c)$J_\perp/J_1 = 3.5$, and (d)$J_\perp/J_1 = 5.0$). The insets shows the same correlations obtained by Lanczos diagonalization of a 24 sites system performed by C. A. Lamas [90].

$\Delta \approx J_\perp$, which is a signature of the mentioned phase.

In order to support the analytical results of the mean-field approach, the author proposed C. A. Lamas to perform Lanczos exact diagonalization calculations, and he calculated a finite system of 24 spins with $S = 1/2$ and periodic boundary conditions in two directions in the layer [90]. The bilayer structure of the lattice makes analysis particularly difficult because there are four sites per unit cell and the system contains only 6 unit cells. In particular, correlation functions between spins in the same layer can be studied only for a few neighbors. Fig. 3.4 shows the spin correlations in the same layer in the zig-zag direction obtained by Schwinger boson mean-field theory corresponding to the points (a)–(d) in Fig. 3.3 for $2 \times 2 \times 50 \times 50$ sites

system. The insets are the exact diagonalization results calculated by C. A. Lamas for the same points for a 24-site system. Although correlations are calculated only for a few sites in exact diagonalization, the absence of antiferromagnetic long-range order in the insets of Fig. 3.4(c) and (d) is clear. This is consistent with the Schwinger boson mean-field theory results corresponding to the main figures. The results of exact diagonalization in the insets of Fig. 3.4(c) and (d) clearly show only short-range antiferromagnetic correlations. The Schwinger boson mean-field theory results in Fig. 3.4(c) also show short-range antiferromagnetic correlations, and this corresponds to the interlayer dimer phase composed of correlated interlayer dimers. However, in Fig. 3.4(d) the interlayer dimers are decoupled, and the system belongs to the perfect interlayer dimer product state within the Schwinger boson mean-field treatment. In Fig. 3.5 we show the energy per dimer for $J_2 = 0.18$ in units of $J_\perp$ calculated with Schwinger boson mean-field theory (blue circles) and exact diagonalization for a system with 24 sites (red squares). As it can be observed the energy per dimer becomes close to the value of the dimer product state $\dfrac{E}{2NJ_\perp} = -3/4$, already for $J_\perp \simeq 3$.

As showed in the phase diagram Fig. 3.3, there is a reentrant behavior in the region $0.2075 \lesssim J_2 \lesssim 0.289$. In this region, Néel phase separates from $J_2$ axis, leaving a tiny space for a magnetically disordered phase. In this way Néel phase is here not only limited by $J_\perp^*(J_2)$ critical line from above, but also by a second $J_\perp^{**}(J_2)$ critical line from below (See Fig. 3.3). In Fig. 3.2, we show the sublattice magnetization [55,97,98] along the line $J_2 = 0.1$. It is clear that a small bilayer coupling enhances the antiferromagnetic long-range order [76,83], which is the reason of the reentrant effect.

On the other hand, in the range $0.3732 \lesssim J_2 \lesssim 0.398$ at $J_\perp = 0$, an exact diagonalization calculation [90] shows an evidence of the existence of an intra-layer nematic VBC phase [55] as we have discussed in Chapter 2 for the single layer case, but we do not analyze this point further in this thesis. In this VBC phase SU(2) spin rotational and lattice translational symmetries are preserved. However, the lattice $C_3$ symmetry, corresponding to $2\pi/3$

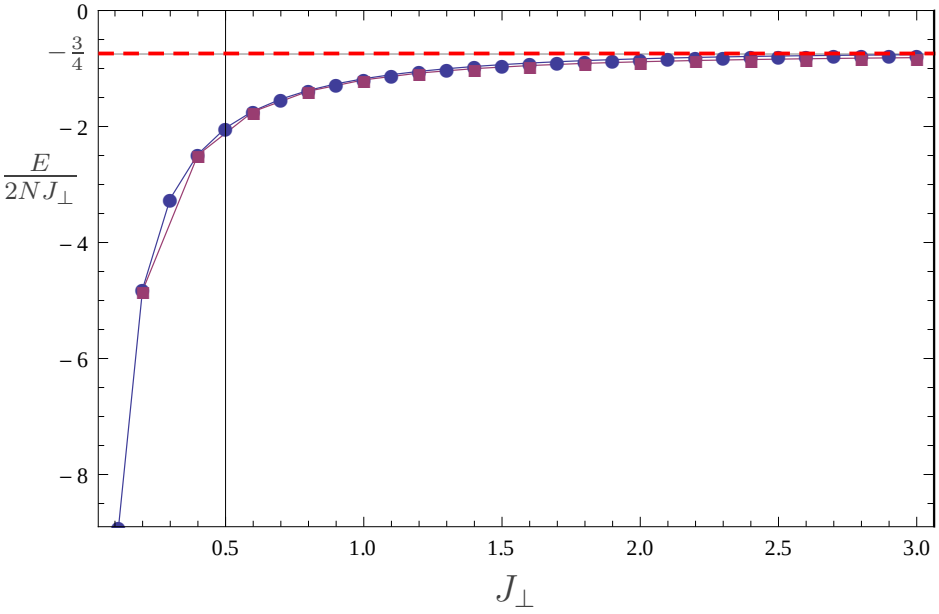


Figure 3.5: Ground state energy per dimer over $J_\perp$ as a function of $J_\perp$ for $J_2 = 0.18$. Results calculated by means of the Schwinger boson mean-field theory extrapolated to the thermodynamic limit (blue circles) are compared to Lanczos exact diagonalization performed by C. A. Lamas [90] for a 24 sites system (red squares). Horizontal dashed line indicates to $\frac{E}{2NJ_\perp} = -3/4$ corresponding to an isolated interlayer dimer.

rotations around an axis perpendicular to the plane and passing through a site, is broken. We expect that with increasing the interlayer coupling $J_\perp$, the system moves to the interlayer dimer state, where the $C_3$ symmetry is recovered. We will check this point in our future work.

Finally, in the region $0.289 \lesssim J_2/J_1 \lesssim 0.3732$ the ground state preserves spin rotational and lattice translational symmetries and the spin-spin correlations are short ranged. This agrees with the evidence of a spin liquid phase in the phase diagram corresponding to $J_\perp = 0$ [39, 40, 55]. We expect that $C_3$ lattice rotational symmetry is not broken, but again this needs a future work.

## 3.4 Linear spin wave theory

In this section we use a linear spin wave approach to study the stability of Néel order as a function of the spin quantum number $S$. The classical ground state of the Hamiltonian (3.1) for $J_2 < \frac{1}{6}J_1$ is given by an antiparallel (Néel) configuration. Incorporating quantum fluctuation to the classical ground state may lead to the melting of Neél order.

For the spin wave implementation it is convenient to define new spin operators $\tilde{\mathbf{S}}$ rotating by $\pi$ about the $x$-axis for the spins on the sublattices 2 and 3 (See Fig. 3.1). After the rotation we have

$$\begin{aligned} \tilde{S}^x_\alpha(\mathbf{r}) &= S^x_\alpha(\mathbf{r}), && (3.29)\\ \tilde{S}^y_\alpha(\mathbf{r}) &= -S^y_\alpha(\mathbf{r}), && (3.30)\\ \tilde{S}^z_\alpha(\mathbf{r}) &= -S^z_\alpha(\mathbf{r}), && (3.31) \end{aligned}$$

for spin operators on the sublattices 2 or 3, while $\tilde{\mathbf{S}}_\alpha(\mathbf{r}) = \mathbf{S}_\alpha(\mathbf{r})$ for the sublattices 1 and 4. Thereby, the classical ground state have all spins pointing toward the new $+\tilde{S}^z$ axis.

The next step is to write the spin operators in terms of Holstein-Primakoff bosons as follows

$$\begin{aligned} \tilde{S}^+_\alpha(\mathbf{r}) &= \sqrt{2S}a_\alpha(\mathbf{r}), && (3.32)\\ \tilde{S}^-_\alpha(\mathbf{r}) &= \sqrt{2S}a^\dagger_\alpha(\mathbf{r}), && (3.33)\\ \tilde{S}^z_\alpha(\mathbf{r}) &= S - n_\alpha(\mathbf{r}). && (3.34) \end{aligned}$$

The Hamiltonian is now written in terms of these boson operators as

$$H = E_0 + H_{SW}, \tag{3.35}$$

with

$$\begin{aligned} E_0 &= 2NS^2(6J_2 - 3J_1 - J_\perp) && (3.36)\\ H_{SW} &= 2NS(6J_2 - 3J_1 - J_\perp) \end{aligned}$$

$$+ \quad \sum_{\mathbf{k}>0} \mathbf{a}^\dagger(\mathbf{k}) \mathcal{M}(\mathbf{k}) \mathbf{a}(\mathbf{k}). \tag{3.37}$$

Here $\sum_{\mathbf{k}>0}$ means that the sum runs over a half the first Brillouin zone, and we introduce the vector of bosons in the momentum space:

$$\mathbf{a}(\mathbf{k}) = \Big( \; a_1(\mathbf{k}), \;\; a_2(\mathbf{k}), \;\; a_3(\mathbf{k}), \;\; a_4(\mathbf{k}), \;\; a_1^\dagger(-\mathbf{k}), \;\; a_2^\dagger(-\mathbf{k}), \;\; a_3^\dagger(-\mathbf{k}), \;\; a_4^\dagger(-\mathbf{k}) \; \Big)^\intercal. \tag{3.38}$$

The $8 \times 8$ matrix $\mathcal{M}(\mathbf{k})$ is given by

$$\mathcal{M}(\mathbf{k}) = \begin{pmatrix} M_2(\mathbf{k}) & M_1(\mathbf{k}) \\ M_1(\mathbf{k}) & M_2(\mathbf{k}) \end{pmatrix}, \tag{3.39}$$

where

$$M_2(\mathbf{k}) = \begin{pmatrix} \gamma_2(\mathbf{k}) & 0 & 0 & 0 \\ 0 & \gamma_2(\mathbf{k}) & 0 & 0 \\ 0 & 0 & \gamma_2(\mathbf{k}) & 0 \\ 0 & 0 & 0 & \gamma_2(\mathbf{k}) \end{pmatrix}, \tag{3.40}$$

$$M_1(\mathbf{k}) = \begin{pmatrix} 0 & \gamma_1(-\mathbf{k}) & \gamma_\perp & 0 \\ \gamma_1(\mathbf{k}) & 0 & 0 & \gamma_\perp \\ \gamma_\perp & 0 & 0 & \gamma_1(-\mathbf{k}) \\ 0 & \gamma_\perp & \gamma_1(\mathbf{k}) & 0 \end{pmatrix}, \tag{3.41}$$

and functions $\gamma_1$, $\gamma_2$ and $\gamma_\perp$ are given by

$$\gamma_1(\mathbf{k}) = \frac{1}{2} J_1 S (1 + e^{i\mathbf{k}\cdot\mathbf{e}_1} + e^{-i\mathbf{k}\cdot\mathbf{e}_2}) \tag{3.42}$$

$$\begin{aligned} \gamma_2(\mathbf{k}) &= J_2 S (\cos(\mathbf{k}\cdot\mathbf{e}_1) + \cos(\mathbf{k}\cdot\mathbf{e}_2) + \cos(\mathbf{k}\cdot(\mathbf{e}_1+\mathbf{e}_2))) \\ &+ \frac{3}{2} J_1 S - 3 J_2 S + \frac{1}{2} J_\perp S \end{aligned} \tag{3.43}$$

$$\gamma_\perp = \frac{1}{2} J_\perp S. \tag{3.44}$$

Then we use a Bogoliubov transformation to diagonalize the Hamiltonian

$H_{SW}$ and obtain the following eigenvalues

$$\varepsilon^{\pm}(\mathbf{k}) = \sqrt{(\gamma_2(\mathbf{k}))^2 - (\gamma_\perp \pm |\gamma_1(\mathbf{k})|)^2}, \tag{3.45}$$

which is doubly degenerate. The staggered magnetization is calculated in the linear approximation and the result is

$$\begin{aligned} M &= \frac{1}{4N}\sum_{\mathbf{r},\alpha}\left\langle \tilde{S}^z_\alpha(\mathbf{r})\right\rangle \\ &= S - \frac{1}{4N}\sum_{\mathbf{r},\alpha}\left\langle \mathbf{a}^\dagger_\alpha(\mathbf{r})\mathbf{a}_\alpha(\mathbf{r})\right\rangle . \end{aligned} \tag{3.46}$$

Fluctuations around the Néel state increase with the frustration $J_2$, and can destroy the Néel order. For the smaller value of $S$, quantum fluctuations grow and we expect the melting of the Néel state at some value of $S$. The correction to the classical boundary for the Néel state is determined by finding the frustration $J_2$ at which the staggered magnetization $M$ given by Eq. (3.46) vanishes.

In Fig. 3.6 we present the sublattice magnetization $M$ for $S = 1/2$ as a function of the interlayer coupling ($J_\perp$) corresponding to $J_2 = 0.1$ (dashed line on Figure 3.3).

Notice that, for small values of the interlayer coupling, the magnetization is an increasing function of $J_\perp$, i.e, the antiferromagnetic order is enhanced. But increasing more the value of $J_\perp$ the sublattice magnetization is reduced and vanishes for large values of $J_\perp$. This behavior is in agreement with the Schwinger boson mean-field theory results and the reentrant effect observed in the phase diagram of Fig. 3.3. A similar enhancement in sublattice magnetization was also observed in the bilayer square lattice [76, 83].

In Fig. 3.7, we present the melting curves in the $1/S$-$J_2$ plane for different values of $J_\perp$. The case corresponding to $J_\perp = 0$ agrees with the results of

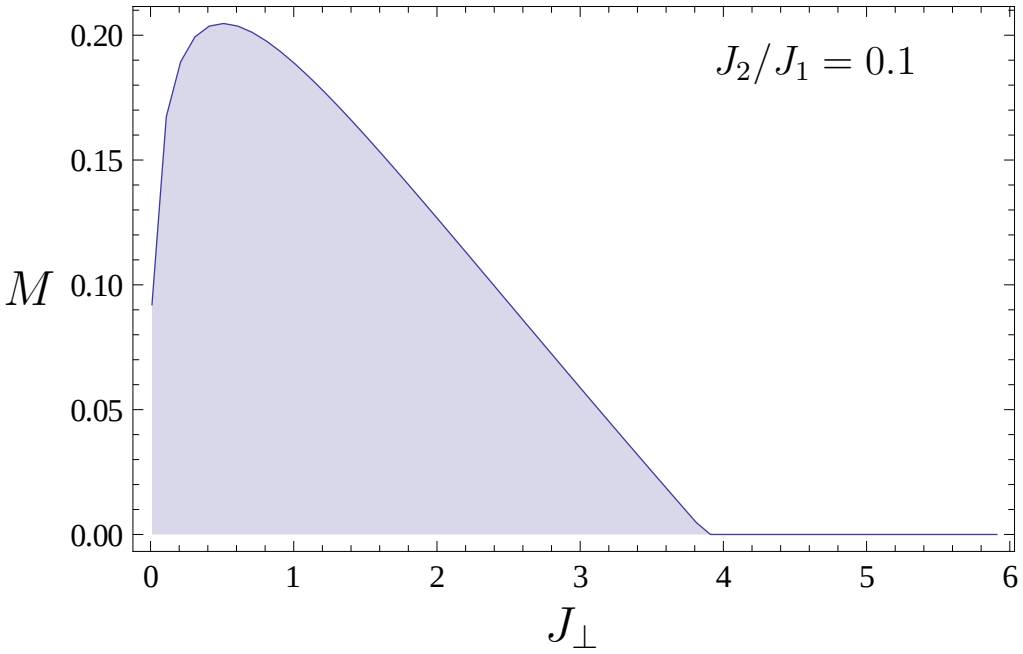


Figure 3.6: Staggered magnetization vs. $J_\perp$ obtained by means of the linear spin wave approximation for $J_2/J_1 = 0.1$. and $S = 1/2$

the linear spin wave theory presented in Fig. 5 of Ref. [31] for the single layer $J_1$-$J_2$ Heisenberg model. For large values of $J_\perp$ the region of the Néel state is reduced. Notice that in Ref. [31] and Ref. [48], the linear spin wave theory and Schwinger bosons mean-field theory disagree about the position of the Néel state boundary. Their difference about the position of the Néel state boundary between the linear spin wave theory and Schwinger bosons mean-field theory may be reduced by including higher order $1/S$ corrections to the linear spin wave theory, which are beyond the scope of the present work.

Finally, in Fig. 3.8 we show the energy dispersion of magnon excitations along the path in the Brillouin zone depicted. As it is shown in Eq. (3.45), the dispersion is twofold degenerate. It is clear that as the interlayer coupling increases, two of the four magnon modes acquires a nonzero gap at the $\Gamma$ point.

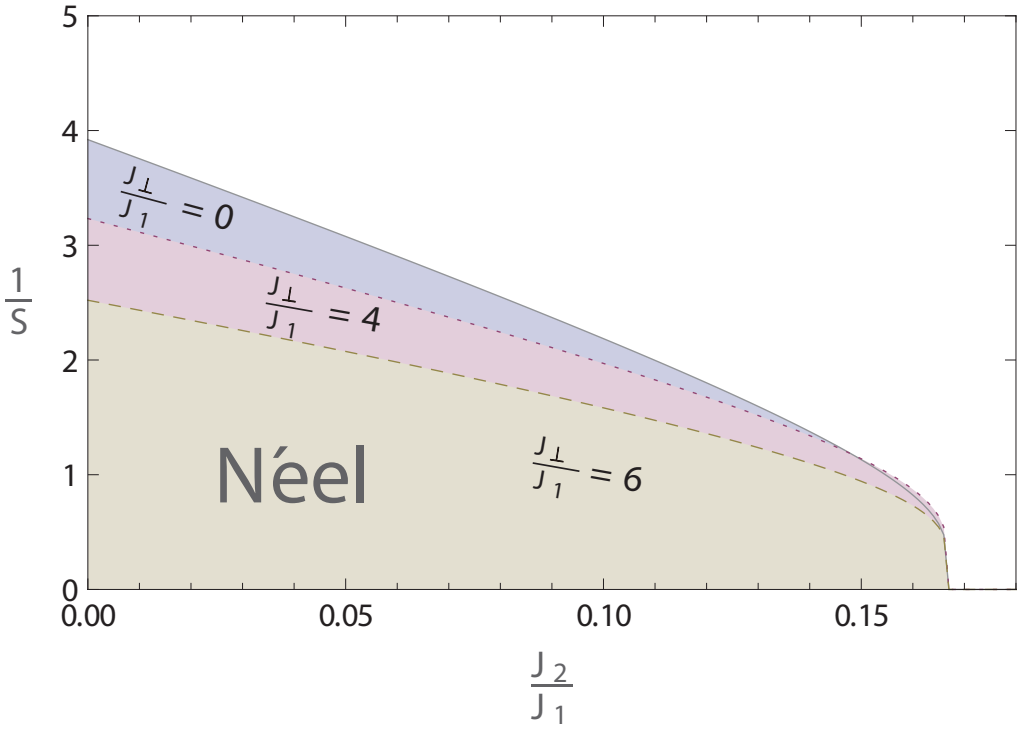


Figure 3.7: Phase diagram in the $1/S$-$J_2$ plane for different values of $J_\perp$ obtained by means of the linear spin wave theory.

## 3.5 Conclusion

In this chapter, we have studied the ground-state phase diagram of a frustrated Heisenberg model on the bilayer honeycomb lattice, by means of Schwinger bosons mean-field theory, complemented with linear spin-wave theory and Lamas' results of exact diagonalization [90]. The results obtained by using different methods are in good agreement.

By analyzing the sublattice magnetization and the spin gap by Schwinger boson mean-field theory, we have estimated the phase boundary for the $S = 1/2$ case between the magnetically ordered (gapless) Néel phase and a magnetically disordered (gapped) phase in $J_2$-$J_\perp$ plane. This melting of Néel order with controlling interlayer coupling $J_\perp$ has also been observed in spin-spin correlations, where Schwinger boson mean-field theory and exact diagonalization calculations predict the same qualitative behavior.

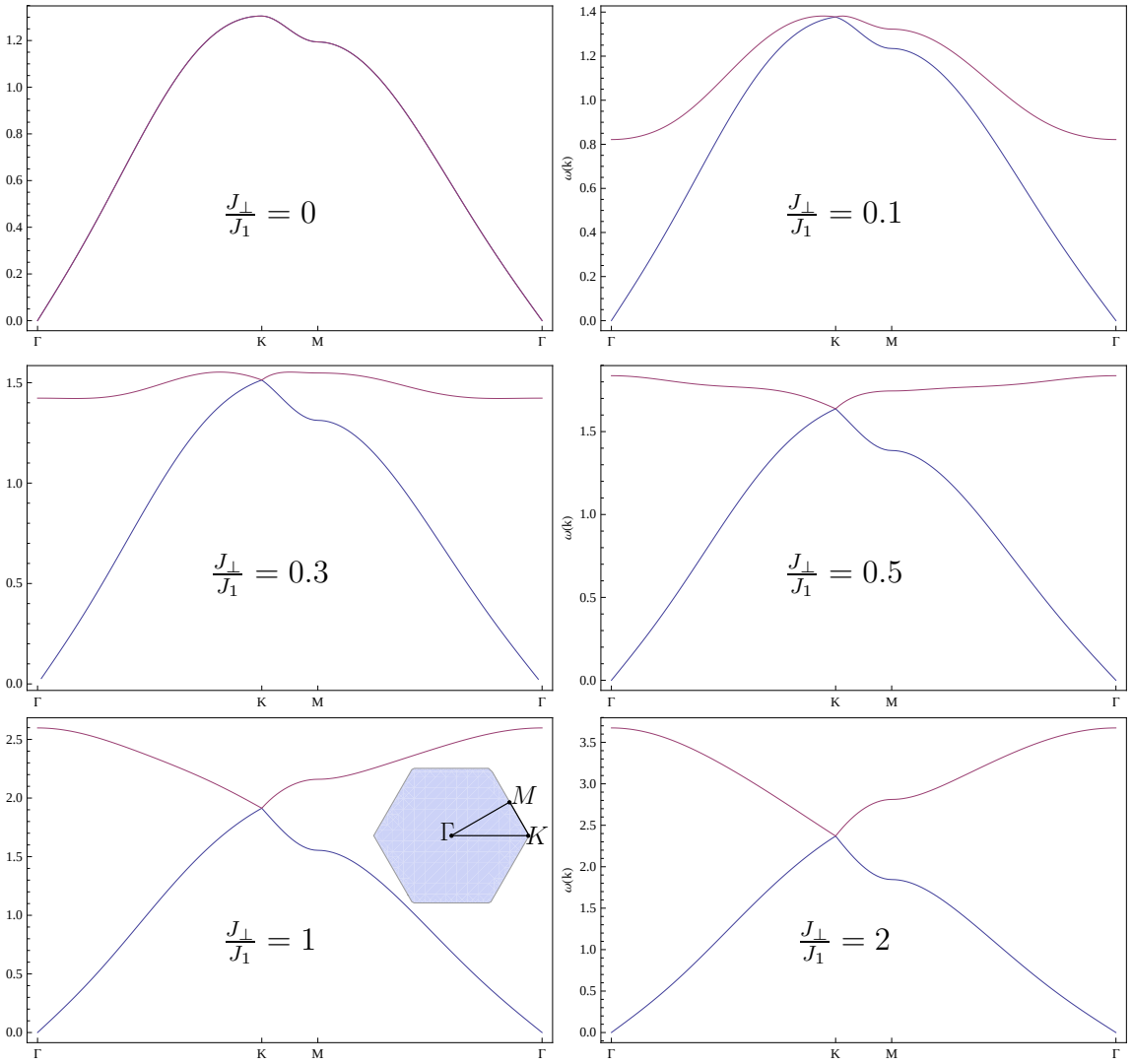


Figure 3.8: Dispersion of magnon energies at $J_2/J_1 = 0.1$ for different values of $J_\perp$ along the path in the Brillouin zone depicted in the bottom left panel. The data are obtained by means of the linear spin wave theory.

In particular, in the small frustration region ($J_2/J_1 \lesssim 0.2075$) the system has the Néel order for $J_\perp = 0$ as discussed in Chapter 2. Increasing the interlayer coupling, the Néel order is destroyed at a critical value $J_\perp^*(J_2)$ and the system enters in a nonmagnetic phase. The boundary of the Néel ordered phase $J_\perp^*(J_2)$ is estimated by extrapolating the spin gap to the thermodynamic limit. The behavior of the spin-spin correlations is consistent with the destruction of the Néel order. For large values of the interlayer coupling, the spin-spin correlations change to have only short-range correlations.

In the region of $0.2075 \lesssim J_2/J_1 \lesssim 0.289$, the boundary of the Néel ordered phase shows a reentrant behavior. At $J_\perp = 0$ the system does not have any magnetic order, but increasing $J_\perp$ up to a finite but small value $J^{**}(J_2)$, the Néel order appears. Increasing further $J_\perp$, the Néel order is destroyed at another critical value $J^*(J_2)$. The behavior of the sublattice magnetization as the function of $J_\perp$ also supports the reentrant behavior.

For $0.289 \lesssim J_2/J_1 \lesssim 0.3732$, the Néel order is absent at $J_\perp = 0$ and the system has a nonzero spin gap, whereas in the region of $0.3732 \lesssim J_2/J_1 \lesssim 0.398$ each layer exhibits a disordered phase with broken $C_3$ lattice rotational symmetry [55]. This was also discussed in the exact diagonalization study [90]. In both cases, with increasing the value of $J_\perp$ the system changes to an interlayer dimer state with a spin gap that is approximately proportional to $J_\perp$.

When $J_\perp/J_1 > 4$, in the entire range of $0 < J_2/J_1 < 0.398$, the system presents signatures of an interlayer dimer state that evolves adiabatically from the limit of decoupled interlayer dimers. It is not easy to determine precisely transitions lines between different magnetically disordered phases. We leave detailed study of these transitions for a future work, as we have focused on the general characteristics of the disordered phases.

Finally, we briefly comment on the implication of our findings in this chapter to the experimental results. As we reviewed in the introduction chapter and Chapter 2, the bismuth manganese oxynitrate $Bi_3Mn_4O_{12}(NO_3)$, which is described by the $S = 3/2$ frustrated Heisenberg model on the bilayer honeycomb lattice, does not show magnetic long-range order down to 0.4K [11]. This indicates the ground state is magnetically disordered [11]. The

estimated values of the interactions by neutron scattering experiments [13,14] are $J_1 = 1.4$ meV, $J_2 = 0.2$ meV and $J_\perp = 0.7$ meV. The estimations of $J_\perp$ by the first principle calculations is, however, larger than $J_1$ [15]. As we have shown in Fig. 3.3, the critical value $J_\perp^*/J_1$ is 2.609 at $J_2/J_1 = 0.14$. Therefore, it is unlikely that the interlayer coupling stabilizes the disordered phase experimentally observed. Another possibility is that some frustration induced magnetically disordered phase may appear, such as the GSL or the staggered VBC which we have shown in Chapter 2. To understand the nature of the ground state of this material, further experimental study is needed to determine more precise value of exchange parameters, as well as theoretical study for $S = 3/2$ case.

# Chapter 4

# Quantum phases in the Heisenberg model on the bilayer honeycomb lattice including interlayer frustration

This chapter presents our study of the Heisenberg antiferromagnetic model on the bilayer honeycomb lattice including interlayer frustration, which is the second way of introducing frustration in the bilayer systems. Sec. 4.1 introduces the model and proves that a product of dimers is the exact ground state of the system on a special line of the parameter space. Sec. 4.2 sketches several qualitative aspects of the quantum phase diagram. In Sec. 4.3 we describe the Schwinger boson mean-field formalism specialized for this model. In Sec. 4.4 we introduce the bond operator approaches. In Sec. 4.5 we analyze the interlayer dimer phase, departing from the line of the exact dimer state. In Sec. 4.6 we characterize the magnetic phases, including Néel-like and collinear states. In Sec. 4.7 we summarize our quantitative findings on the quantum phase diagram. Finally in Sec. 4.8 we present our conclusions.

## 4.1 Bilayer model with interlayer frustration and exact ground state

We study the Heisenberg Hamiltonian on the bilayer honeycomb lattice

$$H = \sum_{\mathbf{r},\mathbf{r}',\alpha,\beta} J_{\alpha,\beta}(\mathbf{r},\mathbf{r}')\hat{\mathbf{S}}_{\alpha}(\mathbf{r})\cdot\hat{\mathbf{S}}_{\beta}(\mathbf{r}'), \tag{4.1}$$

where $\hat{\mathbf{S}}_{\alpha}(\mathbf{r})$ is the spin operator on the site $\alpha$ corresponding to the unit cell $\mathbf{r}$. The index $\alpha$ takes the values $\alpha = 1,A;\ 2,A;\ 1,B;\ 2,B$ corresponding to the four sites on each unit cell and the couplings $J_{\alpha,\beta}(\mathbf{r},\mathbf{r}')$ are depicted in Fig. 4.1.

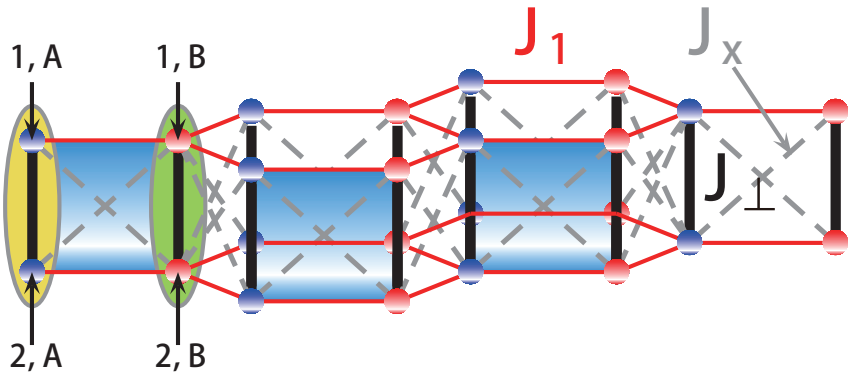


Figure 4.1: The honeycomb lattice with $J_1$, $J_\perp$ and $J_x$ couplings considered in this chapter. Colored areas correspond to the unit cells. $1,A;\ 2,A;\ 1,B;\ 2,B$ correspond to the four sites on one unit cell. Here, the indexes 1 and 2 indicate the two layers. $A$ and $B$ indicate the two sublattices of the honeycomb lattice.

In this chapter we set $J_2 = 0$ and focus on the effect of the interlayer frustration, i.e., we consider the couplings $J_1$, $J_\perp$ and $J_x$ as shown in Fig. 4.1. Interestingly, in that case, the bilayer honeycomb Hamiltonian exhibits an exact dimer-product ground state in a certain region of parameter space, even for finite $J_1$ and $J_x$. This result is valid for arbitrary site spin $S$. Hamiltonians with this property were constructed first by Bose *et al.* [138], based

on methods in Ref. [139], and have been reconsidered in many subsequent studies [140–146].

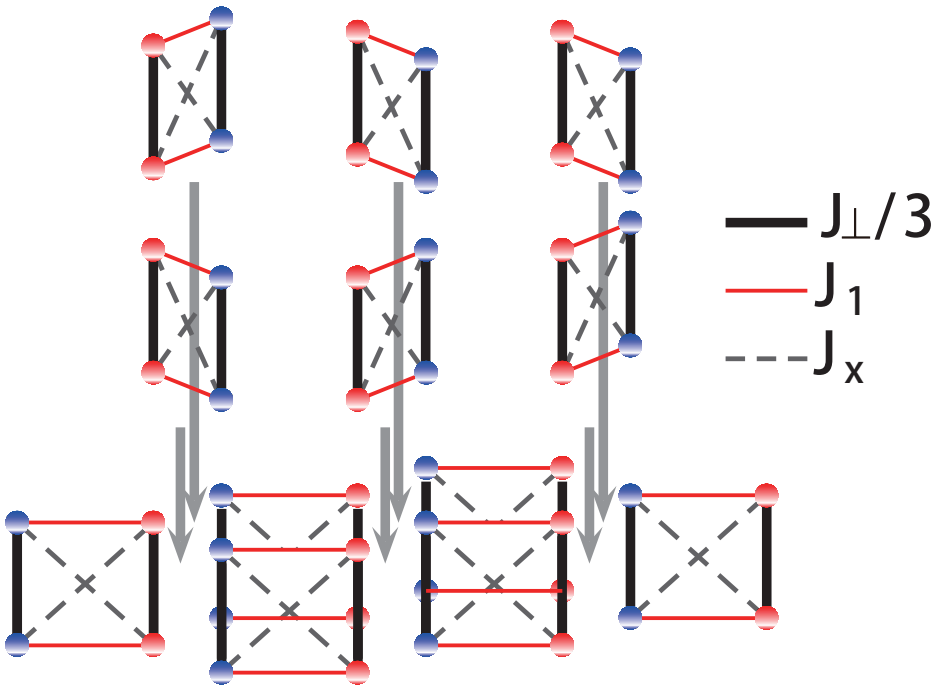


Figure 4.2: Decomposition of the Heisenberg model on the frustrated bilayer honeycomb lattice into three sets of four-spin plaquettes.

As shown in Fig. 4.2, we start by decomposing the Hamiltonian Eq. (4.1) as $H = H_0 + H_1 + H_2$, with

$$\begin{aligned} H_i = \sum_{\mathbf{r}} \Big[ & \frac{J_\perp}{3} \left( \hat{\mathbf{S}}_{1,A}(\mathbf{r}_i) \cdot \hat{\mathbf{S}}_{2,A}(\mathbf{r}_i) + \hat{\mathbf{S}}_{1,B}(\mathbf{r}) \cdot \hat{\mathbf{S}}_{2,B}(\mathbf{r}) \right) \\ + \; & J_1 \left( \hat{\mathbf{S}}_{1,A}(\mathbf{r}_i) \cdot \hat{\mathbf{S}}_{1,B}(\mathbf{r}) + \hat{\mathbf{S}}_{2,A}(\mathbf{r}_i) \cdot \hat{\mathbf{S}}_{2,B}(\mathbf{r}) \right) \\ + \; & J_x \left( \hat{\mathbf{S}}_{1,A}(\mathbf{r}_i) \cdot \hat{\mathbf{S}}_{2,B}(\mathbf{r}) + \hat{\mathbf{S}}_{2,A}(\mathbf{r}_i) \cdot \hat{\mathbf{S}}_{1,B}(\mathbf{r}) \right) \Big], \end{aligned} \tag{4.2}$$

where $\mathbf{r}_0 = \mathbf{r}$ and $\mathbf{r}_i = \mathbf{r} + \mathbf{e}_i$ $(i = 1, 2)$, being $\mathbf{e}_1$ and $\mathbf{e}_2$ the primitive vectors of the triangular lattice. Introducing the bond spin operators

$$\hat{\mathbf{L}}_\alpha = \hat{\mathbf{S}}_{1,\alpha} + \hat{\mathbf{S}}_{2,\alpha} \qquad \hat{\mathbf{K}}_\alpha = \hat{\mathbf{S}}_{1,\alpha} - \hat{\mathbf{S}}_{2,\alpha}. \tag{4.3}$$

with $\alpha = A, B$, we can rewrite $H_i$ as

$$\begin{aligned} H_i &= -\frac{2}{3} J_\perp N S(S+1) + \sum_{\mathbf{r}} \left\{ \frac{J_\perp}{6} \left( \hat{\mathbf{L}}_A^2(\mathbf{r}_i) + \hat{\mathbf{L}}_B^2(\mathbf{r}) \right) \right. \\ &+ \left( \frac{J_1 + J_x}{2} \right) \left( \hat{\mathbf{L}}_A(\mathbf{r}_i) \cdot \hat{\mathbf{L}}_B(\mathbf{r}) \right) \\ &+ \left. \left( \frac{J_1 - J_x}{2} \right) \left( \hat{\mathbf{K}}_A(\mathbf{r_i}) \cdot \hat{\mathbf{K}}_B(\mathbf{r}) \right) \right\}, \end{aligned} \tag{4.4}$$

where $N$ is the number of unit cells.

The main point of this section is that the last term in the Hamiltonian vanishes for $J_1 = J_x$, and therefore, (i) *each* bond spin $\hat{\mathbf{L}}_\alpha^2(\mathbf{r})$ is conserved and (ii) the *total* bond spin $\sum_{\mathbf{r}} \hat{\mathbf{L}}_\alpha^2(\mathbf{r})$ is conserved. Therefore, at $J_1 = J_x$, the eigenstates of $H$ are multiplets of the total bond spin. Among those is the *product state of bond singlets*, i.e.

$$|\psi\rangle = \bigotimes_{i=1}^{N} |s_A\rangle_{\mathbf{r}_i} |s_B\rangle_{\mathbf{r}_i} \tag{4.5}$$

with $\hat{\mathbf{L}}_\alpha(\mathbf{r}_i)|s_\alpha\rangle_{\mathbf{r}_i} = 0$, and $|s_\alpha\rangle_{\mathbf{r}_i} = \sum_{m=-S}^{S} (-1)^{S-m} |m, -m\rangle / \sqrt{2S+1}$. Here $|m, -m\rangle$ labels a product of eigenstates of $\hat{\mathbf{S}}_{1,\alpha}^z(\mathbf{r}_i)$ and $\hat{\mathbf{S}}_{2,\alpha}^z(\mathbf{r}_i)$ on dimer $\alpha$ of the unit cell located at $\mathbf{r}_i$. The energy $E_0$ of $|\psi\rangle$ can be read off from Eq. (4.4), namely $E_0 = -\frac{2}{3} J_\perp N S(S+1)$.

For any other multiplets of the *total* bond spin one has to promote dimers into eigenstates of $\hat{\mathbf{L}}_\alpha^2(\mathbf{r})$ different from zero. This will increase any eigenstate's energy proportional to $J_\perp$, due to the first term under sum in Eq. (4.4), but will also lead to exchange-lowering of the energy proportional to $J_1 + J_x$ from pairs of nearest neighbor dimers with non-zero bond spin due to the second term under sum in Eq. (4.4). Therefore, for any finite site spin $S$, and for $J_1$ less than a critical coupling $0 < J_1 < J_1^c$, $|\psi\rangle$ is indeed also the ground state at $J_1 = J_x$.

While we emphasize, that the preceding argument is valid for *any* site spin $S$, the nature of the state for $J_1 > J_1^c$ at $J_1 = J_x$ may depend on details. However, for $S = 1/2$ the situation is definite. Since there are only

four eigenstates of $\hat{\mathbf{L}}_\alpha^2(\mathbf{r})$, i.e. singlet and triplet, the ground state will either be $|\psi\rangle$ or stem from the sector of *all* $\hat{\mathbf{L}}_\alpha(\mathbf{r})$ in triplet states $|t_{\mu\alpha}\rangle_{\mathbf{r}}$, where $\mu$ refers to the z-component [146]. By virtue of Eq. (4.4) the latter sector is isomorphic to the spin-1 Heisenberg model on the hexagonal lattice. In both of these sectors nucleation of inhomogeneous distributions of $L = 0$ and $L = 1$ are energetically unfavorable, i.e. do not lead to ground states [146].

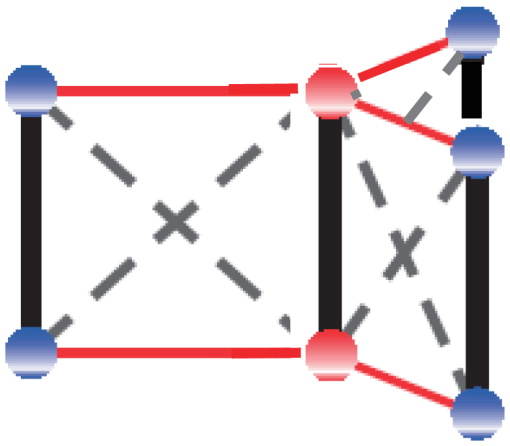

Figure 4.3: The 8-site cluster used in the exact diagonalization for the comment on the region of the exact dimer-product ground state.

In the following we would like to comment on the region of the exact dimer-product ground state. As we know, the dimer-product state is an eigenstate of the Hamiltonian at $J_1 = J_x$. Now the question is whether this state is the true lowest-energy eigenstate or not. From Anderson's argument [147], we can get the lower bound for the ground state energy of the whole system just by adding the lowest energies of the cluster systems. The exact diagonalization of an 8-site cluster (consisting of 4 dimer units) found that the dimer-product state saturates the lower bound if $J_1/J_\perp < 1/2$. The 8-site cluster is shown in Fig. 4.3. Although this does not necessarily mean that the transition occurs precisely at $J_1/J_\perp = 1/2$, it indicates that the dimer-product state is the ground state of the system at least for $J_1/J_\perp < 1/2$ at $J_1 = J_x$.

The exact dimer singlet product state serves as a convenient starting point for several perturbative and mean field methods, which we will take advantage of starting in Sec. 4.5.

## 4.2 Qualitative aspects

Before presenting results of the Schwinger boson and related approaches, we provide in this section a *schematic* quantum phase diagram expected for the bilayer model with interlayer frustration. This is depicted in Fig. 4.4. We will justify this in the following sections by analyzing various phases. We study ground-state energies, low-energy excitations, triplet gaps, order parameters and spin correlations by means of several methods: Schwinger boson and bond operator mean-field theories, exact diagonalization, series expansion and linear spin-wave theory. The results presented in this chapter by other methods which supplement my results were obtained by the following colleagues: exact diagonalization was mainly performed by C. A. Lamas [106], and series expansion was mainly performed by M. Arlego and W. Brenig [106].

Several comments apply to Fig. 4.4. First, the diagram is symmetric respect to the $J_1 = J_x$ line. This is evident at the Hamiltonian level. Indeed, from Fig. 4.1, we see that exchanging $J_1 \leftrightarrow J_x$, induces a site exchange $1, B \leftrightarrow 2, B$, which in turn results in $K_B \leftrightarrow -K_B$. This leaves the last term of $H_0$ in Eq.(4.4) invariant. The same is true for $H_1$ and $H_2$. In the following we normalize energies in units of $J_\perp$ and introduce the dimensionless couplings $J_\perp = 1$, $j_1 = J_1/J_\perp$ and $j_x = J_x/J_\perp$.

The bold dark-red part of the diagonal line of maximum frustration, $j_1 = j_x$ in Fig. 4.4, refers to the exact dimer state. As discussed in Sec. 4.1 this state changes at a first order transition point into the ground state of an $S = 1$ AFM Heisenberg on the single layer hexagonal lattice, which extends over the solid black diagonal line shown in Fig. 4.4. We will show that this transition occurs at $j_1 = j_x \simeq 0.5$.

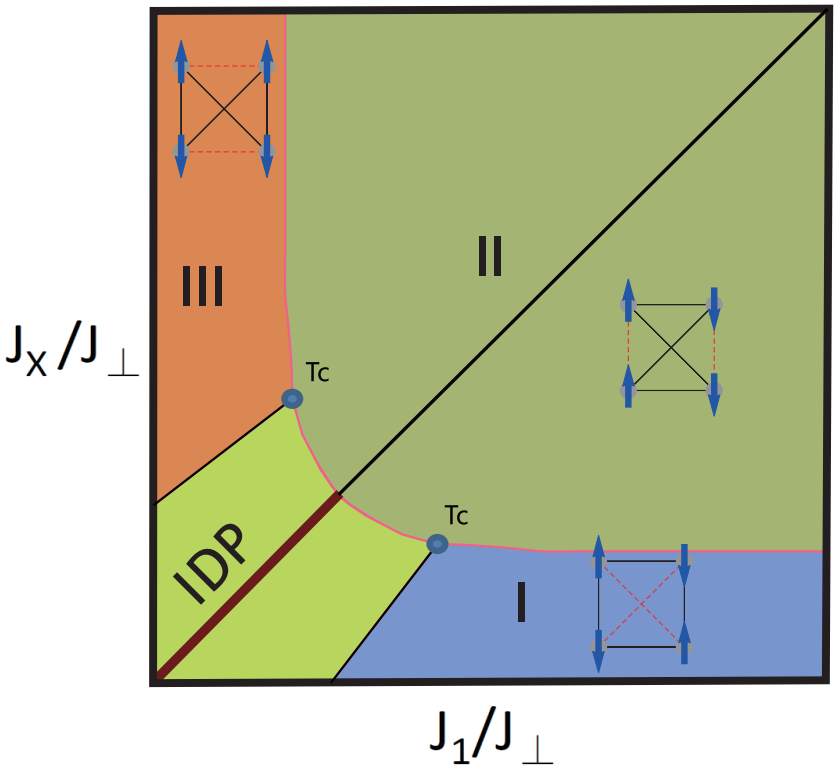


Figure 4.4: Schematic ground state phase diagram of the Heisenberg model on the bilayer honeycomb lattice with interlayer frustration. The blue, olive and orange regions correspond to three collinear magnetic long-range ordered phases labeled as I, II and III. The green region is the quantum disordered *interlayer dimer phase* (IDP). Among phase boundaries, the pink line corresponds to first order transition and the black lines correspond to continuous transition. Tc is a tricritical point.

Departing off the line of maximum frustration the exact dimer turns into a gapped *interlayer dimer phase* (IDP) (see Fig. 4.4). This phase is quantum disordered, and has gapful triplon excitations. The triplon gap ($\Delta$) decreases from $\Delta = 1$ as distance increases from the diagonal line.

For sufficiently large $j_1$ and/or $j_x$, the system favors collinear orders as a straightforward semi-classical argument predicts. Namely three ways exist to minimize two out of the three exchange interactions ($J_1, J_x, J_\perp$) of spins, leaving one of them frustrated. The corresponding phases are labeled I, II, and III in Fig. 4.4, and the frustrated link in spin configuration is marked by

red dash line. Phases I and III are related to each other through the $j_1 \leftrightarrow j_x$ symmetry already mentioned. While the classical states I, II and III are not eigenstates of the quantum Hamiltonian, we detect signals of these orderings in the quantum model by calculating the spin correlation functions, which justify this identification.

We end this section with predicting the order of the phase transitions. Since the symmetries of the phases I, II, and III have no subgroup relations, we expect that the transitions I-II and II-III should be first order, i.e., of level-crossing type. On the other hand, the transition from the IDP into the magnetic phases I and III will be signaled by closing of spin gap $\Delta$, which decreases symmetrically from 1 to 0, away from the red line of exact-dimer product state up to the two corresponding critical lines. This gap closing manifests a second order quantum phase transition.

Finally, as discussed in Sec. 4.1, the transition to the phase II at the end of the bold dark-red line in the IDP is of the first order. The nature of the transition remains first order all along the IDP-II boundary up to the two tricritical points ($T_{\mathrm{C}}$), where the IDP and the phase II meet either the phase I or III.

## 4.3 Schwinger boson mean-field approach for the bilayer model with interlayer frustration

Now we present the formulation of Schwinger boson mean-field approach which we will use in this chapter. We represent the spin operators at each lattice site by two types of Schwinger bosons with a local constraint of the number of Schwinger bosons per site to fix the magnitude of the spin, and introduce two types of bond operators as we have done in Chapter 2. In the following, $\hat{A}^{l}_{\mathbf{R},\mathbf{R}+\delta}$ and $\hat{B}^{l}_{\mathbf{R},\mathbf{R}+\delta}$ correspond to two types of bond operators within the two layers. $\hat{A}^{12(21)}_{\mathbf{R},\mathbf{R}+\delta} = \frac{1}{2}\left(\hat{b}^{1(2)}_{\mathbf{R}\uparrow}\hat{b}^{2(1)}_{\mathbf{R}+\delta\downarrow} - \hat{b}^{1(2)}_{\mathbf{R}\downarrow}\hat{b}^{2(1)}_{\mathbf{R}+\delta\uparrow}\right)$ and $\hat{B}^{12(21)}_{\mathbf{R},\mathbf{R}+\delta} = \frac{1}{2}\left(\hat{b}^{1(2)\dagger}_{\mathbf{R}\uparrow}\hat{b}^{2(1)}_{\mathbf{R}+\delta\uparrow} + \hat{b}^{1(2)\dagger}_{\mathbf{R}\downarrow}\hat{b}^{2(1)}_{\mathbf{R}+\delta\downarrow}\right)$ correspond to two types of bond oper-

ators between the two layers. Therefore, we can decompose the Hamiltonian as

$$\begin{aligned}
\hat{H} &= J_1 \sum_{\mathbf{r}^{(1)},lm} \left( :\hat{B}^{l\dagger}_{\mathbf{r}^{(1)},\mathbf{r}^{(1)}+\alpha_m} \hat{B}^{l}_{\mathbf{r}^{(1)},\mathbf{r}^{(1)}+\alpha_m} : - \hat{A}^{l\dagger}_{\mathbf{r}^{(1)},\mathbf{r}^{(1)}+\alpha_m} \hat{A}^{l}_{\mathbf{r}^{(1)},\mathbf{r}^{(1)}+\alpha_m} \right) \\
&\quad + J_\perp \sum_n \sum_{\mathbf{r}^{(n)}} \left( :\hat{B}^{12\dagger}_{\mathbf{r}^{(n)},\mathbf{r}^{(n)}} \hat{B}^{12}_{\mathbf{r}^{(n)},\mathbf{r}^{(n)}} : - \hat{A}^{12\dagger}_{\mathbf{r}^{(n)},\mathbf{r}^{(n)}} \hat{A}^{12}_{\mathbf{r}^{(n)},\mathbf{r}^{(n)}} \right) \\
&\quad + J_x \sum_{\mathbf{r}^{(1)},m} \Big( :\hat{B}^{12\dagger}_{\mathbf{r}^{(1)},\mathbf{r}^{(1)}+\alpha_m} \hat{B}^{12}_{\mathbf{r}^{(1)},\mathbf{r}^{(1)}+\alpha_m} : - \hat{A}^{12\dagger}_{\mathbf{r}^{(1)},\mathbf{r}^{(1)}+\alpha_m} \hat{A}^{12}_{\mathbf{r}^{(1)},\mathbf{r}^{(1)}+\alpha_m} \\
&\quad + :\hat{B}^{21\dagger}_{\mathbf{r}^{(1)},\mathbf{r}^{(1)}+\alpha_m} \hat{B}^{21}_{\mathbf{r}^{(1)},\mathbf{r}^{(1)}+\alpha_m} : - \hat{A}^{21\dagger}_{\mathbf{r}^{(1)},\mathbf{r}^{(1)}+\alpha_m} \hat{A}^{21}_{\mathbf{r}^{(1)},\mathbf{r}^{(1)}+\alpha_m} \Big) . \qquad (4.6)
\end{aligned}$$

Here $\mathbf{r}^{(n)}$ are the positions of lattice sites of sublattice $n$ ($n = 1, 2$). $\alpha_m$ are the nearest neighbor vectors and $\beta_m$ are three of the next nearest neighbor vectors as we have chosen in Chapter 2, with $m = 1, 2, 3$ for the directions of bonds. Then we introduce mean fields corresponding to these bond operators. We assume that they are uniform in space, but dependent on the directions of bonds:

$$\begin{aligned}
A^l_m &\equiv \left\langle \hat{A}^{l}_{\mathbf{r}^{(1)},\mathbf{r}^{(1)}+\alpha_m} \right\rangle , \qquad B^l_m \equiv \left\langle \hat{B}^{l}_{\mathbf{r}^{(1)},\mathbf{r}^{(1)}+\alpha_m} \right\rangle , \\
A^{\perp(n)} &\equiv \left\langle \hat{A}^{12}_{\mathbf{r}^{(n)},\mathbf{r}^{(n)}} \right\rangle , \qquad B^{\perp(n)} \equiv \left\langle \hat{B}^{12}_{\mathbf{r}^{(n)},\mathbf{r}^{(n)}} \right\rangle , \qquad (4.7) \\
A^{12(21)}_m &\equiv \left\langle \hat{A}^{12(21)}_{\mathbf{r}^{(n)},\mathbf{r}^{(n)}+\alpha_m} \right\rangle , \qquad B^{12(21)}_m \equiv \left\langle \hat{B}^{12(21)}_{\mathbf{r}^{(n)},\mathbf{r}^{(n)}+\alpha_m} \right\rangle .
\end{aligned}$$

By using the Hartree-Fock decoupling, we obtain the mean-field Hamiltonian:

$$\begin{aligned}
\hat{H}_{MF} &= J_1 \sum_{\mathbf{r}^{(1)},lm} \Big[ \left( B^{l*}_m \hat{B}^{l}_{\mathbf{r}^{(1)},\mathbf{r}^{(1)}+\alpha_m} - A^{l*}_m \hat{A}^{l}_{\mathbf{r}^{(1)},\mathbf{r}^{(1)}+\alpha_m} \right) + h.c. \\
&\quad - \left( \left| B^l_m \right|^2 - \left| A^l_m \right|^2 \right) \Big] \\
&\quad + J_\perp \sum_n \sum_{\mathbf{r}^{(n)}} \Big[ \left( B^{\perp(n)*} \hat{B}^{12}_{\mathbf{r}^{(n)},\mathbf{r}^{(n)}} - A^{\perp(n)*} \hat{A}^{12}_{\mathbf{r}^{(n)},\mathbf{r}^{(n)}} \right) + h.c. \\
&\quad - \left( \left| B^{\perp(n)} \right|^2 - \left| A^{\perp(n)} \right|^2 \right) \Big]
\end{aligned}$$

$$
\begin{aligned}
&+J_x \sum_{\mathbf{r}^{(1)},m} \Big[ \Big( B_m^{12*} \hat{B}^{12}_{\mathbf{r}^{(n)},\mathbf{r}^{(n)}+\alpha_m} - A_m^{12*} \hat{A}^{12}_{\mathbf{r}^{(n)},\mathbf{r}^{(n)}+\alpha_m} \Big) + h.c. \\
&- \Big( B_m^{21*} \hat{B}^{21}_{\mathbf{r}^{(n)},\mathbf{r}^{(n)}+\alpha_m} - A_m^{21*} \hat{A}^{21}_{\mathbf{r}^{(n)},\mathbf{r}^{(n)}+\alpha_m} \Big) + h.c. \\
&- \Big( \left|B_m^{12}\right|^2 + \left|B_m^{21}\right|^2 - \left|A_m^{12}\right|^2 - \left|A_m^{21}\right|^2 \Big) \Big] . \qquad (4.8)
\end{aligned}
$$

As we have done in Chapter 2, the local constraint of the number of Schwinger bosons per site is enforced by a Lagrange multiplier $\lambda_{\mathbf{R}}$ at each site. We replace the local Lagrange multipliers $\lambda_{\mathbf{R}}$ by parameters $\lambda^{(n)}$ for each sublattice, which is a crucial approximation in Schwinger bosons mean-field theory:

$$
\hat{H}_{MF} \rightarrow \hat{H}_{MF} + \hat{H}_{\lambda} \qquad (4.9)
$$

with

$$
\hat{H}_{\lambda} = \sum_{n=1,2} \sum_{\mathbf{r}^{(n)},l=1,2} \lambda^{l(n)} \left( \sum_{\mu=\uparrow,\downarrow} \hat{b}^{l\dagger}_{\mathbf{r}^{(n)}\mu} \hat{b}^{l}_{\mathbf{r}^{(n)}\mu} - 2S \right) . \qquad (4.10)
$$

We perform Fourier transformation for Schwinger bosons on each sublattice:

$$
\hat{b}^{l}_{\mathbf{r}^{(n)}\mu} = \frac{1}{\sqrt{N/2}} \sum_{\mathbf{k}\in BZ} \hat{b}^{l(n)}_{\mathbf{k}\mu} \exp\left( i\mathbf{k}\cdot\mathbf{r}^{(n)} \right) , \qquad (4.11)
$$

where $N$ is the total number of lattice sites in one layer. In the following we will assume the mean fields $A$ and $B$ to be real. In the $\mathbf{k}$-space, the mean-field Hamiltonian can be represented in the following compact form:

$$
\hat{H}_{MF} = \sum_{\mathbf{k}\in BZ} \hat{\phi}^{\dagger}_{\mathbf{k}} \tilde{M}_{\mathbf{k}} \hat{\phi}_{\mathbf{k}} + E_0, \qquad (4.12)
$$

where we introduce the Nambu spinor in the momentum space:

$$
\hat{\phi}_{\mathbf{k}} = \left( \begin{array}{cccccccc} \hat{b}^{1(1)}_{\mathbf{k}\uparrow}, & \hat{b}^{1(2)}_{\mathbf{k}\uparrow}, & \hat{b}^{2(1)}_{\mathbf{k}\uparrow}, & \hat{b}^{2(2)}_{\mathbf{k}\uparrow}, & \hat{b}^{1(1)\dagger}_{-\mathbf{k}\downarrow}, & \hat{b}^{1(2)\dagger}_{-\mathbf{k}\downarrow}, & \hat{b}^{2(1)\dagger}_{-\mathbf{k}\downarrow}, & \hat{b}^{2(2)\dagger}_{-\mathbf{k}\downarrow} \end{array} \right)^{\mathsf{T}} , \qquad (4.13)
$$

and the constant is as follows:

$$
-E_0 \;=\; \frac{N}{2} J_1 \sum_{lm} \Big( \left(B_m^l\right)^2 - \left(A_m^l\right)^2 \Big) + \frac{N}{2} J_{\perp} \sum_{n} \Big( \left(B^{\perp(n)}\right)^2 - \left(A^{\perp(n)}\right)^2 \Big)
$$

$$+\frac{N}{2}J_x\sum_m\left(\left(B_m^{12}\right)^2+\left(B_m^{21}\right)^2-\left(A_m^{12}\right)^2-\left(A_m^{21}\right)^2\right)$$
$$+(2S+1)\,\frac{N}{2}\sum_{ln}\lambda^{l(n)}. \tag{4.14}$$

The $8\times 8$ dynamical matrix $\tilde{M}_{\mathbf{k}}$ is given by

$$\tilde{M}_{\mathbf{k}}=\begin{pmatrix} M_{\mathbf{k}}^B & -M_{\mathbf{k}}^A \\ M_{\mathbf{k}}^A & M_{\mathbf{k}}^B \end{pmatrix}, \tag{4.15}$$

where

$$M_{\mathbf{k}}^B=\begin{pmatrix} \Gamma_{\mathbf{k}}^{B1}+\Lambda^1 & \Gamma^{B\perp} \\ \left(\Gamma^{B\perp}\right)^\dagger & \Gamma_{\mathbf{k}}^{B2}+\Lambda^2 \end{pmatrix},\quad M_{\mathbf{k}}^A=\begin{pmatrix} \Gamma_{\mathbf{k}}^{A1} & \Gamma^{A\perp} \\ -\left(\Gamma^{A\perp}\right)^\dagger & \Gamma_{\mathbf{k}}^{A2} \end{pmatrix} \tag{4.16}$$

with the following definitions of matrices:

$$\Lambda^l = \begin{pmatrix} \lambda^{l(1)} & 0 \\ 0 & \lambda^{l(2)} \end{pmatrix}, \tag{4.17}$$

$$\Gamma_{\mathbf{k}}^{Bl} = \begin{pmatrix} 0 & \frac{J_1}{2}\sum_m B_m^l e^{i\mathbf{k}\cdot\alpha_m} \\ \frac{J_1}{2}\sum_m B_m^l e^{-i\mathbf{k}\cdot\alpha_m} & 0 \end{pmatrix}, \tag{4.18}$$

$$\Gamma_{\mathbf{k}}^{Al} = \begin{pmatrix} 0 & \frac{J_1}{2}\sum_m A_m^l e^{i\mathbf{k}\cdot\alpha_m} \\ -\frac{J_1}{2}\sum_m A_m^l e^{-i\mathbf{k}\cdot\alpha_m} & 0 \end{pmatrix}, \tag{4.19}$$

$$\Gamma^{B\perp} = \begin{pmatrix} \frac{J_\perp}{2}B^{\perp(1)} & \frac{J_x}{2}\sum_m B_m^{12} e^{i\mathbf{k}\cdot\alpha_m} \\ \frac{J_x}{2}\sum_m B_m^{21} e^{-i\mathbf{k}\cdot\alpha_m} & \frac{J_\perp}{2}B^{\perp(2)} \end{pmatrix}, \tag{4.20}$$

$$\Gamma^{A\perp} = \begin{pmatrix} \frac{J_\perp}{2}A^{\perp(1)} & \frac{J_x}{2}\sum_m A_m^{12} e^{i\mathbf{k}\cdot\alpha_m} \\ -\frac{J_x}{2}\sum_m A_m^{21} e^{-i\mathbf{k}\cdot\alpha_m} & \frac{J_\perp}{2}A^{\perp(2)} \end{pmatrix}. \tag{4.21}$$

As we have done in Chapter 2, para-unitary diagonalization [114] of $\tilde{M}_{\mathbf{k}}$ can be achieved by defining the new boson operators $\hat{\phi}_{\mathbf{k}} = F_{\mathbf{k}}\hat{\psi}_{\mathbf{k}}$, where $F_{\mathbf{k}}$ satisfies

$$F_{\mathbf{k}}^{\dagger}\varphi F_{\mathbf{k}} = \varphi, \quad \varphi = \begin{pmatrix} I_{4\times 4} & 0 \\ 0 & -I_{4\times 4} \end{pmatrix}. \tag{4.22}$$

Therefore, the mean-field Hamiltonian is diagonalized as follows:

$$\hat{H}_{MF} = \sum_{\mathbf{k}} \hat{\psi}_{\mathbf{k}}^{\dagger} \cdot \mathbf{E}(\mathbf{k}) \cdot \hat{\psi}_{\mathbf{k}} + E_0, \tag{4.23}$$

where

$$\mathbf{E}(\mathbf{k}) = \mathrm{diag}\left[\omega_1(\mathbf{k}), \omega_2(\mathbf{k}), \omega_3(\mathbf{k}), \omega_4(\mathbf{k}), \omega_1(\mathbf{k}), \omega_2(\mathbf{k}), \omega_3(\mathbf{k}), \omega_4(\mathbf{k})\right]. \tag{4.24}$$

On the other hand, from the inverse of the Bogoliubov transformation matrix [114]

$$F_{\mathbf{k}} = \begin{pmatrix} U_{\mathbf{k}} & -V_{\mathbf{k}} \\ V_{\mathbf{k}} & U_{\mathbf{k}} \end{pmatrix}, \tag{4.25}$$

we can establish the mean-field equations by calculating the expectation values of corresponding operators directly:

$$\begin{aligned} A_m^l &= \frac{1}{2} \times \frac{2}{N} \sum_{\mathbf{k},\mathbf{k}'} e^{\left[i\mathbf{k}\cdot\mathbf{r}^{(1)} + i\mathbf{k}'\cdot\left(\mathbf{r}^{(1)}+\alpha_m\right)\right]} \left(\left\langle \hat{b}_{\mathbf{k}\uparrow}^{l(1)} \hat{b}_{\mathbf{k}'\downarrow}^{l(2)} \right\rangle - \left\langle \hat{b}_{\mathbf{k}\downarrow}^{l(1)} \hat{b}_{\mathbf{k}'\uparrow}^{l(2)} \right\rangle\right) \\ &= \frac{1}{N} \sum_{\mathbf{k}} \left[\left(U_{\mathbf{k}} V_{\mathbf{k}}^{\dagger}\right)_{2l-1,2l} e^{-i\mathbf{k}\cdot\alpha_m} + c.c.\right], \end{aligned} \tag{4.26}$$

$$\begin{aligned} A^{\perp(n)} &= \frac{1}{2} \times \frac{2}{N} \sum_{\mathbf{k},\mathbf{k}'} e^{i\left(\mathbf{k}+\mathbf{k}'\right)\cdot\mathbf{r}^{(n)}} \left(\left\langle \hat{b}_{\mathbf{k}\uparrow}^{1(n)} \hat{b}_{\mathbf{k}'\downarrow}^{2(n)} \right\rangle - \left\langle \hat{b}_{\mathbf{k}\downarrow}^{1(n)} \hat{b}_{\mathbf{k}'\uparrow}^{2(n)} \right\rangle\right) \\ &= \frac{1}{N} \sum_{\mathbf{k}} \left[\left(U_{\mathbf{k}} V_{\mathbf{k}}^{\dagger}\right)_{n,n+2} + c.c.\right], \end{aligned} \tag{4.27}$$

$$A_m^{12} = \frac{1}{2} \times \frac{2}{N} \sum_{\mathbf{k},\mathbf{k}'} e^{\left[i\mathbf{k}\cdot\mathbf{r}^{(1)} + i\mathbf{k}'\cdot\left(\mathbf{r}^{(1)}+\alpha_m\right)\right]} \left(\left\langle \hat{b}_{\mathbf{k}\uparrow}^{1(1)} \hat{b}_{\mathbf{k}'\downarrow}^{2(2)} \right\rangle - \left\langle \hat{b}_{\mathbf{k}\downarrow}^{1(1)} \hat{b}_{\mathbf{k}'\uparrow}^{2(2)} \right\rangle\right)$$

$$= \frac{1}{N}\sum_{\mathbf{k}}\left[\left(U_{\mathbf{k}}V_{\mathbf{k}}^{\dagger}\right)_{14}e^{-i\mathbf{k}\cdot\alpha_m}+c.c.\right], \tag{4.28}$$

$$\begin{aligned} A_m^{21} &= \frac{1}{2}\times\frac{2}{N}\sum_{\mathbf{k},\mathbf{k}'}e^{\left[i\mathbf{k}\cdot\mathbf{r}^{(1)}+i\mathbf{k}'\cdot\left(\mathbf{r}^{(1)}+\alpha_m\right)\right]}\left(\left\langle\hat{b}_{\mathbf{k}\uparrow}^{2(1)}\hat{b}_{\mathbf{k}'\downarrow}^{1(2)}\right\rangle-\left\langle\hat{b}_{\mathbf{k}\downarrow}^{2(1)}\hat{b}_{\mathbf{k}'\uparrow}^{1(2)}\right\rangle\right) \\ &= \frac{1}{N}\sum_{\mathbf{k}}\left[\left(U_{\mathbf{k}}V_{\mathbf{k}}^{\dagger}\right)_{32}e^{-i\mathbf{k}\cdot\alpha_m}+c.c.\right], \end{aligned} \tag{4.29}$$

$$\begin{aligned} B_m^{l} &= \frac{1}{2}\times\frac{2}{N}\sum_{\mathbf{k},\mathbf{k}'}e^{\left[-i\mathbf{k}\cdot\mathbf{r}^{(1)}+i\mathbf{k}'\cdot\left(\mathbf{r}^{(1)}+\alpha_m\right)\right]}\left(\left\langle\hat{b}_{\mathbf{k}\uparrow}^{l(1)\dagger}\hat{b}_{\mathbf{k}'\uparrow}^{l(2)}\right\rangle+\left\langle\hat{b}_{\mathbf{k}\downarrow}^{l(1)\dagger}\hat{b}_{\mathbf{k}'\downarrow}^{l(2)}\right\rangle\right) \\ &= \frac{1}{N}\sum_{\mathbf{k}}\left[\left(V_{\mathbf{k}}V_{\mathbf{k}}^{\dagger}\right)_{2l-1,2l}e^{-i\mathbf{k}\cdot\alpha_m}+c.c.\right], \end{aligned} \tag{4.30}$$

$$\begin{aligned} B^{\perp(n)} &= \frac{1}{2}\times\frac{2}{N}\sum_{\mathbf{k},\mathbf{k}'}e^{i\left(\mathbf{k}'-\mathbf{k}\right)\cdot\mathbf{r}^{(n)}}\left(\left\langle\hat{b}_{\mathbf{k}\uparrow}^{1(n)\dagger}\hat{b}_{\mathbf{k}'\uparrow}^{2(n)}\right\rangle+\left\langle\hat{b}_{\mathbf{k}\downarrow}^{1(n)\dagger}\hat{b}_{\mathbf{k}'\downarrow}^{2(n)}\right\rangle\right) \\ &= \frac{1}{N}\sum_{\mathbf{k}}\left[\left(V_{\mathbf{k}}V_{\mathbf{k}}^{\dagger}\right)_{n,n+2}+c.c.\right], \end{aligned} \tag{4.31}$$

$$\begin{aligned} B_m^{12} &= \frac{1}{2}\times\frac{2}{N}\sum_{\mathbf{k},\mathbf{k}'}e^{\left[-i\mathbf{k}\cdot\mathbf{r}^{(1)}+i\mathbf{k}'\cdot\left(\mathbf{r}^{(1)}+\alpha_m\right)\right]}\left(\left\langle\hat{b}_{\mathbf{k}\uparrow}^{1(1)\dagger}\hat{b}_{\mathbf{k}'\uparrow}^{2(2)}\right\rangle+\left\langle\hat{b}_{\mathbf{k}\downarrow}^{1(1)\dagger}\hat{b}_{\mathbf{k}'\downarrow}^{2(2)}\right\rangle\right) \\ &= \frac{1}{N}\sum_{\mathbf{k}}\left[\left(V_{\mathbf{k}}V_{\mathbf{k}}^{\dagger}\right)_{14}e^{-i\mathbf{k}\cdot\alpha_m}+c.c.\right], \end{aligned} \tag{4.32}$$

$$\begin{aligned} B_m^{21} &= \frac{1}{2}\times\frac{2}{N}\sum_{\mathbf{k},\mathbf{k}'}e^{\left[-i\mathbf{k}\cdot\mathbf{r}^{(1)}+i\mathbf{k}'\cdot\left(\mathbf{r}^{(1)}+\alpha_m\right)\right]}\left(\left\langle\hat{b}_{\mathbf{k}\uparrow}^{2(1)\dagger}\hat{b}_{\mathbf{k}'\uparrow}^{1(2)}\right\rangle+\left\langle\hat{b}_{\mathbf{k}\downarrow}^{2(1)\dagger}\hat{b}_{\mathbf{k}'\downarrow}^{1(2)}\right\rangle\right) \\ &= \frac{1}{N}\sum_{\mathbf{k}}\left[\left(V_{\mathbf{k}}V_{\mathbf{k}}^{\dagger}\right)_{32}e^{-i\mathbf{k}\cdot\alpha_m}+c.c.\right]. \end{aligned} \tag{4.33}$$

The four constraints in the number of Schwinger bosons can be written in

the momentum space as

$$\begin{aligned} 2S &= \frac{2}{N}\sum_{\mathbf{k},\mathbf{k}'} e^{i\left(\mathbf{k}'-\mathbf{k}\right)\cdot\mathbf{r}^{(n)}}\left(\left\langle \hat{b}^{l(n)\dagger}_{\mathbf{k}\uparrow}\hat{b}^{l(n)}_{\mathbf{k}'\uparrow}\right\rangle + \left\langle \hat{b}^{l(n)\dagger}_{\mathbf{k}\downarrow}\hat{b}^{l(n)}_{\mathbf{k}'\downarrow}\right\rangle\right) \\ &= \frac{2}{N}\sum_{\mathbf{k}}\left[\left(V_{\mathbf{k}}V^{\dagger}_{\mathbf{k}}\right)_{\nu\nu} + c.c.\right], \end{aligned} \tag{4.34}$$

where $\nu = 1, 2, 3, 4$. The number of parameters to be determined is 32. Since we have two layers, we have six $A^{l}_{m}$ and six $B^{l}_{m}$ in total. For the interlayer nearest neighbor bond, we have two $A^{\perp(n)}$ and two $B^{\perp(n)}$. For three interlayer second neighbor bonds, we have three $A^{12}_{m}$, three $A^{21}_{m}$, three $B^{12}_{m}$ and three $B^{21}_{m}$. In addition to these 28 mean-field parameters, we also need to determine four Lagrange multipliers, which are chemical potentials of Schwinger bosons.

## 4.4 Bond operator approach

Quantum spin models comprising weakly coupled antiferromagnetic spin-1/2 dimers allow for a description in terms of bosonic operators, so called *bond operators* (BO) [148–150], which label the dimer's singlet-triplet states. BOs lead to a treatment of dimerized phases similar to the linear spin wave theory for magnetically ordered phases. Within BO theory the two spins, $\mathbf{S}_1$ and $\mathbf{S}_2$, on each dimer are expressed as

$$S^{\alpha}_{1} = \frac{1}{2}(s^{\dagger}t_{\alpha} + t^{\dagger}_{\alpha}s - \sum_{\beta,\gamma} i\varepsilon_{\alpha\beta\gamma}t^{\dagger}_{\beta}t_{\gamma}), \tag{4.35}$$

$$S^{\alpha}_{2} = \frac{1}{2}(-s^{\dagger}t_{\alpha} - t^{\dagger}_{\alpha}s - \sum_{\beta,\gamma} i\varepsilon_{\alpha\beta\gamma}t^{\dagger}_{\beta}t_{\gamma}), \tag{4.36}$$

where $s^{(\dagger)}$and $t^{(\dagger)}_{\alpha}$ destroy(create) the singlet and triplet states of the dimer and Greek indices, $\alpha = 1, 2, 3$, label to the threefold triplet states. A hard-core constraint

$$s^{\dagger}s + \sum_{\alpha} t^{\dagger}_{\alpha}t_{\alpha} = 1 \tag{4.37}$$

is implied, which renders the algebra of the r.h.s of Eqs. (4.35) and (4.36) identical to that of spins.

Inserting the BO representation into the spin model leads to an interacting Bose system. Two kinds of *quadratic approximations* have been used in the limit of weak dimer coupling, namely the BO mean-field theory (BO-MFT) [148] and the BO Holstein-Primakoff (BO-HP) approach [149, 150]. In both cases, terms only up to the second order in the BOs are retained. In the BO-MFT, singlets are condensed and this is represented by replacing the operators $s$ and $s^\dagger$ by a real constant. The constraint (4.37) is satisfied on the average with a global Lagrange multiplier $\eta$ [148]. In the BO-HP approach, the constraint is used to eliminate all the singlet operators using $s = s^\dagger = (1-\sum_\alpha t_\alpha^\dagger t_\alpha)^{-1/2}$, followed by expanding the square root [149,150].

In both of BO-MFT and BO-HP approaches, the Hamiltonian (4.1) in units of $J_\perp$ on the frustrated hexagonal bilayer lattice is approximated as

$$
\begin{aligned}
H &= H_0 + H_1 + H_c && (4.38)\\
H_0 &= \sum_{l,b}(-\frac{3}{4}s^2 + \frac{1}{4}\sum_\alpha t_{lb\alpha}^\dagger t_{lb\alpha}) && (4.39)\\
H_1 &= \sum_{l,\widetilde{m},\alpha}\frac{s^2\widetilde{j_1}}{2}(t_{\widetilde{m}A\alpha}^\dagger t_{lB\alpha} + t_{\widetilde{m}A\alpha}^\dagger t_{lB\alpha}^\dagger + h.c.) && (4.40)\\
H_c &= -\sum_{l,b}\eta(s^2 + \sum_\alpha t_{lb\alpha}^\dagger t_{lb\alpha} - 1) && (4.41)
\end{aligned}
$$

where $t_{lb\alpha}^{(\dagger)}$ labels triplets in the unit cell $l$ at the basis site $b = A, B$ of the two interpenetrating triangular lattices comprising the hexagonal lattice. The sites $\widetilde{m}A$ in Eq. (4.40) refer to the three nearest neighbors sites around the B-sublattice site $lB$. $\widetilde{j_1} = j_1 - j_x$ is the dimensionless exchange coupling. $s^2$ is the singlet condensate, and $\eta$ is the global Lagrange multiplier for constraint (4.37).

This Hamiltonian can be diagonalized by a standard Bogoliubov transformation and this leads to ground state energy *E per unit cell*, i.e. per four

spins,

$$E = -\frac{3}{4} - \frac{3}{2}s^2 - 2\eta s^2 + 5\eta + \frac{3}{2N}\sum_k (E_{k+} + E_{k-}) \tag{4.42}$$

with the *triplon dispersion*

$$E_{k\pm} = a\sqrt{1 \pm \frac{s^2}{a}e(k)} \tag{4.43}$$

where $a = 1/4 - \eta$, and

$$e(k) = \widetilde{j}_1 \sqrt{3 + 2\cos k_x + 4\cos\frac{k_x}{2}\cos\frac{\sqrt{3}k_y}{2}} \tag{4.44}$$

$$= \widetilde{j}_1 \sqrt{3 + g(k)}, \tag{4.45}$$

with $g(k) \equiv 2\cos k_x + 4\cos\frac{k_x}{2}\cos\frac{\sqrt{3}k_y}{2}$. Eqs. (4.43)-(4.45) display an important symmetry for $\widetilde{j}_1 \leftrightarrow -\widetilde{j}_1$, namely for that $e(k) \leftrightarrow -e(k)$. This implies that on the quadratic level of the BO-HP and BO-MFT approaches all results are symmetric with respect to the diagonal line of $j_1 = j_x$. From Eqs. (4.42)-(4.45) the BO-HP approach is completed by replacing the sum of the first four terms in Eq. (4.42) by $-9/2$ and by setting $a = 1$, $s = 1$ in Eqs. (4.43) and (4.44).

For the BO-MFT the energy $E$ has to be extremized, implying two self-consistency equations $\partial E/\partial a = 0$ and $\partial E/\partial s = 0$. These equations can be combined into a single one for the parameter $d = s^2/a$, i.e.

$$d = \frac{5}{2} - \frac{3}{4N}\sum_{k,v=\pm}\frac{1}{\sqrt{1 + v\,d\,e(k)}}\,. \tag{4.46}$$

Knowing $d$, we can obtain both mean field parameters by inserting it in one of the mean field equations, e.g. $\partial E/\partial a = 0$

$$2s^2 = 5 - \frac{3}{2N}\sum_{k,v=\pm}\frac{1 + \frac{1}{2}\,v\,d\,e(k)}{\sqrt{1 + v\,d\,e(k)}}\,. \tag{4.47}$$

We mention in passing that the trivial limit, i.e. $\widetilde{j}_1 = 0$, leads to $d = 1$,

$s = 1$, and $\eta = -3/4$, and therefore the *singlet-triplet gap* is $\Delta = 1$ and the ground state energy is $E = -3/2$, which is consistent with two singlet dimers per unit cell.

## 4.5 Interlayer dimer phase

In this section we analyze the interlayer dimer phase (IDP) at $j_1, j_x \ll 1$. In particular, we discuss the ground state energy and the spin gap, as obtained from dimer series expansion (D-SE), bond operator (BO) theory using Holstein-Primakoff (HP) approach and mean-field theory (MFT), as well as from exact diagonalization (ED). The technical details about the D-SE calculation can be found in Ref. [143, 151–158]. Both D-SE and BO-HP/MFT are natural approaches to treat the IDP, since they are exact in the fully decoupled dimer-product state along the line $j_1 = j_x$ and treat deviations from that line perturbatively. While D-SE is exact order-by-order in $j_1 - j_x$, BO-HP/MFT is proper only up to the leading order. Since both approaches renormalize only the fully decoupled dimer-product state, they are insensitive to level crossing, which may occur within the ground state, as a function of $j_1 - j_x$. This means that these methods do not detect a first order transition, but only second order quantum phase transitions accompanied by closing spin gap. Therefore, in order to probe first order transitions, we resort to ED as an unbiased technique. While finite size effects render ED less effective to detect gap closing, it allows to search for level crossings rather efficiently. In contrast, ED, BO, and D-SE are complementary and useful to determine the extent of IDP phase, as well as examine the nature of the transitions to other phases.

We begin by considering the ground state energy. From the D-SE calculation, we obtain the fourth order expansion in $j_1$ and $j_x$ for the ground state energy *per spin* evolving from the limit of decoupled interlayer dimers

$$\begin{aligned} E(j_1, j_x) &= -\frac{3}{8} + \frac{9}{512}(j_1 - j_x)^2 \Big[ -16 - 8(j_1 + j_x) \\ &\quad +3\left(j_1^2 + j_x^2\right) - 22 j_1 j_x \Big]. \end{aligned} \tag{4.48}$$

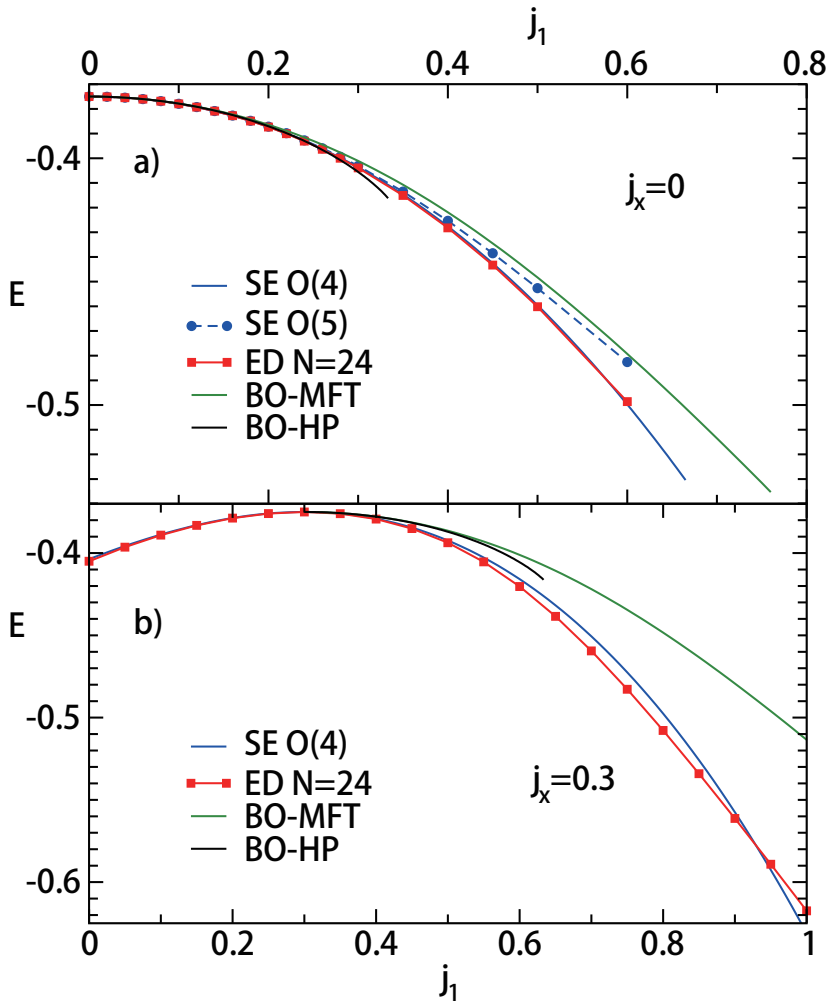


Figure 4.5: Ground state energy per spin $E$ as a function of $j_1$ from ED (red with squares), D-SE (blue, blue dashed with circles), BO-HP (black) and BO-MFT (green) for a) $j_x = 0$ with system size $N = 24$, and the fourth and fifth orders, see also Refs. [90, 159] and b) $j_x = 0.3$ with system size $N = 24$, and the fourth order.

This gives $E(j_1, j_1) = -\frac{3}{8}$, corresponding the exact dimer-product solution along $j_x = j_1$ and $E(j_1, j_x) = E(j_x, j_1)$ fulfilling the symmetry under $j_1 \leftrightarrow j_x$. In Fig. 4.5 we compare the ground state energy obtained from the various methods for two different values of $j_x$. Fig. 4.5a) also contains the BO-MFT

results taken from Refs. [159] and results in Ref. [90] of the fifth order results of D-SE at $j_x = 0$, and ED for $N = 24$ sites. In both panels, the energy shows a maximum for all methods at $j_1 = j_x$, where the ground state is a dimer-product state with energy per spin equal to $-3/8$. Around the exact solution point, ED and D-SE show excellent agreement up to $|j_1 - j_x| \simeq 0.3$ in both panels of Fig. 4.5. Deviations between ED and D-SE beyond that points are due to finite size effects in the ED and due to the finite order of the D-SE. The effect of the latter can be assessed at $j_x = 0$, where the higher fifth order result is available [90]. From Fig. 4.5a), a difference between the fourth and fifth order D-SE becomes visible for $|j_1 - j_x| \gtrsim 0.3$. Turning to the BO theory, two comments are in order. First, as shown in Fig. 4.7, the HP spin gap becomes zero within the range of $j_1$, $j_x$-values shown. Therefore, the BO-HP curve terminate at $j_1 \simeq 0.33$ in Fig. 4.5a). Second, both HP and MFT depend on $j_1$ and $j_x$ only via the difference $j_1 - j_x$. This is not an exact property of the model beyond the leading order, which is obvious from Eq. (4.48). In turn, BO results in Fig. 4.5a) and b) are identical to each other up to a shift of origin and have been plotted only for positive $j_1 - j_x$. Moreover, ED, D-SE and BO are expected to agree best at either $j_1 = 0$ or $j_x = 0$, which is consistent with this figure. In fact, the agreement between all four methods is excellent for $j_x = 0$ and for $j_1 \lesssim 0.3$, while the ED and D-SE show some difference from the BO theory at $j_x = 0.3$. In view of the significant changes from the fourth to fifth order D-SE, a quantitative assessment of these differences is beyond this work. In fact, Fig. 4.5a) suggests that the fifth order D-SE agrees better with the BO theory than with the ED for $j_1 \gtrsim 0.3$.

While the difference in the results between the various methods discussed are only quantitative, we expect a qualitative difference between the ED and D-SE or BO theory in the vicinity of the first order transition from the IDP to the magnetic phase II (Fig. 4.4). Therefore, we plot in Fig. 4.6 the ground state energy density versus $j_x$ along lines $j_1 = j_x - b$, with $b = 0$, 0.1, 0.2, and 0.3 from top to bottom. The ED results are shown by blue dots, whereas the D-SE results are shown by solid red lines. First, the small but finite

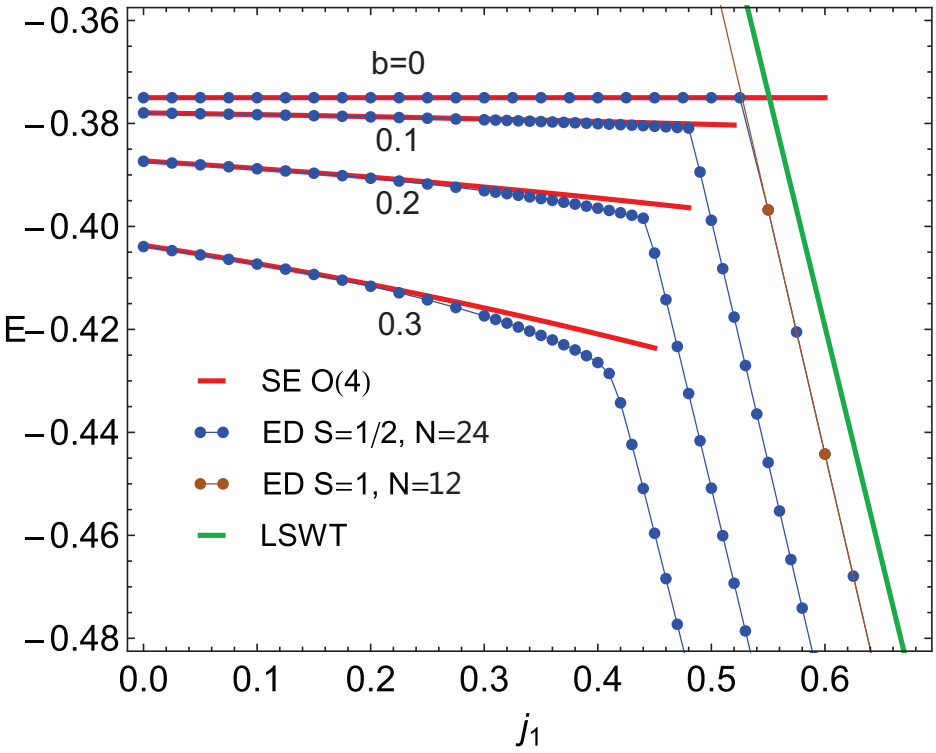


Figure 4.6: Ground state energy per spin $E$ as a function of $j_1$, for different paths parametrized by $j_x = j_1 + b$, with $b = 0$, 0.1, 0.2, and 0.3 (top to bottom). Blue dots: ED for S=1/2 bilayer model. Brown dots: ED for S=1 effective model on single layer. Solid red: D-SE. Green line: LSWT for S=1 effective single layer.

slope of $E$ at small $j_1$ increases as $b$ increases, and this demonstrates that properties in the IDP do not only depend on $b = j_x - j_1$. Therefore, in this figure we do not include the BO results. Second, we note that the results for $b = 0$ ($j_1 = j_x$) show that the ED and the D-SE coincide exactly at $-3/8$ up to the transition point $j_1^c = j_x^c \simeq 0.52$. This corresponds to the end of the bold red line in Fig. 4.4. At the transition point, the ED exhibits a kink in the energy versus $j_1$, signaling a first order transition into another type of ground state. Clearly the D-SE cannot detect this transition because it adiabatically evolves the dimer state with $j_1$, which is no longer the ground state for $j_1 > j_1^c$. Qualitative differences between the ED and the D-SE are also observed away from the diagonal line of $j_1 = j_x$, for $j_1 \gtrsim j_1^c$. Here again,

a clear change of slope is detected by the ED in Fig. 4.6 for $b = 0.1$ and 0.2. This supports our conclusion that the transition IDP-II is of the first order, as anticipated in the previous section. At $b = 0.3$, the ED result shows no clear signature of kink anymore, and this suggests that a transition replaces the first order ones for smaller $b$. This also implies the presence of a tricritical point.

Non-IDP phases will be analyzed in detail in the following Sections. Here we elaborate further on the transition from the IDP into the effective $S = 1$ AFM on the single layer hexagonal lattice explained in Sec. 4.1. We have verified this scenario with checking two points. First, we have performed ED calculations on a *single* layer spin-1 cluster comprising the same *site*-geometry as that of the *dimers* in the original cluster. The corresponding ground state energy is depicted by brown dots in Fig. 4.6. The excellent agreement between both types of ED calculations verifies our assertion of the transition from the IDP into the ground state of an $S = 1$ AFM Heisenberg model on the hexagonal single layer. Second, we have used the linear spin wave theory (LSWT) and calculated the ground state energy of the spin-1 Heisenberg antiferromagnet on the hexagonal lattice. Details are explained in Appendix [21, 42]. The result, which predicts $j_1^c \simeq 0.551$, is also shown in Fig. 4.6 and it is quantitatively very similar to the ED results. Since LSWT for a collinear state with $S = 1$ should be rather well defined, it would be interesting to analyze if the small difference of the critical coupling $\Delta j_1^c \approx 0.03$ between ED and LSWT is dominated by $O(1/S^2)$ correction or by finite size effects.

Away from the exact dimer line, the spin gap $\Delta$ in the dispersion of triplons will close at $\mathbf{k}_c = (0, 0)$ for sufficiently large $j_1 - j_x$. From the fourth order D-SE we get

$$\begin{aligned}\Delta(j_1, j_x) &= 1 - \frac{3}{16}\,|j_1 - j_x|\,\left|-8 + (j_1 - j_x)^3\right| \\ &\quad -\frac{3}{128}\,(j_1 - j_x)^2\Big[-16 + 8(j_1 - j_x) \\ &\quad +55\left(j_1^2 + j_x^2\right) - 14 j_1 j_x\Big]. \qquad (4.49)\end{aligned}$$

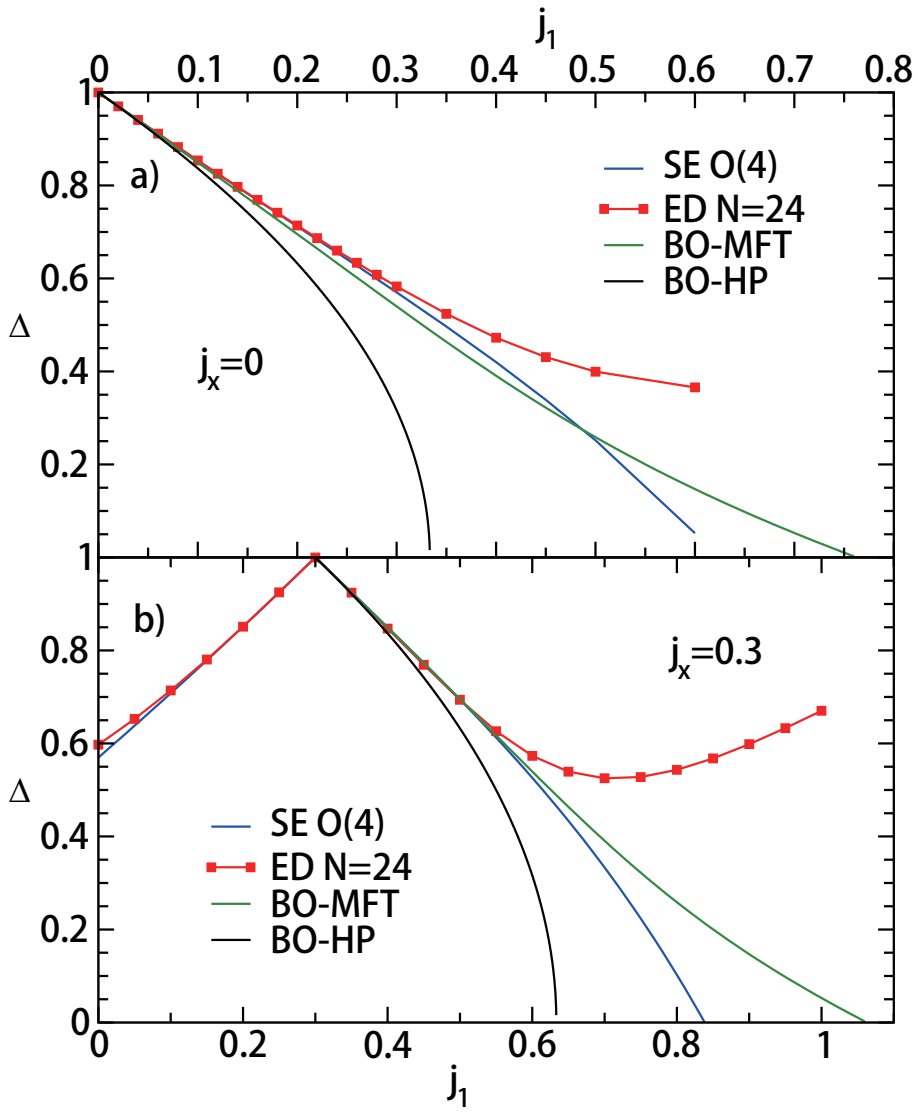


Figure 4.7: Spin gap $\Delta$ vs $j_1$ from ED (red with squares), $O(4)$ D-SE (blue), BO-HP (black), and BO-MFT (green), for a) at $j_x = 0$ with system size $N = 24$, see also Refs. [90, 159] and b) $j_x = 0.3$ with system size $N = 24$.

As for the ground state energy in Eq. (4.48), this satisfies $\Delta(j_1, j_x) = \Delta(j_x, j_1)$ and resembles the decoupled dimer state, i.e. $\Delta(j_1, j_1) = 1$. In Fig. 4.7 we compare Eq. (4.49) with the results of ED, BO-HP and BO-

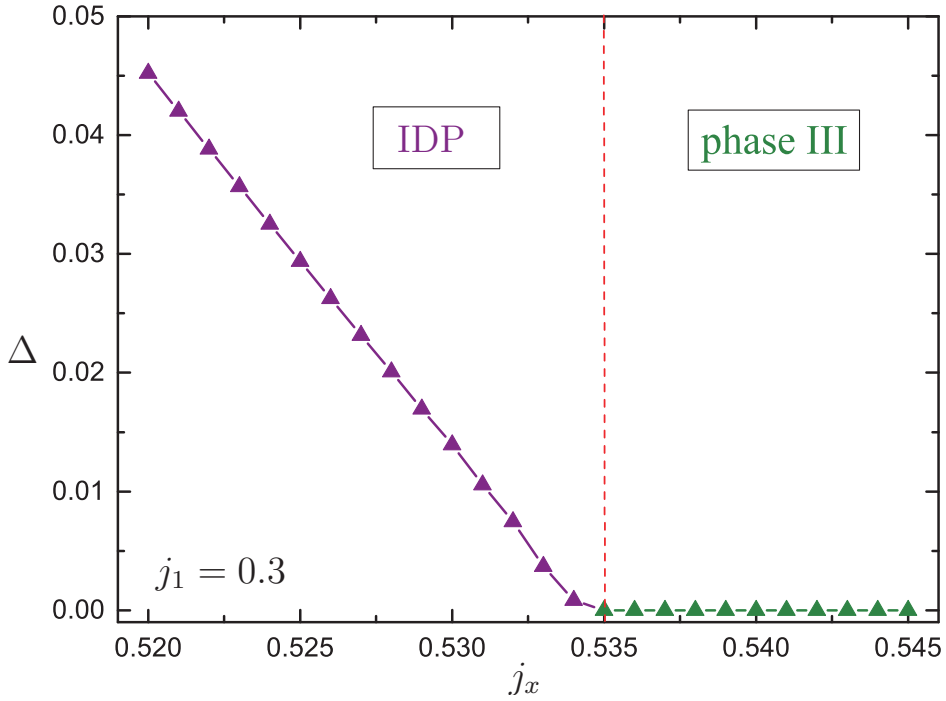


Figure 4.8: Example of SB-MFT gap at $j_1 = 0.3$ for the IDP-III transition and extrapolated to the thermodynamic limit.

MFT as a function of $j_1$ for the same two values of $j_x$ as in Fig. 4.5. As for the ground state energy, the BO results are identical in Fig. 4.7a) and b) up to a shift of origin and have been plotted only for positive $j_1 - j_x$. It is clear from the figure that the ED, D-SE, and BO-MFT results keep a finite spin gap for a larger range of exchange couplings away from the $j_1 = j_x$ line, while in the BO-HP result the gap closes more rapidly. The agreement between the ED, D-SE, and BO-MFT results is very good for $|j_1 - j_x| \lesssim 0.3$. Finite size effects for the spin gap in the ED are rather large, and the gap is minimum of $\Delta \sim 0.35$ at $j_x = 0$, while the minimum is $\Delta \sim 0.5$ for $j_x = 0.3$. A proper finite-size scaling analysis of the spin gap is unfeasible for ED, because of limitation due to large system size. Interestingly, while in the BO-HP result the gap at the critical point shows a standard square root behavior, with a negative curvature, self-consistency within the BO-MFT leads to a positive curvature of $\Delta$, with no obvious power law at gap closing. Thus, these two results contradict to each other.

We close this Section with two remarks on the SB-MFT result. In this approach, quantum disordered phases are also associated with a gapped excitation spectrum, and therefore the SB-MFT can equally well detect the IDP. However, while in the D-SE and BO theory the elementary excitations in the IDP actually correspond to the physical triplons, in SB-MFT they are bosonic spinons [2]. In order to obtain a proper spin excitation spectrum including the gap, the two-spinon propagator needs to be evaluated (see e.g. Ref. [107]). To do this, it is necessary to *include* interactions between spinons, in order to confine spinons into a physical spin-triplet excitation. It is beyond the level in our present approach and we will not try such calculations. Despite this, we use SB-MFT to determine the transition points from the IDP to the magnetic phases of the bilayer based on the closing of the spinon gap, since long range magnetic order characterized by a condensation of the bosons should lead to a gapless spectrum. In Fig. 4.8 we show a representative example. As the second remark, let us note that SB-MFT predicts a phase transition point $j_1^c = 0.547$ on the $j_1 = j_x$ line for the transition between the IDP and the magnetic phase II, which is larger than the ED result but agrees very well with the LSWT prediction $j_1^c = 0.551$.

## 4.6 Magnetic phases

In this section we analyze ground-state properties of the phases I, II and III of Fig. 4.4. These are gapless phases with magnetic long-range order (LRO) and a spin structure explained on the classical level in Sec. 4.2.

To investigate how these orderings survive under quantum fluctuations, we calculate the static spin correlation functions $C(r) = \langle S_0^z S_r^z \rangle$. Panels (b)-(d) of Fig. 4.9 show $C(r)$ where $r$ is the distance along the green path depicted in panel (a). We have selected three different points of parameters space to illustrate the behavior of the correlations along the considered path. Panel (b) shows $C(r)$ for the point $(j_1, j_x) = (0.7, 0.3)$, whereas the panel (d) shows the result for its symmetric point $(0.3, 0.7)$. In both cases the sign alternation in $C(r)$ is consistent with the spin configuration in the magneti-

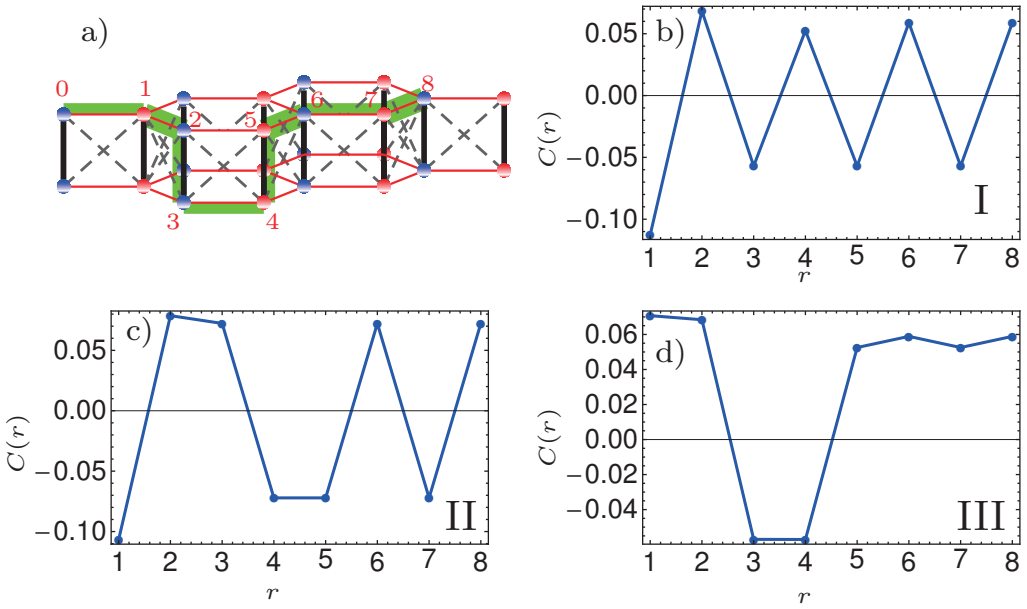


Figure 4.9: Static correlation function $C(r)$ vs. $r$ along the green path depicted in panel a), obtained by means of ED on a finite cluster of 24 spins mainly performed by C. A. Lamas [106]. Panel b) $(j_1, j_x) = (0.7, 0.3)$, c) $(0.7, 0.7)$, and d) $(0.3, 0.7)$ clearly show a pattern consistent with the classical structure shown in regions I, II, and III of Fig. 4.4.

cally ordered phases I and III illustrated in the insets of Fig. 4.4. The same occurs with the panel (c) for $(j_1, j_x) = (0.7, 0.7)$. This case is consistent with the classical spin pattern depicted in the inset of phase II in Fig. 4.4.

Although short-distance correlations in the ED results are consistent with the ordered phases, constraints in the cluster size does not permit to obtain the actual form of $C(r)$ for large distances and to conclude LRO. These aspects can be considered with complementary techniques, such as the SB-MFT, which has been successfully used to study two-dimensional frustrated Heisenberg antiferromagnets [48, 49, 55, 90, 97, 99, 109–111].

Fig. 4.10 shows the SB-MFT result of the spin-spin correlation between spins, and traversing on the same layer along one of the 'zigzag-chain' paths of the hexagonal lattice, for a system of 10000 sites at $(j_1, j_x) = (0.8, 0.3)$ (phase I); $(0.9, 0.6)$ (phase II); and $(0.52, 0.3)$ (IDP). The last case is shown to contrast the magnetic phases. Due to the mirror symmetry of the phase

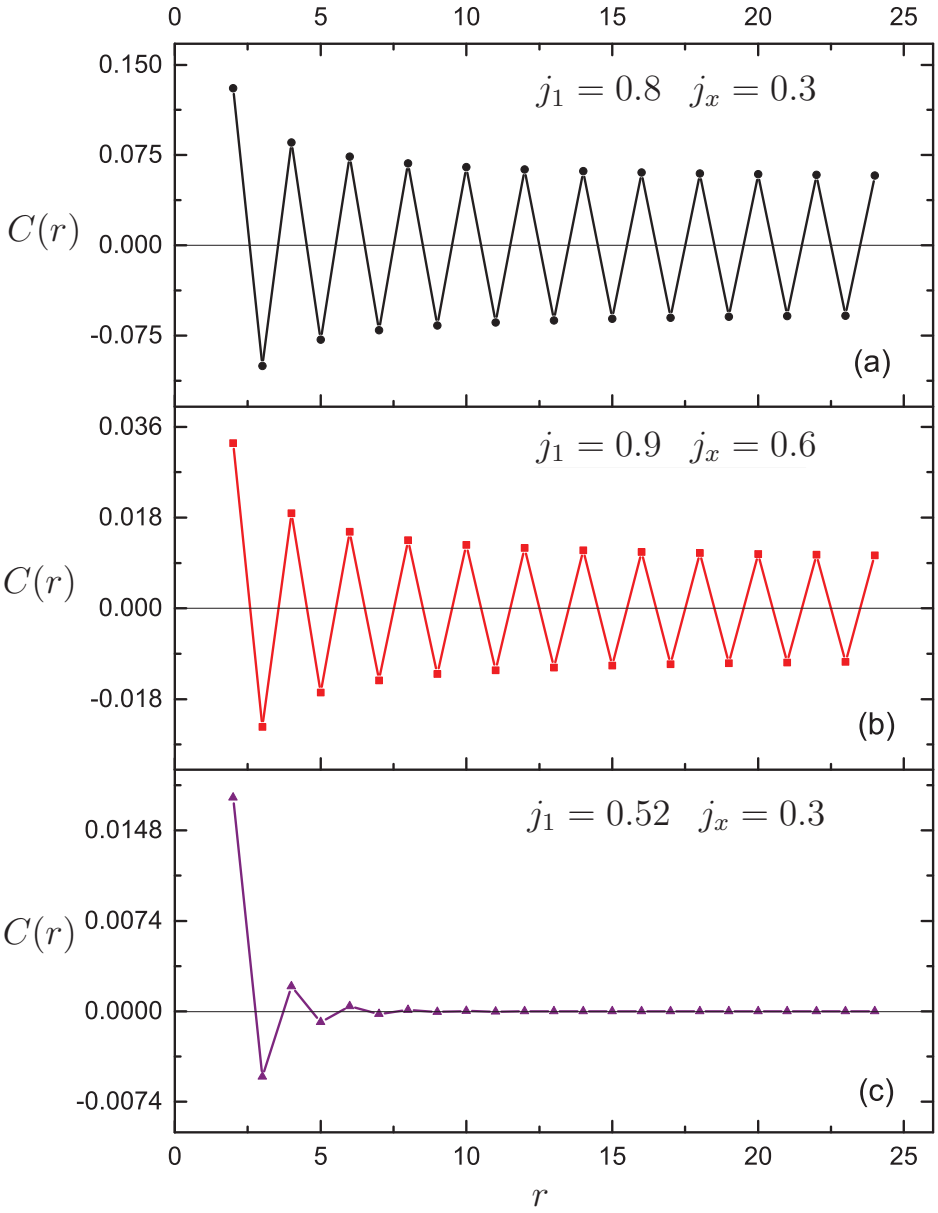


Figure 4.10: Spin-spin correlation between spins belonging to the same layer in the zigzag direction obtained by SBMFT for a 10000 sites system. It is shown for the three different phases in the $j_1 > j_x$ side of the phase diagram (Fig. 4.4): (a) $j_1 = 0.8$, $j_x = 0.3$ (phase I), (b) $j_1 = 0.9$, $j_x = 0.6$ (phase II), and (c) $j_1 = 0.52$, $j_x = 0.3$ (IDP).

diagram along the line $j_1 = j_x$, we confine the figure to the part $j_1 \geqslant j_x$. While AFM LRO is clearly visible in the panels (a) and (b) on each layer,

the difference between (a) and (b) is about the nearest-neighbor interlayer spin-spin correlation which is negative in the case (a) and positive in the case (b). This corresponds to AFM in phase I and FM in phase II, in agreement with the ED results. Panel (c) of Fig. 4.10 clearly shows that the IDP phase has short range spin-spin correlations only, consistently with the presence of a finite spin gap.

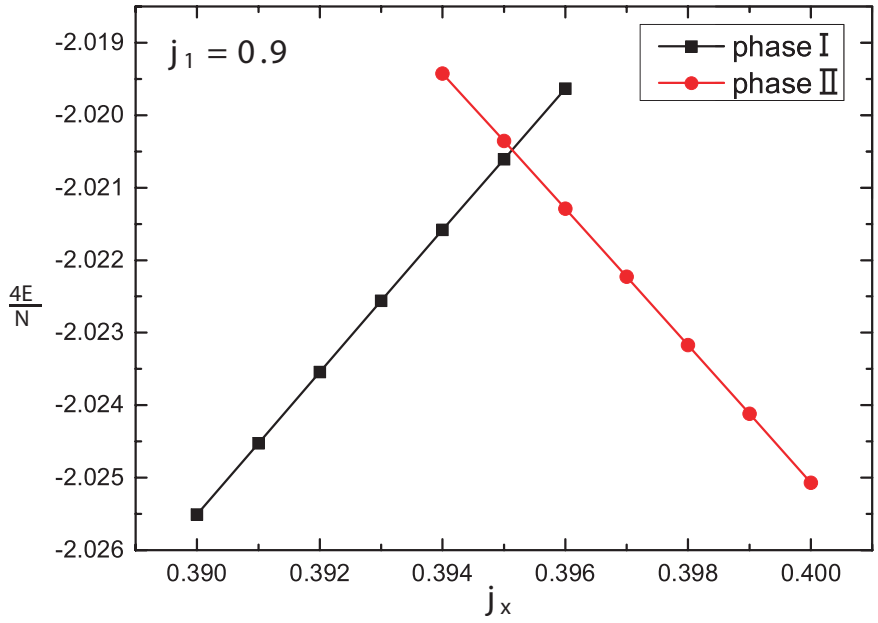


Figure 4.11: Energy per unit cell from SB-MFT shows a crossing at $j_1 = 0.9$ for the phase transition I-II.

To determine the location of the transitions between the LRO phases we should notice that these phases have no subgroup relations to each other. Therefore any direct transitions between them are of first order, and they can be determined from a crossing in the ground state energy. This is true, both, for the ED and SB-MFT. In Fig. 4.11 a representative result of the SB-MFT is depicted for the phase transition I-II. Similar results are obtained by the ED calculation and will be summarized in the next Section.

Let us finally mention that we have not found any evidence of the existence of intermediate phases (e.g. non-collinear structures like helical order)

for the I-II and II-III phase boundaries. However, the limitations of the techniques employed, especially the small system sizes in the ED calculations, as well as the mean field character of SB-MFT, does not allow completely exclude the possibility of such intermediate phases.

## 4.7 Quantum phase diagram

In this Section we compare boundaries in the ground-state phase diagram determined by all the methods used in this work. The main result is Fig. 4.12 and it summarizes our findings of the SB-MFT, BO-HP, BO-MFT, D-SE, and ED calculations. This figure is the *quantitative* phase diagram, corresponding to the schematic one in Fig. 4.4. Several comments are in order.

To begin, we note that for the first order transitions between the phases I↔II, II↔III, and IDP↔II, the SB-MFT and ED results agree quantitatively, and they are shown by magenta and green open circles, respectively in Fig. 4.12. The lines of first order transition are determined by the crossing points of the ground state energy in our study. The energy is less susceptible to errors in various approaches, e.g. finite size effects. We note that SB-MFT technique is more convenient than the others to estimate all the phase boundaries, irrespective of whether the transition is first or second order.

In contrast to the first order transitions, for the second order transitions between the IDP and I and III phases, our methods complementary to the SB-MFT determine a range of transition points less precisely, since the gap closing, i.e. the divergence of the correlation length is sensitive to the method used. Nevertheless, Fig. 4.12 clearly shows that both IDP↔(I, III) transition points are centered around the two lines $|j_x - j_1| \sim 0.6(\pm 0.2)$, where the precision $\pm 0.2$ comes from the discrepancy among the various approaches. Note that this scattering also limits the precision of the location of the two tricritical points that separate the phases IDP-I-II and IDP-II-III.

Remarkably all the methods used predict essentially straight critical lines for the IDP↔(I, III) transitions with approximately unit slope, at least in

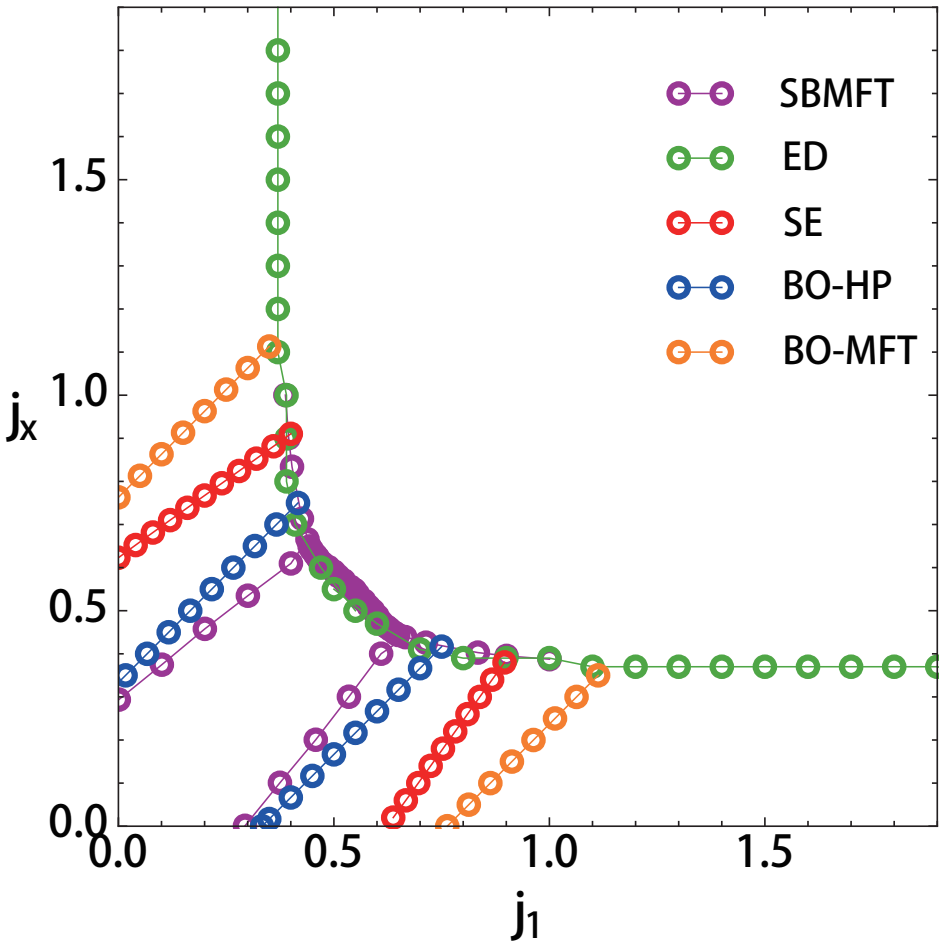


Figure 4.12: Ground-state phase boundaries determined by the different techniques considered.

the scale of the plot. This is a direct consequence of the last term in Eq. (4.4), perturbing the exact dimer state. As a consequence, e.g. in both BO methods, and by construction, the triplon hopping amplitude is a function of the difference of exchanges $|j_1 - j_x|$ alone. Yet, the D-SE result at $O(4)$ level (red open circles in Fig. 4.12) exhibits a small curvature of the transition lines. In the BO-HP result it is possible to obtain an analytical expression, and the critical lines are $j_x = j_1 \pm 1/3$, depicted by blue open circles in Fig. 4.12. For the BO-MFT result (orange open circles), the offset $|j_1 - j_x| = 1/3$ is replaced by a numerical constant determined by the analytic self-consistency equations, and that is $\approx 0.76$ (see Fig. 4.7a)). Note that in all the cases

(except SB-MFT) the critical line ends at the border of phase II, which is obviously an artifact of the methods. This is because as we have previously mentioned, level crossings are not detected in the D-SE nor BO approaches.

## 4.8 Conclusion

We have studied the ground-state phase diagram of the Heisenberg model on the bilayer honeycomb lattice including interlayer frustration. To characterize the different phases present in the model, as well as their transitions, we have calculated a variety of quantities, such as ground state energies, low energy excitations, triplet gaps and static spin-spin correlations. This has been done, using several methods complementary to each other: bond operator and Schwinger bosons mean field theories, dimer series expansion, and exact diagonalization of finite systems.

The main results of our work are summarized in the schematic phase diagram of Fig. 4.4. This diagram is symmetric with respect to the line $j_1 = j_x$. For $j_1 = j_x \leq j_x^c \approx 0.55$, the ground state is an exact interlayer dimer-product state. This ground state and its elementary triplet excitations are identical to those in the decoupled dimer limit ($j_1 = j_x = 0$). With departing from the diagonal line, a dimerized phase evolves adiabatically from the exact ground state and extends over a region around the diagonal line. This gapped *interlayer dimer phase* (IDP) has been analyzed by means of bond operator theory and dimer series expansion (complemented with exact diagonalization), both of which are exact for the pure singlet product state.

In contrast to the IDP phase, which is gapped and magnetically disordered due to quantum origin, the other phases present in the model are magnetically ordered, and thus gapless, and classical in nature. In particular we have identified three magnetic phases, denoted as I, II, and III in Fig. 4.4. The phases I and II are Néel-like, whereas the phase III exhibits a columnar order. The magnetic structure of these phases has been clarified both by exact diagonalization on finite systems of $N = 24$ sites and by Schwinger boson mean field theory, and both show qualitatively identical results. In

particular the phase II along the diagonal line $j_1 = j_x > j_x^c$ is equivalent to the ground state of an effective spin-1 Heisenberg model on the single-layer honeycomb lattice with an antiferromagnetic coupling $j_1 = j_x$.

All the methods suggest that the transitions are of the first order (level crossing) between the phases I↔II, II↔III and IDP↔II, while second order (gap closing) between the phases IDP↔I and IDP↔III. A quantitative analysis of the ground-state phase diagram is performed by the combination of all methods. For all the first order transitions exact diagonalization and Schwinger boson mean field theory agree well to each other. For the second order transitions, the different methods used have shown a qualitative agreement.

To the best of our knowledge, it is the first time to provide a comprehensive study about the ground-state phase diagram of a Heisenberg model on the bilayer honeycomb lattice including interlayer frustration, and this work should play an important role in the understanding of the quantum phases and the competition between the frustration and unfrustration couplings in frustrated magnets.

# Chapter 5

# Summary and perspectives

In this thesis, we study the ground state of the frustrated Heisenberg models on the single layer and bilayer honeycomb lattices, motivated by recent theoretical and experimental progresses about the quantum disordered phases in the honeycomb-lattice antiferromagnets. The main approach we have used is an improved version of Schwinger boson mean-field theory, which uses mean fields corresponding to antiferromagnetic and ferromagnetic correlations on equal footing. This is important for frustrated models as pointed in Ref. [100]. We have also assumed that the bond mean fields may dependent on their bond directions. Therefore, we are able to identify whether the phases break the lattice rotational symmetry or not.

Chapter 2, Chapter 3 and Chapter 4 are the main parts of this thesis. In Chapter 2, we used the improved Schwinger boson mean-field theory, and determined the ground state phase diagram of the $S = 1/2$ $J_1$-$J_2$ Heisenberg model on the single-layer honeycomb lattice in the region of $0 \leq J_2/J_1 \leq 0.5$, where $J_1$ is the nearest neighbor coupling and $J_2$ is the next nearest neighbor coupling. The magnetically ordered Néel and spiral phases are found for $0 \leq J_2/J_1 \lesssim 0.2075$ and $0.398 \lesssim J_2/J_1 \leq 0.5$, respectively. In the intermediate region $0.2075 \lesssim J_2/J_1 \lesssim 0.398$, the spin gap is finite and the local magnetization is zero, which indicates a magnetically disordered ground state. Our conclusion about this disordered region quantitatively agrees well with recent numerical results [40, 41, 50, 53]. In addition, we have examined

the order parameter $|\psi|$ of $C_3$ lattice rotational symmetry and identified two different phases in the magnetically disordered region. One is a gapped spin liquid phase for $0.2075 \lesssim J_2/J_1 \lesssim 0.3732$. This shows short-range antiferromagnetic correlations and preserves both the $C_3$ rotational symmetry and the lattice translational symmetry. The other is a staggered valence bond crystal phase for $0.3732 \lesssim J_2/J_1 \lesssim 0.398$. This breaks the $C_3$ rotational symmetry but preserves the lattice translational symmetry. We also checked the possibility of the plaquette valence bond crystal phase, which breaks the lattice translational symmetry. It was shown that the gapped spin liquid phase and the staggered valence bond crystal phase are energetically favorable over the plaquette valence bond crystal phase. It is the key finding of Chapter 2 that two types of magnetically disordered phases exist in the intermediate frustration region and the lattice rotational symmetry breaks in the part of large $J_2/J_1$ in the magnetically disordered region. There are two physical mechanisms which stabilize these two phases. First, the low coordination number of the honeycomb lattice and the frustration from the next nearest neighbor antiferromagnetic couplings $J_2$ enhance quantum fluctuations. The strong quantum fluctuations tend to suppress the magnetic long-range order. Secondly, the frustration from the next nearest neighbor antiferromagnetic couplings $J_2$ tend to break the $C_3$ lattice rotational symmetry. This physical mechanism exists even in the classical case, since for $J_2/J_1 > 1/6$ this model has a family of degenerate spiral ground states, and each state breaks the $C_3$ lattice rotational symmetry.

In Chapter 3, we have studied the melting of Néel order and magnetically disordered ground states of the frustrated Heisenberg model on the bilayer honeycomb lattice by the same approach, complemented with exact diagonalizations performed by C. A. Lamas [90] and linear spin wave theory. We have estimated the melting curve of Néel order in $J_2$-$J_\perp$ plane for the $S = 1/2$ case by analyzing sublattice magnetization and spin gap, with controlling the interlayer coupling $J_\perp$. We have also calculated the spin correlations characterizing these phases. The key finding of this chapter is the re-entrant behavior of the melting curve in the region of $0.2075 \lesssim J_2/J_1 \lesssim 0.289$. At $J_\perp = 0$ the system is a gapped spin liquid, which shows short-range an-

tiferromagnetic order, but increasing the interlayer coupling up to a finite (and small) value $J_\perp^{**}(J_2)$, a phase transition occurs to the Néel ordered phase. Increasing $J_\perp$ further, the Néel order is destroyed at $J_\perp^{*}(J_2)$, and the systems changes to the interlayer dimer phase. The dependence of the sublattice magnetization on $J_\perp$ also confirms the reentrant behavior, since a small bilayer coupling enhances the value of the sublattice magnetization. This is consistent with the behavior of the sublattice magnetization observed in the $S = 1/2$ unfrustrated Heisenberg model on the bilayer honeycomb and square lattices [76, 77, 83, 86]. Another interesting part is the region of $0.3732 \lesssim J_2/J_1 \lesssim 0.398$. For $J_\perp = 0$ in this region, each layer is a valence bond crystal which breaks the lattice rotational symmetry, and as $J_\perp$ increases, the system changes to a interlayer dimer state which preserves the lattice rotational symmetry. We expect that the $C_3$ lattice rotational symmetry breaking disappears upon increasing $J_\perp$, and we leave this point for future studies.

In Chapter 4, we have studied the ground-state phase diagram of the Heisenberg model on the bilayer honeycomb lattice including interlayer frustration due to $J_x$ using several complementary techniques: Schwinger boson approach, bond operator approaches, dimer series expansion and exact diagonalization of finite systems. Here $J_x$ is the next-nearest neighbor coupling between the two layers. Among these approaches, dimer series expansion calculation was mainly performed by M. Arlego and W. Brenig [106], and exact diagonalization calculation was mainly performed by C. A. Lamas [106]. We have identified the appeared quantum phases and determined their phase boundaries in the $J_1$-$J_x$ plane with $J_\perp$ fixed to be 1 by calculating the ground-state energy, excitation spectrum, singlet-triplet gap, and spin correlation functions. The phase diagram is symmetric with respect to the line of $J_1 = J_x$, and it has four phases. We have analyzed the phase diagram by various methods explained above. For $J_1 = J_x \leq j_x^c \approx 0.55 J_\perp$, the model is exactly solvable and its ground state is an interlayer dimer product state. Moving away from the line of $J_1 = J_x$, a gapped interlayer dimer phase (IDP) evolves adiabatically from the exact dimer product state and extends over a region around the diagonal line. The other three phases in the phase dia-

gram are magnetically ordered with gapless excitations. The phases I and II are Néel-like, whereas III exhibits a columnar order. The phase transitions are first order (level crossing) for the transitions I↔II, II↔III and IDP↔II, while second order (gap closing) for the transitions IDP↔I and IDP↔III.

In the following we comment about possible future extensions of the present thesis. Firstly, it is interesting to study the effects of local fluctuations of the bosonic chemical potential and examine how this improves the Schwinger boson mean-field appraoch [125], since the local constraints of Schwinger boson number have been treated in average in the present thesis. Trumper *et al.* [99] has included such correction for the $J_1$-$J_2$ square lattice by means of collective coordinate methods and it is possible to generalize their approach to the honeycomb lattice case. Secondly, since there are still very few works for the frustrated Heisenberg model on the bilayer honeycomb lattice, it is interesting to apply other methods to this model, such as the bond operator mean-field theory [148]. Finally, concerning the model itself, it is important to study the effects of anisotropy in interactions added to the Heisenberg model. For example, Dzyaloshinskii-Moriya interactions [160–163] are forbidden between nearest neighbor sites in a single layer honeycomb lattice, since the middle of each bond is an inversion center. However, between the next-nearest neighbor sites, Dzyaloshinskii-Moriya interactions are generally finite. The bilayer case is more interesting. For all of the nearest neighbor, next-nearest neighbor and the interlayer bonds, Dzyaloshinskii-Moriya interactions are allowed. It is important and interesting to study the effects of the Dzyaloshinskii-Moriya terms.

Our results are relevant to understanding magnetic properties in honeycomb-lattice antiferromagnetic materials such as the newly synthesized manganese oxide $Bi_3Mn_4O_{12}(NO_3)$ [11]. The variant of this system where $Mn^{4+}$ ions with $S = 3/2$ are replaced by $V^{4+}$ ions with $S = 1/2$ may be a possible candidate to realize the model discussed in this thesis. The magnetically disordered phases induced by the frustration and interlayer couplings may stimulate the explanation for the spin-liquid-like behavior of the material $Bi_3Mn_4O_{12}(NO_3)$ [11]. The values of the interactions estimated by neutron scattering experiments [13,14] are $J_1 = 1.4$ meV, $J_2 = 0.2$ meV and $J_\perp = 0.7$

meV. As we have shown in Fig. 3.3, the critical value $J_\perp^*/J_1$ is 2.609 at $J_2/J_1 = 0.14$. Therefore, it is unlikely that the interlayer coupling stabilizes the disordered phase experimentally observed. Another possibility is that some frustration induced magnetically disordered phase may appear, such as the GSL or the staggered VBC which we have shown in Chapter 2. Since $Bi_3Mn_4O_{12}(NO_3)$ shows short-range antiferromagnetic correlations at low temperatures [13, 14], as we have observed in the GSL state, we expect that the ground state of this compound may be the GSL state, which also shows short-range antiferromagnetic correlations. The staggered VBC state does not show short-range antiferromagnetic correlations, and therefore it is not the ground state of this compound. We should note that the experimentally estimated values of $J_2/J_1$ is smaller than our theoretical result of the Néel phase boundary $(J_2/J_1)_c \simeq 0.2075$ for $S = 1/2$ case, as we have discussed in Chapter 2. However, we expect that $S = 3/2$ case may have a smaller critical value $(J_2/J_1)_c$ than the $S = 1/2$ case. Further experimental study for precise exchange parameters and further theoretical study for $S = 3/2$ case are necessary before further conclusions can be obtained.

Our studies of the frustrated systems on the honeycomb lattice provide a systematic investigation about the effects of frustration to the ground state and we believe that our results provide important information in understanding possible exotic phases and competition between the frustration and unfrustration couplings in frustrated magnets.

# Chapter 6

# Appendix

## 6.1 Linear Spin Wave Theory at $j_1 = j_x$

Here we briefly explain the equations necessary to determine the transition point $j_1^c$ for the first order transition between IDP and II phases along the line $j_1 = j_x$ based on the linear spin wave theory. In the following, as we have introduced in Sec. 4.1, the operator $\mathbf{L}$ is the bond spin operator and $L$ is its quantum number. In the IDP phase for $j_1 = j_x$, the ground state energy is

$$E\left(\text{all bonds in } L = 0 \text{ sector}\right)/J_\perp = -\frac{3}{2}N_\triangle\,, \tag{6.1}$$

where $N_\triangle$ is the number of triangular unit cells. The Hamiltonian of the "all bonds in $L = 1$ sector" on the other hand reads

$$H\left(\text{all bonds in } L = 1 \text{ sector}\right)/J_\perp = \frac{1}{2}N_\triangle + j_1 \sum_{\langle lm \rangle} \mathbf{L}_l \cdot \mathbf{L}_m\,, \tag{6.2}$$

where the sum is taken over nearest-neighbor site pairs on the hexagonal lattice. The ground state of the latter is known to be an Néel state, and its energy per site is calculated by the linear spin wave theory, up to the order of $O(1/S)$ [21, 42]:

$$\frac{E_{LSWT}}{2N_{\triangle}J_{\perp}} = j_1 S^2 \left\{ -\frac{3}{2} + \frac{2}{S}\int_0^{\frac{2\pi}{3}} dk_y \int_0^{-\frac{1}{\sqrt{3}}k_y + \frac{4\pi}{3\sqrt{3}}} dk_x \frac{3\sqrt{3}}{8\pi^2} \left[ 2 - \right.\right.$$
$$\left.\left. \cos^2\frac{\sqrt{3}k_y}{2} - \cos\frac{3k_x}{2}\cos\frac{\sqrt{3}k_y}{2} \right]^{1/2} - \frac{3}{2S} \right\}$$
$$\simeq \quad j_1 S^2 \left( -\frac{3}{2} - \frac{0.314763}{S} \right) . \tag{6.3}$$

For $S = 1$ this reads

$$\frac{E_{LSWT}}{2N_{\triangle}J_{\perp}} \simeq -1.81476\, j_1 \,, \tag{6.4}$$

which is plotted in Fig. 4.6. Together with (6.1), (6.2) and keeping in mind that each "*site*" in (6.3) stands for *two* spins on the original bilayer lattice, we obtain

$$\frac{E\,(\text{all } L = 0 \text{ sector})}{2N_{\triangle}J_{\perp}} = -\frac{3}{4}, \tag{6.5}$$

$$\frac{E\,(\text{all } L = 1 \text{ sector})}{2N_{\triangle}J_{\perp}} = \frac{1}{4} - 1.81476 j_1. \tag{6.6}$$

By equating these two, one obtains the value at the transition point

$$j_1^c \simeq 0.551036.$$

.

# Bibliography


[1] (ed.) H. T. Diep, *Frustrated Spin Systems*, (World Scientific, Singapore 2005).

[2] (eds.) C. Lacroix, P. Mendels, and F. Mila, *Introduction to Frustrated Magnetism*, (Springer-Verlag, Berlin, 2011).

[3] P. W. Anderson, Mater. Res. Soc. Bull. **8**, 153 (1973); P. Fazekas and P. W. Anderson, Phil. Mag. **30**, 423 (1974); P. W. Anderson, Science **235**, 1196 (1987).

[4] L. Balents, Nature **464**, 199 (2010).

[5] G. Misguich and C. Lhuillier, *Two-Dimensional Quantum Antiferromagnets*, in Ref. [1].

[6] S. Sachdev, arXiv:0901.4103 (Rapporteur talk at the 24th Solvay Conference on Physics, *"Quantum Theory of Condensed Matter"*, Brussels, Oct 2008.)

[7] N. Read and S. Sachdev, Phys. Rev. B **42**, 4568 (1990).

[8] X. G. Wen , Phys. Rev. B **44**, 2664 (1991).

[9] C. Lhuillier and G. Misguich, *Introduction to Quantum Spin Liquids*, in Ref. [2].

[10] L. Néel, Annales de Physique (Paris) **3**, 137 (1948).

[11] O. Smirnova, M. Azuma, N. Kumada, Y. Kusano, M. Matsuda, Y. Shimakawa, T. Takei, Y. Yonesaki, and N. Kinomura, J. Am. Chem. Soc. **131**, 8313 (2009).

[12] S. Okubo, F. Elmasry, W. Zhang, M. Fujisawa, T. Sakurai, H. Ohta, M. Azuma, O. A. Sumirnova, and N. Kumada, J. Phys.: Conf. Series **200**, 022042 (2010).

[13] M. Matsuda, M. Azuma, M. Tokunaga, Y. Shimakawa, and N. Kumada Phys. Rev. Lett. **105**, 187201 (2010).

[14] M. Azuma, M. Matsuda, N. Onishi, S. Olga, Y. Kusano, M. Tokunaga, Y. Shimakawa, and N. Kumada, J. Phys.: Conf. Series **320**, 012005 (2011).

[15] H. C. Kandpal and J. van den Brink, Phys. Rev. B **83**, 140412(R) (2011).

[16] E. Manousakis, Rev. Mod. Phys. **63**, 1 (1991).

[17] H. A. Bethe, Z Phys. **74**, 205 (1931).

[18] Weihong Zheng, J. Oitmaa, and C. J. Hamer, Phys. Rev. B **43**, 8321 (1991).

[19] Weihong Zheng and C. J. Hamer, Phys. Rev. B **47**, 7961 (1993).

[20] Anders W. Sandvik, Phys. Rev. B **56**, 11678 (1997)

[21] Weihong Zheng, J. Oitmaa, and C. J. Hamer, Phys. Rev. B **44**, 11869 (1991).

[22] Eduardo V. Castro, N. M. R. Peres, K. S. D. Beach, and Anders W. Sandvik, Phys. Rev. B **73**, 054422 (2006).

[23] M. A. Metlitski and S. Sachdev, Phys. Rev. B **77**, 054411 (2008).

[24] R. K. Kaul, M. A. Metlitski, S. Sachdev, and C. Xu, Phys. Rev. B **78**, 045110 (2008).

[25] L. Wang and A. W. Sandvik, Phys. Rev. B **81**, 054417 (2010).

[26] R. Moessner, S.L. Sondhi, and P. Chandra, Phys. Rev. B **64**, 144416 (2001).

[27] A. Ralko, M. Mambrini and D. Poilblanc, Phys. Rev. B **80**, 184427 (2009).

[28] K. Takano, Phys. Rev. B **74**, 140402 (2006).

[29] M. Hermele, Phys. Rev. B **76**, 035125 (2007).

[30] R. Kumar, D. Kumar, and B. Kumar, Phys. Rev. B **80**, 214428 (2009).

[31] A. Mattsson, P. Fröjdh, and T. Einarsson, Phys. Rev. B **49**, 3997 (1994).

[32] R. Ganesh, D.N. Sheng, Y.-J. Kim, and A. Paramekanti, Phys. Rev. B **83**, 144414 (2011).

[33] T. Einarsson and H. Johannesson, Phys. Rev. B **43**, 5867 (1991).

[34] S. Okumura, H. Kawamura, T. Okubo, and Y. Motome, J. Phys. Soc. Jpn. **79**, 114705 (2010).

[35] H. D. Rosales, D. C. Cabra, C. A. Lamas, P. Pujol, and M. E. Zhitomirsky, Phys. Rev. B **87**, 104402 (2013).

[36] A. Mulder, R. Ganesh, L. Capriotti, and A. Paramekanti, Phys. Rev. B **81**, 214419 (2010).

[37] F. Wang, Phys. Rev. B **82**, 024419 (2010).

[38] H. Mosadeq, F. Shahbazi, and S. A. Jafari, J. Phys.: Condens. Matter **23**, 226006 (2011).

[39] B. K. Clark, D. A. Abanin, and S. L. Sondhi, Phys. Rev. Lett. **107**, 087204 (2011).

[40] F. Mezzacapo and M. Boninsegni, Phys. Rev. B **85**, 060402(R) (2012).

[41] R. F. Bishop, P. H. Y. Li, D. J. J. Farnell, and C. E. Campbell, J. Phys.: Condens. Matter **24**, 236002 (2012).

[42] E. Rastelli, A. Tassi, and L. Reatto, Physica B **97**, 1 (1979).

[43] J. B. Fouet, P. Sindzingre, and C. Lhuillier, Eur. Phys. J. B **20**, 241 (2001).

[44] S. Katsura, T. Ide, and T. Morita, J. Stat. Phys. **42**, 381 (1986)

[45] J. Oitmaa and R. R. P. Singh, Phys. Rev. B **84**, 094424 (2011).

[46] P. H. Y. Li, R. F. Bishop, D. J. J. Farnell, J. Richter, and C. E. Campbell, Phys. Rev. B **85**, 085115 (2012).

[47] R. F. Bishop and P. H. Y. Li, Phys. Rev. B **85**, 155135 (2012).

[48] D. C. Cabra, C. A. Lamas, and H. D. Rosales, Phys. Rev. B **83**, 094506 (2011).

[49] D. C. Cabra, C. A. Lamas, and H. D. Rosales, Mod. Phys. Lett. B 25, 891 (2011).

[50] A. F. Albuquerque, D. Schwandt, B. Hetényi, S. Capponi, M. Mambrini, and A. M. Läuchli, Phys. Rev. B **84**, 024406 (2011).

[51] J. Reuther, D. A. Abanin, and R. Thomale, Phys. Rev. B **84**, 014417 (2011).

[52] D. J. J. Farnell, R. F. Bishop, P. H. Y. Li, J. Richter, and C. E. Campbell, Phys. Rev. B **84**, 012403 (2011).

[53] P. H. Y. Li, R. F. Bishop, D. J. J. Farnell, and C. E. Campbell, Phys. Rev. B **86**, 144404 (2012).

[54] Hong-Yu Yang, A F. Albuquerque, S. Capponi, A. M Lauchli, and K. P. Schmidt, New J. Phys. **14**, 115027 (2012).

[55] Hao Zhang and C. A. Lamas, Phys. Rev. B 87, 024415 (2013).

[56] R. Ganesh, J. van den Brink, and S. Nishimoto, Phys. Rev. Lett. **110**, 127203 (2013).

[57] Z. Zhu, D. A. Huse, and S. R. White, Phys. Rev. Lett. **110**, 127205 (2013).

[58] S. S Gong, D. N. Sheng, O. I. Motrunich, and M. P. A. Fisher, Phys. Rev. B **88**, 165138 (2013).

[59] R. F. Bishop, P. H. Y. Li, and C. E. Campbell, J. Phys.: Condens. Matter **25**, 306002 (2013).

[60] Z.Y. Meng, T.C. Lang, S. Wessel, F.F. Assaad, and A. Muramatsu, Nature **464**, 847 (2010).

[61] Y.-M. Lu and Y. Ran, Phys. Rev. B **84**, 024420 (2011).

[62] H.Y. Yang and K.P. Schmidt, Europhys. Lett. **94**, 17004 (2011).

[63] A. Vaezi and X.G. Wen, arXiv:1010.5744v1 (2010).

[64] A. Vaezi, M. Mashkoori, and M. Hosseini, Phys. Rev. B **85**, 195126 (2012).

[65] M.-T. Tran and K.-S. Kim, Phys. Rev. B **83**, 125416 (2011).

[66] S. Sorella, Y. Otsuka, and S. Yunoki, Sci. Rep. **2**, 992 (2012).

[67] A. H. MacDonald, S. M. Girvin, and D. Yoshioka, Phys. Rev. B **37**, 9753 (1988); *ibid.* **41**, 2565 (1990).

[68] A. H. Castro Neto, F. Guinea, N. M. R. Peres, K. S. Novoselov, and A. K. Geim, Rev. Mod. Phys. **81**, 109 (2009).

[69] M. Z. Hasan and C. L. Kane, Rev. Mod. Phys. **82**, 3045 (2010).

[70] X. L. Qi and S. C. Zhang, Rev. Mod. Phys. **83**, 1057 (2011).

[71] E. Dagotto, Rev. Mod. Phys. **66**, 763 (1994).

[72] K. Hida, J. Phys. Soc. Jpn. **61**, 1013 (1992).

[73] A. J. Millis and H. Monien, Phys. Rev. Lett. **70**, 2810 (1993).

[74] A. J. Millis and H. Monien, Phys. Rev. B **50**, 16606 (1994).

[75] A. W. Sandvik and D. J. Scalapino, Phys. Rev. Lett. **72**, 2777 (1994).

[76] A. V. Chubukov and D. K. Morr, Phys. Rev. B **52**, 3521 (1994).

[77] K. K. Ng, F. C. Zhang, and M. Ma, Phys. Rev. B **53**, 12196 (1996).

[78] M. P. Gelfand, Z. Weihong, C. J. Hamer, and J. Oitmaa, Phys. Rev. B **57**, 392 (1998).

[79] Y. Matsushita, M. P. Gelfand, and C. Ishii, J. Phys. Soc. Jpn. **68**, 247 (1999).

[80] A. Collins and C. J. Hamer, Phys. Rev. B **78**, 054419 (2008).

[81] H. Liao and T. Li, J. Phys.: Condens. Matter **23**, 475602 (2011).

[82] K. Hida, J. Phys. Soc. Jpn. **67**, 1540 (1998).

[83] K. Hida, J. Phys. Soc. Jpn. **65**, 594 (1996).

[84] D. K. Yu, Q. Gu, H. T. Wang, and J. L. Shen, J. Phys.: Condens. Matter **11**, 3175 (1999).

[85] R. Ganesh, S.V. Isakov, and A. Paramekanti, Phys. Rev. B **84**, 214412 (2011).

[86] J. Oitmaa and R. R. P. Singh, Phys. Rev. B **85**, 014428 (2012).

[87] D.A. Huse and V. Elser, Phys. Rev. Lett. **60**, 2531 (1988).

[88] C. Gros, Ann. Phys. (N.Y.) **189**, 53 (1989).

[89] F. Mezzacapo, N. Schuch, M. Boninsegni, and J. I. Cirac, New J. Phys. **11**, 083026 (2009).

[90] Hao Zhang, M. Arlego, and C. A. Lamas, Phys. Rev. B **89**, 024403 (2014).

[91] D. P. Arovas and A. Auerbach, Phys. Rev. B **38**, 316 (1988); A. Auerbach and D. P. Arovas, Phys. Rev. Lett. **61**, 617 (1988).

[92] A. Auerbach, *Interacting Electrons and Quantum Magnetism* (Springer-Verlag, New York, 1994).

[93] A. Auerbach and D. P. Arovas, *Schwinger Bosons Approaches to Quantum Antiferromagnetism*, in Ref. [2].

[94] D. Yoshioka, J. Phys. Soc. Jpn. **58**, 32 (1989).

[95] D. Yoshioka, J. Phys. Soc. Jpn. **58**, 3733 (1989).

[96] J. E. Hirsch and S. Tang, Phys. Rev. B **39**, 2850 (1989)

[97] H. A. Ceccatto, C. J. Gazza, and A. E. Trumper, Phys. Rev. B **47**, 12329 (1993).

[98] C. J. Gazza and H. A. Ceccato, J. Phys.: Condens. Matter **5**, L135 (1993).

[99] A. E. Trumper, L. O. Manuel, C. J. Gazza, and H. A. Ceccatto, Phys. Rev. Lett. **78**, 2216 (1997).

[100] R. Flint and P. Coleman, Phys. Rev. B **79**, 014424 (2009).

[101] D. Yoshioka and J. Miyazaki, J. Phys. Soc. Jpn **60**, 614 (1991).

[102] L. Capriotti, A. E. Trumper, and S. Sorella, Phys. Rev. Lett. **82**, 3899 (1999).

[103] P. A. Lee, N. Nagaosa, and X. G. Wen, Rev. Mod. Phys. **78**, 17 (2006).

[104] L. B. Ioffe, M. V. Feigel'man, A. Ioselevich, D. Ivanov, M. Troyer, and G. Blatter, Nature **415**, 503 (2002).

[105] T. Nikuni, M. Oshikawa, A. Oosawa, and H. Tanaka, Phys. Rev. Lett. **84**, 5868 (2000).

[106] Hao Zhang, Carlos A. Lamas, Marcelo Arlego and Wolfram Brenig, Phys. Rev. B **93**, 235150 (2016).

[107] A. Mezio, C. N. Sposetti, L. O. Manuel, and A. E. Trumper, Europhys. Lett. **94**, 47001 (2011).

[108] H. Feldner, D. C. Cabra, and G. L. Rossini, Phys. Rev. B **84**, 214406 (2011).

[109] L. Messio, B. Bernu, and C. Lhuillier, Phys. Rev. Lett. **108**, 207204 (2012).

[110] G. Misguich, Phys. Rev. B **86**, 245132 (2012).

[111] L. Messio, C. Lhuillier, and G. Misguich, Phys. Rev. B **87**, 125127 (2013).

[112] The errors in the values of the phase boundaries only reflect the error in the extrapolation to the thermodynamic limit.

[113] J. Schwinger, *On Angular Momentum*, in *Quantum Theory of Angular Momentum*, edited by L. Biedenharn and H. Van Dam, (Academic, New York, 1965).

[114] J. H. P. Colpa, Physica A **93**, 327 (1978).

[115] P. Chandra, P. Coleman, and A. I. Larkin, Phys. Rev. Lett. **64**, 88 (1990).

[116] C. A. Lamas, D. C. Cabra, P. Pujol, and G. L. Rossini, arXiv:1406.4872 (2014).

[117] R. Moessner and S. L. Sondhi, Phys. Rev. Lett. **86**, 1881 (2001).

[118] J. D. Reger, J. A. Riera, and A. P. Young, J. Phys.: Condens. Matter **1**, 1855 (1989).

[119] U. Löw, Condens. Matter Phys. **12**, 497 (2009).

[120] X. G. Wen , Phys. Rev. B **65**, 165113 (2002).

[121] F. Wang and A. Vishwanath, Phys. Rev. B **74**, 174423 (2006).

[122] M. B. Hastings, Phys. Rev. B **69**, 104431 (2004).

[123] E. H. Lieb, T. D. Schultz, and D. Mattis, Ann. Phys. (NY) **16**, 407 (1961).

[124] I. Kimchi, S. A. Parameswaran, A. M. Turner, F. Wang, and A. Vishwanath, Proc. Nat. Acad. Sci. **110**, 16378 (2013).

[125] M. Raykin and A. Auerbach, Phys. Rev. Lett. **70**, 3808 (1993).

[126] L. O. Manuel, A. E. Trumper, and H. A. Ceccatto, Phys. Rev. B **57**, 8348 (1998).

[127] S. R. White, Phys. Rev. Lett. **69**, 2863 (1992).

[128] S. R. White and A. L. Chernyshev, Phys. Rev. Lett. **99**, 127004 (2007).

[129] E. M. Stoudenmire and S. R. White, Ann. Rev. Cond. Matter Phys. **3**, 111 (2012).

[130] S. M. Yan, D. A. Huse and S. R. White, Science **332**, 1173 (2011).

[131] S. Depenbrock, I. P. McCulloch, and U. Schollwöck, Phys. Rev. Lett. **109**, 067201 (2012).

[132] H. C. Jiang, H. Yao, and L. Balents, Phys. Rev. B **86**, 024424 (2012).

[133] M. Mambrini, A. Läuchli, and D. Poilblanc, Phys. Rev. B **74**, 144422 (2006).

[134] J. Reuther, P. Wölfle, R. Darradi, W. Brenig, M. Arlego, and J. Richter, Phys. Rev. B **83**, 064416 (2011).

[135] P. W. Leung and N. W. Lam, Phys. Rev. B **53**, 2213 (1996).

[136] T. Senthil, A. Vishwanath, L. Balents, S. Sachdev, and M. Fisher, Science **303**, 1490 (2004).

[137] C. Xu, Int. J. Mod. Phys. B **26**, 1230007 (2012).

[138] I. Bose and S. Gayen, Phys. Rev. B **48**, 10653(R) (1993).

[139] I. Bose, Phys. Rev. B **45**, 13072 (1992).

[140] A. Honecker, F. Mila, and M. Troyer, Eur. Phys. J. B **15**, 227 (2000).

[141] W. Brenig and K. W. Becker, Phys. Rev. B **64**, 214413 (2001).

[142] W. Brenig, A. Honecker, and K. W. Becker, in *Advances in Solid State Physics*, (ed) B Kramer (Springer, Berlin, Heidelberg, 2002), Vol. 42, p. 457.

[143] M. Arlego and W. Brenig, Eur. Phys. J. B **53**, 193 (2006).

[144] P. Chen, C. Y. Lai, and M. F. Yang, Phys. Rev. B **81**, 020409(R) (2010).

[145] O. Derzhko, T. Krokhmalskii, and J. Richter, Phys. Rev. B **82**, 214412 (2010).

[146] C. A. Lamas and J. M. Matera, Phys. Rev. B **92**, 115111 (2015).

[147] P. W. Anderson, Phys. Rev. **83**, 1260 (1951).

[148] S. Sachdev and R. N. Bhatt, Phys. Rev. B **41**, 9323 (1990).

[149] A. V. Chubukov, JETP Lett. **49**, 129 (1989).

[150] A. V. Chubukov and T. Jolicoeur, Phys. Rev. B **44**, 12050(R) (1991).

[151] F. Wegner, Ann. Phys. **506**, 77 (1994).

[152] C. Knetter and G. S. Uhrig, Eur. Phys. J. B **13**, 209 (2000).

[153] W. Brenig and A. Honecker, Phys. Rev. B **65**, 140407(R) (2002).

[154] M. Grzeschik and W. Brenig, Phys. Rev. B **69**, 064420 (2004).

[155] M. Arlego and W. Brenig, Phys. Rev. B **75**, 024409 (2007).

[156] M. Arlego and W. Brenig, Phys. Rev. B **78**, 224415 (2008).

[157] W. Brenig, Phys. Rev. B **67**, 064402 (2003).

[158] M. Arlego and W. Brenig, Phys. Rev. B **84**, 134426 (2011).

[159] M. Arlego, C. A. Lamas, and Hao Zhang, J. Phys.: Conf. Series **568**, 042019 (2014).

[160] I. E. Dzyaloshinskii, Zh. Eksp. Teor. Fiz. **32**, 1547 (1957) [Sov. Phys. JETP **5**, 1259 (1957)].

[161] I. Dzyaloshinsky, J. Phys. Chem. Solids. **4**, 241 (1958).

[162] T. Moriya, Phys. Rev. Lett. **4**, 228 (1960).

[163] T. Moriya, Phys. Rev. **120**, 91 (1960).